



Approaching complexity by stochastic methods: From biological systems to turbulence

Rudolf Friedrich^a, Joachim Peinke^b, Muhammad Sahimi^c, M. Reza Rahimi Tabar^{d,b,e,*}

^a Institute for Theoretical Physics, University of Münster, D-48149 Münster, Germany

^b Institute of Physics, Carl von Ossietzky University, D-26111 Oldenburg, Germany

^c Mork Family Department of Chemical Engineering and Materials Science, University of Southern California, Los Angeles, CA 90089-1211, USA

^d Department of Physics, Sharif University of Technology, Tehran 11155-9161, Iran

^e Fachbereich Physik, Universität Osnabrück, Barbarastrafße 7, 49076 Osnabrück, Germany

ARTICLE INFO

Article history:

Accepted 30 March 2011

Available online 13 June 2011

editor: H. Orland

Keywords:

Stochastic processes

Time series

Multifractal

Fokker–Planck and Langevin equations

ABSTRACT

This review addresses a central question in the field of complex systems: given a fluctuating (in time or space), sequentially measured set of experimental data, how should one analyze the data, assess their underlying trends, and discover the characteristics of the fluctuations that generate the experimental traces? In recent years, significant progress has been made in addressing this question for a class of stochastic processes that can be modeled by Langevin equations, including additive as well as multiplicative fluctuations or noise. Important results have emerged from the analysis of temporal data for such diverse fields as neuroscience, cardiology, finance, economy, surface science, turbulence, seismic time series and epileptic brain dynamics, to name but a few. Furthermore, it has been recognized that a similar approach can be applied to the data that depend on a length scale, such as velocity increments in fully developed turbulent flow, or height increments that characterize rough surfaces. A basic ingredient of the approach to the analysis of fluctuating data is the presence of a Markovian property, which can be detected in real systems above a certain time or length scale. This scale is referred to as the *Markov–Einstein* (ME) scale, and has turned out to be a useful characteristic of complex systems. We provide a review of the operational methods that have been developed for analyzing stochastic data in time and scale. We address in detail the following issues: (i) reconstruction of stochastic evolution equations from data in terms of the Langevin equations or the corresponding Fokker–Planck equations and (ii) intermittency, cascades, and multiscale correlation functions.

© 2011 Elsevier B.V. All rights reserved.

Contents

1. Introduction.....	88
2. Stochastic processes.....	90
2.1. Discrete time evolution.....	91
2.1.1. Discrete time approximation of stochastic evolution equations.....	92
2.1.2. Limit theorems, and Wiener and Lévy processes.....	92
2.2. Statistical description of stochastic processes.....	93
2.2.1. Probability distributions.....	93
2.2.2. Markov processes.....	94

* Corresponding author at: Institute of Physics, Carl von Ossietzky University, D-26111 Oldenburg, Germany. Tel.: +49 5419697062.

E-mail address: mohammed.r.rahimi.tabar@uni-oldenburg.de (M. Reza Rahimi Tabar).

2.2.3.	Short-time propagator of Langevin processes	94
2.2.4.	Short-time propagator of the Lévy processes	95
2.2.5.	Joint probability distribution and Markovian properties	95
2.3.	Finite-time propagators	95
2.3.1.	The Fokker–Planck equation	95
2.3.2.	Fractional Fokker–Planck equations	96
2.4.	Measurement noise	96
3.	Stochastic data analysis as a function of time	96
3.1.	Markovian properties and Markov–Einstein time (length) scale	97
3.2.	Estimation of drift and diffusion coefficients	98
3.2.1.	Estimation of the drift vector	98
3.2.2.	Estimation of the diffusion matrix	99
3.2.3.	Higher-order cumulants	99
3.2.4.	Lévy processes	99
3.2.5.	Differentiating between stochastic process and noise data	99
3.2.6.	Estimation of the drift and diffusion coefficients from sparsely sampled time series	99
3.2.7.	Multiscale construction of time series	100
3.2.8.	Mapping stochastic processes onto complex networks	100
3.3.	Level-crossing analysis of time series	100
3.3.1.	Numerical aspects and precision	102
3.3.2.	Self-consistency	102
4.	Stochastic data analysis in length scale	102
4.1.	The Langevin dynamics in scale	103
4.2.	Deformation of the PDF on scale and cascade of information, from large to small scales	103
4.2.1.	Multiscale correlation functions	103
4.2.2.	Multipliers	105
5.	Applications: processes in time and space	106
5.1.	Epileptic brain dynamics and stochastic qualifiers	107
5.2.	Heart interbeat fluctuations	110
5.2.1.	Markov analysis of nonstationary heart interbeat data	111
5.2.2.	Comparison with other methods	113
5.3.	Econophysics: financial data	114
5.3.1.	Analysis of the fluctuations in the daily price of oil	114
5.3.2.	Fluctuations in the currency exchange rates	117
5.4.	Rough surfaces	118
5.4.1.	Reconstruction of rough surfaces	118
5.4.2.	Controlling surface statistical properties using bias voltage	120
6.	Applications: processes in scales	125
6.1.	Turbulence	126
6.1.1.	Two-point statistics	127
6.1.2.	Multipoint statistics: the Fokker–Planck analysis	131
6.1.3.	Markov properties	131
6.1.4.	Kramers–Moyal coefficients	133
6.1.5.	Integration of the Fokker–Planck equation	134
6.1.6.	Joint multipoint statistics of longitudinal and transverse increments	136
6.2.	Passive scalar	137
6.3.	Econophysics: financial data in scale and the measurement noise	142
6.3.1.	Markov properties	145
6.3.2.	Kramers–Moyal coefficients	145
6.3.3.	Consistency checks	148
6.4.	Seismic time series	149
7.	Conclusions and outlook	156
	Acknowledgments	157
	References	157

1. Introduction

Overview

Quite often the behavior of complex systems that are far from equilibrium can be traced back to rather simple laws, due to the existence of self-organizing processes [1–6]. Complex systems are composed of a huge number of microscopic subsystems, which irregularly vary on a fast time scale. The fast dynamics can often be treated as fluctuations. Self-organized behavior arises due to the emergence of collective variables, or order parameters, which, compared to the time or length scales of the microscopic subsystems, vary on slower temporal and larger spatial scales. The interaction of the order parameters are typically nonlinear, with the microscopic degrees of freedom showing up in irregular fluctuations that

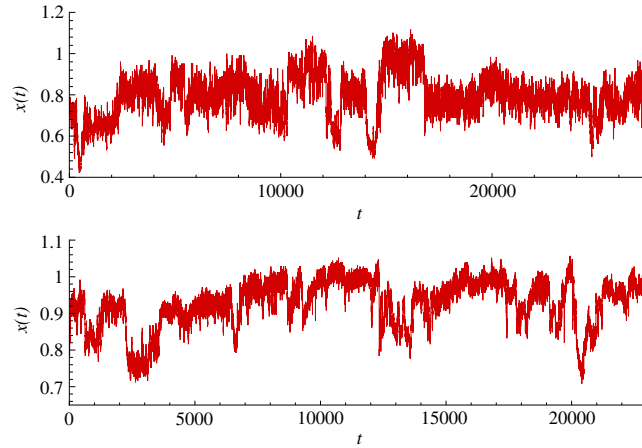


Fig. 1. Time series of interbeat intervals $x(t)$ versus interval number t for a typical person with congestive heart failure (bottom) and a healthy subject (top).

participate in the order parameter dynamics. As a result, the analysis of the behavior of complex systems must be based on the assessment of the nonlinear interactions, as well as the determination of the characteristics and the strength of the fluctuating forces. This immediately leads to the problem of retrieving a stochastic dynamical system from data; see Fig. 1 for typical stochastic time series.

Analysis of time series has a long tradition in the field of nonlinear dynamics [7–9]. Much effort has been devoted to addressing the question of how to extract a deterministic dynamical system from a suitable analysis of experimental data, since the correct analysis may yield all the important information on the dynamical properties of the system under consideration. Usually, the fluctuations are treated as a random variable, additively superimposed on a trajectory generated by a deterministic dynamical system. The problem of dynamical noise, i.e., fluctuations that interfere with the dynamical evolution, has not been addressed in much details, although it is of utmost importance for the analysis of strongly fluctuating time series.

This review provides detailed description and discussion of the methods that have been developed for analyzing stochastic data in time and/or length scales. The development of such methods has been stimulated by research on turbulent flows [10–13], which has shown the necessity of treating the fluctuations as dynamical variables which interfere with the deterministic dynamics. We address in detail the following issues: (i) How to reconstruct stochastic evolution equations from data in terms of the Langevin equation, or the corresponding Fokker–Planck equation and (ii) intermittency, cascades, and multiscale correlation functions in the data.

A necessary ingredient of the system under consideration is that, its dynamical behavior should be described by a set of macroscopic order parameters $\mathbf{X}(t)$ that are governed by the nonlinear Langevin equations [14–17],

$$\frac{d}{dt}\mathbf{X} = D^{(1)}(\mathbf{X}) + g(\mathbf{X})\mathbf{F}(t) \quad (1.1)$$

where $\mathbf{X}(t)$ denotes the n -dimensional state vector, $D^{(1)}(\mathbf{X})$ the drift vector, and the matrix $g(\mathbf{X})$ is related to the diffusion matrix according to, $D^{(2)}(\mathbf{X})_{ij} = \sum_k g_{ik}(\mathbf{X})g_{jk}(\mathbf{X})$. The noise terms $F_i(t)$ lumped together in the vector $\mathbf{F}(t)$ are fluctuating forces with Gaussian statistics and rapidly decaying temporal correlations, such that delta-correlation in time can be assumed, i.e., $\langle F_i(t) \rangle = 0$, and, $\langle F_i(t)F_j(t') \rangle = 2\delta_{ij}\delta(t - t')$.

Applications of the method include for example, the analysis of noisy electrical circuits [18], stochastic dynamics of metal cutting [19,20], systems with feedback delay [21,22], meteorological processes such as analyzing of sea surface wind vectors [23,24], traffic flow data [25] and physiological time series [26].

It has turned out that the method of analysis based on the Markov processes can also be successfully applied to not only fluctuating time series, but also the analysis of spatially disordered structures, such as fluid turbulence [10,27–29] or characterization of rough surfaces [30,32,34–37]. Such structures can be analyzed as scale-dependent stochastic processes. Experimental observables include the velocity increments, i.e., the difference in the velocity field between two points separated by a distance r , or the analogously defined height increments for rough surfaces. The change of the increments as a function of the distance r can then be viewed as a stochastic process over a length scale and can, quite often, be mapped onto the mathematical structures of the Langevin processes.

Further length/time scale-dependent processes that may be analyzed by such methods include passive scalar advection [38], financial time series [39–42], human interbeat fluctuations [43–47], cosmic microwave background radiation [48], epileptic brain dynamics [50] and seismic time series [52–54], etc.

At the same time, the method can be viewed as an extension of the multifractal description of stochastic processes [55]. The multifractal description focusses on the scaling behavior of the moments of quantities of interest, such as velocity or

temperature increments, as a function of the scale. The complete information on an increment, $\Delta_r X(t) = X(t+r) - X(t)$, is contained in the probability distribution function (PDF), $\tilde{p}(\Delta_r X, r)$, for a certain scale r . It is assumed that the increments exhibit scaling behavior, $\Delta_r X \approx r^h$, with locally varying scaling [56]. As a consequence, the PDF is constructed as a superposition of the probability distributions

$$p(\Delta_r X, r) = \int dh \frac{1}{r^h} \tilde{p}(\Delta_r X/r^h) f(h, r), \quad (1.2)$$

where the measure $f(h, r)$ characterizes the distribution of the regions with different scaling behavior.

In contrast, the approach based on the characterization of the field by a scale-dependent stochastic process aims at describing the joint statistics of the chosen measure on many different scales. This is achieved by the knowledge of the joint PDF, $p(\Delta X(t, r_1); \dots; \Delta X(t, r_n))$. Using such joint PDFs, the correlations between the scales are also worked out, demonstrating how the complexity is linked between scales. If the statistics of the scale-dependent measure can be regarded as a Markov process evolving in r , the knowledge of two-scale conditional PDF is sufficient for a complete description of multiscale joint PDF. As recently shown this can be extended to the n -point statistics $p(X(t_1) \dots X(t_n))$ [101,102].

The Markov method has the advantage that it relates the random variables across different scales by introducing a conditional PDF or, in fact, a two-scale PDF. Provided that the Markov property holds, which can be tested experimentally, a complete statistical characterization of the process across the scales is obtained.

The method is also capable of yielding the scaling behavior of the multiscale correlation functions [57–63], i.e.,

$$\begin{aligned} \mathcal{F}_{p+q}(r, R) &\equiv \langle [X(t+r) - X(t)]^p [X(t+R) - X(t)]^q \rangle \\ &\equiv \langle [\Delta_r X(t)]^p [\Delta_R X(t)]^q \rangle \end{aligned} \quad (1.3)$$

which has been shown that, for a large class of processes independent of their details, behaves as

$$\mathcal{F}_{p+q}(r, R) \sim S_p(r) S_{p+q}(R) / S_p(R) \quad (1.4)$$

where, $S_m(r) = \langle [X(t+r) - X(t)]^m \rangle$. All the results have led to the conclusion that, for the processes that satisfy Eq. (1.4), multiscale correlation functions that are measured for time series are fully consistent with a multiplicative random process for the evolution of the increments in length scale.

As another consequence, the Markov method allows us to analyze and obtain the complete information about level crossing of time series [64–67,41]. In the level-crossing analysis one is interested in determining the average frequency (in time or space) ν_α^+ of observing a given value for a fluctuating function, $X - \bar{X} = \alpha$, in time series from which one determines the average number of crossing the given level in a sample of size T . The average number of visiting the magnitude $X - \bar{X} = \alpha$ with positive slope is, $N_\alpha^+ = \nu_\alpha^+ T$. It can be shown that for discrete time series ν_α^+ can be written in terms of the drift and diffusion coefficients of the underlying stochastic process [41]. For continuous time series the frequency ν_α^+ is determined by averaging the time derivative of the series on the level α over positive slopes [64,65].

The third consequence of the Markov method is that it enables us to understand the cascade nature of scale-dependent processes, as well as the intermittency of the time series. The structures that arise in a time series exhibit themselves as high peaks at random times. The intervals between them are characterized by a low intensity and a large size. Rare peaks are the hallmarks of the PDF's non-Gaussian tails.

The plan of the review is as follows. In Section 2 we give a brief review of essentials of stochastic processes. The main subjects discussed include discrete time evolution, statistical description of stochastic time series, and finite-time propagators. The section ends with the definition of measurement noise. In Section 3 we discuss stochastic analysis and introduce the Markov–Einstein time (length) scale of a data set, which is the basic characteristic time (length) scale of the Markov method. This section contains some technical aspects of the method for estimating the drift and diffusion coefficients of a stochastic series. In addition, explicit expressions for the level-crossing analysis, in terms of the drift and diffusion coefficients, are given. In Section 4 we take up the issue of stochastic analysis for data that depend on length scales, and provide a physical picture of the information cascade from large to small scales. Moreover, this section introduces the multiscale correlation functions and multiplier. Examples of the applications of the method to the analysis of time series are given in Section 5. We address such phenomena as epileptic brain dynamics, heart interbeat fluctuations and financial data. Examples of analysis of the data that fluctuate over length scales are given in Section 6, which include hydrodynamics turbulence, passive scalar, rough surfaces, financial increments and seismic time series.

2. Stochastic processes

In what follows we consider a class of systems that are described by a multivariate state vector $\mathbf{X}(t)$ contained in a d -dimensional state space $\{\mathbf{x}\}$. The evolution of the state vector $\mathbf{X}(t)$ is assumed to be governed by a deterministic part to which noise is added:

$$\frac{d}{dt} \mathbf{X}(t) = \mathbf{N}(\mathbf{X}(t), t) + \mathbf{F}(\mathbf{X}(t), t). \quad (2.1)$$

Here \mathbf{N} denotes a nonlinear function that depends on the stochastic variable $\mathbf{X}(t)$ and, additionally, may explicitly depend on time t . Note, however, that the time t may also be considered as a general variable and replaced by, for example, a scale variable l , as described by, for example, [3,4]. Because the function \mathbf{N} can be nonlinear, that systems that exhibit chaotic time evolution in the deterministic case are also included in the class of stochastic processes (2.1). The term $\mathbf{F}(\mathbf{X}(t), t)$ fluctuates on a fast time scale. We assume that the d components F_i can be represented in the form

$$F_i(\mathbf{X}(t), t) = \sum_{j=1}^d g_{ij}(\mathbf{X}(t), t) F_j(t). \quad (2.2)$$

The quantities $F_j(t)$ are considered to be random functions, whose statistical characteristics are well defined. It is evident that these properties determine significantly the dynamical behavior of the state vector $\mathbf{X}(t)$. Formally, this approach also includes purely deterministic processes by taking, $F = 0$.

2.1. Discrete time evolution

It is convenient to consider the temporal evolution (2.1) of the state vector $\mathbf{X}(t)$ on a time scale that is large compared to the time scale of the fluctuations $F_j(t)$. As we shall briefly indicate below, a stochastic process related to the evolution Eq. (2.1) can be modeled by stochastic evolution laws that relate the state vectors $\mathbf{X}(t)$ at times t_i , $t_{i+1} = t_i + \tau$, $t_{i+2} = t_i + 2\tau, \dots$, for small but finite values of τ . Here, we deal with the class of proper Langevin processes that are defined by the following discrete time evolutions.

(a) *Proper Langevin equations: White noise*

The discrete time evolution of a proper Langevin process is given by

$$\mathbf{X}(t_{i+1}) = \mathbf{X}(t_i) + \mathbf{D}^{(1)}[\mathbf{X}(t_i), t_i]\tau + \mathbf{g}(\mathbf{X}(t_i), t_i)\sqrt{\tau}\boldsymbol{\Gamma}(t_i) \quad (2.3)$$

where $\mathbf{D}^{(1)}[\mathbf{X}(t_i), t_i]$ and $\boldsymbol{\Gamma}(t_i)$ are the drift vector and a fluctuating quantity characterized by a Gaussian distribution with zero mean, $\langle \boldsymbol{\Gamma}(t_i) \rangle = \mathbf{0}$,

$$p(\boldsymbol{\Gamma}) = \frac{1}{(\sqrt{2\pi})^d} e^{-\frac{\boldsymbol{\Gamma}^2}{2}} = \frac{1}{(\sqrt{2\pi})^d} \exp\left(-\sum_{\alpha=1}^d \frac{1}{2} \Gamma_{\alpha}^2\right). \quad (2.4)$$

Furthermore, they are statistically independent for different times

$$\langle \Gamma_{\alpha}(t_i) \Gamma_{\beta}(t_j) \rangle = \delta_{\alpha\beta} \delta_{ij}. \quad (2.5)$$

The discrete Langevin Eq. (2.3) must be considered in the limit $\tau \rightarrow 0$. In the following we describe how the discrete time processes are related to the stochastic evolution equation, Eq. (2.1).

(b) *Generalized Langevin equations: Lévy noise*

A more general class is formed by the discrete time evolution laws [68,69],

$$\mathbf{X}(t_{i+1}) = \mathbf{X}(t_i) + \mathbf{D}^{(1)}[\mathbf{X}(t_i), t_i]\tau + \mathbf{g}(\mathbf{X}(t_i), t_i)\tau^{1/\alpha}\boldsymbol{\eta}_{\alpha,\beta}(t_i) \quad (2.6)$$

where $\mathbf{D}^{(1)}[\mathbf{X}(t_i), t_i]$ and $\boldsymbol{\eta}_{\alpha,\beta}(t_i)$ are the drift vector and a fluctuating quantity, distributed according to the Lévy stable law, characterized by the Lévy parameters α and β [70]. The physical origin of the scaling factor $\tau^{1/\alpha}$ is as follows. A variable X corresponding to such a process can frequently exhibit the dynamics described by the notion of superdiffusion, where the characteristic value $\langle X(t)^2 \rangle$ of the variable X demonstrates scaling behavior $\langle X(t)^2 \rangle \sim t^{2/\alpha}$, with $\alpha < 2$. Some examples are the motion of tracer particles in turbulent flows [71], the diffusion of particles in random media [72], human travel behavior and spreading of epidemics [73] or economic time series in finance [74]. Therefore the variable X scales with time as $\tau^{1/\alpha}$.

As is well known, only the Fourier transform of the distribution is well defined,

$$\begin{aligned} p_{\alpha,\beta}(\eta) &= \frac{1}{2\pi} \int dk Z(k, \alpha, \beta) e^{-ik\eta} \\ Z(k, \alpha, \beta) &= e^{-i|k|^{\alpha}(1-i\beta\text{sign}(k)\Phi)} \\ \Phi &= \tan\left(\frac{\pi\alpha}{2}\right) \quad \alpha \neq 1, \quad \Phi = -\frac{2}{\pi} \ln|k| \quad \alpha = 1. \end{aligned} \quad (2.7)$$

The Gaussian distribution represents a special limit of the class of Lévy stable distributions, $\alpha = 2$ and $\beta = 0$. Formally, one has, $0 < \alpha \leq 2$. However, for almost all applications it seems reasonable to choose, $1 < \alpha \leq 2$, in order for the first moment of the noise source to exist. The parameter β characterizes the skewness of the distribution, i.e. the deviation from a symmetric of the pdf. For a detailed definition we refer the reader to the monograph by Feller [75]. The consideration of this type of statistics for the noise variables η is based on the central-limit theorem, as discussed below.

The discrete Langevin equation, Eq. (2.3), and the generalized Langevin equation, Eq. (2.6), must be considered in the limit, $\tau \rightarrow 0$. They are the basis of all the further treatments. A central point is that, if one assumes the noise sources to be independent of the variable $\mathbf{X}(t_i)$, the discrete time evolution equations define a Markov process, the generator of which, i.e., its conditional probability distribution or short-time propagator, is established on the basis of Eqs. (2.3) and (2.6).

We now describe how the discrete time processes are related to the stochastic evolution described by Eq. (2.1).

2.1.1. Discrete time approximation of stochastic evolution equations

In order to motivate the discrete time approximations, Eq. (2.3), we integrate the evolution law [14] over a finite but small time increment τ :

$$\begin{aligned} \mathbf{X}(t + \tau) &= \mathbf{X}(t) + \int_t^{t+\tau} dt' \mathbf{N}(\mathbf{X}(t'), t') + \int_t^{t+\tau} dt' g(\mathbf{X}(t'), t') \Gamma(t') \\ &\approx \mathbf{X}(t) + \tau \mathbf{N}(\mathbf{X}(t), t) + \int_t^{t+\tau} dt' g(\mathbf{X}(t'), t') \Gamma(t'). \end{aligned} \quad (2.8)$$

The time interval τ is chosen to be larger than the time scale of the fluctuations of $\Gamma_j(t)$. It involves the rapidly fluctuating quantities $\Gamma_j(t)$, and is represented by a stochastic integral [15–17,14].

If we assume the matrix g to be independent of the time t and the state vector $\mathbf{X}(t)$, we arrive at the integrals

$$d\mathbf{W}(t, \tau) = \int_t^{t+\tau} dt' \Gamma(t'). \quad (2.9)$$

These are the quantities for which a statistical characterization can be given. We shall pursue this problem in the next subsection. However, looking at Eq. (2.8), we encounter the difficulty that the integrals over the noise forces may involve functions of the state vector within the time interval $(t, t + \tau)$. The interpretation of such integrals for wildly fluctuating stochastic quantities $\Gamma(t)$ is difficult. The simplest way is to formulate an interpretation of such terms that leads to different interpretations of the stochastic evolution equation, Eq. (2.1). We formulate the widely used definitions due to Itô and Stratonovich.

In the Itô sense, the integral is interpreted as

$$\int_t^{t+\tau} dt' g(\mathbf{X}(t'), t') \Gamma(t') = g(\mathbf{X}(t), t) \int_t^{t+\tau} dt' \Gamma(t') = g(\mathbf{X}(t), t) d\mathbf{W}(t, \tau). \quad (2.10)$$

The Stratonovich definition is

$$\begin{aligned} \int_t^{t+\tau} dt' g(\mathbf{X}(t'), t') \Gamma(t') &= g\left(\frac{\mathbf{X}(t + \tau) + \mathbf{X}(t)}{2}, t + \frac{\tau}{2}\right) \int_t^{t+\tau} dt' \Gamma(t') \\ &= g\left(\frac{\mathbf{X}(t + \tau) + \mathbf{X}(t)}{2}, t + \frac{\tau}{2}\right) d\mathbf{W}(t, \tau). \end{aligned} \quad (2.11)$$

Since from experiments one obtains the probability distributions of the stochastic processes that are related to the stochastic Langevin equations, we are free to choose a certain interpretation of the process. In the following we shall always adopt the Itô interpretation. In this case, the drift vector $\mathbf{D}^1(\mathbf{x}, t) = \mathbf{N}(\mathbf{x}, t)$ coincides with the nonlinear vector field $\mathbf{N}(\mathbf{x}, t)$. We note that Itô and Stratonovich interpretations arise due to the fact that Langevin equations with multiplicative noise need an interpretation of the evaluation of stochastic integrals, as outlined above. In this sense the Itô and Stratonovich calculations are equivalent, since they yield two different interpretations of the Langevin equations leading to the same probability distributions. It may look arbitrary to choose one of them, but fortunately we know how to translate between them. Operationally, the Stratonovich stochastic differential equations (SDE) are easier to solve analytically, but Itô SDEs are more natural starting points for numerical schemes. White noise is an idealization of a real fluctuating forcing which has finite amplitude and timescale. If white noise is an approximation to continuously fluctuating noise with finite memory (much shorter than the dynamical timescales of the considered process), the appropriate representation is the Stratonovich one (Wong–Zakai Theorem [277]). If white noise approximates a sequence of discrete pulses with finite time separation, then the Itô representation is appropriate.

2.1.2. Limit theorems, and Wiener and Lévy processes

In the following we shall discuss the possibilities of characterizing the stochastic integrals

$$W(t + \tau) - W(t) = \int_t^{t+\tau} dt' \Gamma(t') \quad (2.12)$$

where $\Gamma(t)$ is a rapidly fluctuating quantity of zero mean. In order to characterize the properties of this force, one can resort to the limit theorems of statistical mechanics [70]. The central-limit theorem states that if the quantities $\Gamma_j, j = 1, \dots, n$ are statistically independent variables of zero mean and variance σ^2 , then the sum

$$\frac{1}{\sqrt{n}} \sum_{j=1}^n \Gamma_j = \Gamma \quad (2.13)$$

tends to a Gaussian random variable with variance σ^2 for large values of n . The limiting probability distribution $h(\Gamma)$ is then a Gaussian distribution with variance σ^2 :

$$p(\Gamma) = \frac{1}{\sqrt{2\pi\sigma^2}} \exp(-\Gamma^2/2\sigma^2). \tag{2.14}$$

As is well known, there exists a generalization of the central-limit theorem, which applies to random variables whose second moments do not exist. It states that the distribution of the sum over identically distributed random variables Γ_j

$$\frac{1}{n^{1/\alpha}} \sum_{j=1}^n \Gamma_j = \eta_{\alpha,\beta} \tag{2.15}$$

tends to a random variable $\eta_{\alpha,\beta}$ that is distributed according to the Lévy stable distribution $p_{\alpha,\beta}(\eta)$ [278]. The Lévy stable distributions can only be given by their Fourier transforms, Eq. (2.7).

In order to evaluate the integral (2.12) using the limit theorems, it is convenient to represent the stochastic force $\Gamma(t)$ as a sum over $N_\tau \delta$ -kicks occurring at discrete times t_j

$$\Gamma(t) = \sum_j \Gamma_j(\Delta t)^{1/\alpha} \delta(t - t_j), \tag{2.16}$$

where Δt is the time difference between the occurrence of the two kicks. Then, we obtain

$$\begin{aligned} dW(t, \tau) &= \sum_{j,t_j \in \tau} \Gamma_j(\Delta t)^{1/\alpha} \\ &= (N_\tau \Delta t)^{1/\alpha} \frac{1}{N_\tau^{1/\alpha}} \sum_{j,t_j \in \tau} \Gamma_j = \tau^{1/\alpha} \eta(t). \end{aligned} \tag{2.17}$$

An application of the central-limit theorem shows that, if the quantities Γ_j are independent, identically distributed variables, the integral

$$\frac{1}{\tau^{1/\alpha}} \int_t^{t+\tau} \Gamma \tag{2.18}$$

can be considered to be a random variable $\eta(t)$ which, in the limit $N_\tau \rightarrow \infty$, tends to a stable random variable. Thus, for the case of $\alpha = 2$, i.e., for the case in which the second moments of the random kicks exist, the stochastic variable $dW(t, \tau)$ may be represented by the increments

$$dW(t, \tau) = \sqrt{\tau} \eta(t) \tag{2.19}$$

where $\eta(t)$ is a random variable, distributed according to a Gaussian distribution. For the more general case, $dW(t, \tau)$ is a stochastic variable

$$dW(t, \tau) = \tau^{1/\alpha} \eta_{\alpha,\beta}(t) \tag{2.20}$$

where the distribution of $\eta_{\alpha,\beta}$ is the Lévy distribution, i.e., Eq. (2.7).

2.2. Statistical description of stochastic processes

In the previous subsection we discussed processes described by stochastic equations. In the present subsection we shall summarize the corresponding statistical description. Such a description is achieved by introducing suitable statistical averages. We shall denote the averages by the brackets $\langle \cdot \rangle$. For stationary processes the averages can be viewed as a time average. For nonstationary processes the averages are defined as ensemble averages, i.e., averages over an ensemble of experimental (or numerical) realizations of the stochastic process (2.1). For stationary processes in time, one usually deals with time averages.

2.2.1. Probability distributions

The set of stochastic evolution equations, Eq. (2.1), or its finite time representations, Eq. (2.3), define a Markov process. We consider the joint probability density

$$p(\mathbf{x}_n, t_n; \dots; \mathbf{x}_1, t_1; \mathbf{x}_0, t_0) \tag{2.21}$$

which is related to the joint probability, to find the system at times t_i in the volume ΔV_i in the phase space. If we take the times t_i that are separated by the small time increment $\tau = t_{i+1} - t_i$, then the probability density can be related to the discrete time representation of the stochastic process (2.3), according to

$$p(\mathbf{x}_n, t_n; \dots; \mathbf{x}_1, t_1; \mathbf{x}_0, t_0) = \langle \delta(\mathbf{x}_n - \mathbf{X}(t_n)) \cdots \delta(\mathbf{x}_0 - \mathbf{X}(t_0)) \rangle \tag{2.22}$$

where the brackets indicate the statistical average, which may be a time average (for stationary processes) or an ensemble average.

2.2.2. Markov processes

An important subclass of stochastic processes are Markov processes. For such processes the joint probability distribution $p(\mathbf{X}_n, t_n; \dots; \mathbf{X}_1, t_1; \mathbf{X}_0, t_0)$ can be constructed from the knowledge of the conditional probability distributions

$$p(\mathbf{x}_{i+1}, t_{i+1} | \mathbf{x}_i, t_i) = \frac{p(\mathbf{X}_{i+1}, t_{i+1}; \mathbf{x}_i, t_i)}{p(\mathbf{x}_i, t_i)} \quad (2.23)$$

according to

$$p(\mathbf{x}_n, t_n; \dots; \mathbf{x}_1, t_1; \mathbf{x}_0, t_0) = p(\mathbf{x}_n, t_n | \mathbf{x}_{n-1}, t_{n-1}) \cdots p(\mathbf{x}_1, t_1 | \mathbf{x}_0, t_0) p(\mathbf{x}_0, t_0). \quad (2.24)$$

Here, the Markov property of a process for the multiply conditioned probabilities

$$p(\mathbf{x}_i, t_i | \mathbf{x}_{i-1}, t_{i-1}; \dots; \mathbf{x}_0, t_0) = p(\mathbf{x}_i, t_i | \mathbf{x}_{i-1}, t_{i-1}) \quad (2.25)$$

is used. As a consequence, the knowledge of the transition probabilities, together with the initial probability distribution $p(\mathbf{x}_0, t_0)$, suffice to define the N -point probability distribution.

It is straightforward to prove the Chapman–Kolmogorov equation using the 3-point probability distribution for Markov processes:

$$p(\mathbf{x}_j, t_j | \mathbf{x}_i, t_i) = \int d\mathbf{x}_k p(\mathbf{x}_j, t_j | \mathbf{x}_k, t_k) p(\mathbf{x}_k, t_k | \mathbf{x}_i, t_i). \quad (2.26)$$

This relation is valid for all times $t_i < t_k < t_j$. In the following we shall show that the transition probabilities $p(\mathbf{x}_{j+1}, t + \tau | \mathbf{x}_j, t)$ can be determined for small time differences τ . This defines the so-called short-time propagators.

2.2.3. Short-time propagator of Langevin processes

It is straightforward to determine the short-time propagator from the finite time approximation, Eq. (2.3), of the Langevin equation. We shall denote the propagators by $p(\mathbf{x}_{j+1}, t + \tau | \mathbf{x}_j, t)$, in contrast to the finite-time propagators, Eq. (2.23), for which the time interval $t_{i+1} - t_i$ is large compared to τ . We consider the case of Gaussian noise. The variables $\Gamma(t_i)$ are Gaussian random vectors with probability distribution

$$p[\Gamma] = \frac{1}{\sqrt{(2\pi)^d}} \exp\left(-\frac{1}{2} \Gamma \cdot \Gamma\right). \quad (2.27)$$

The finite-time interpretation of the Langevin equation is then rewritten in the form

$$\Gamma(t_i) = \frac{1}{\tau^{1/2}} [g(\mathbf{X}(t_i), t_i)]^{-1} [\mathbf{X}(t_{i+1}) - \mathbf{X}(t_i) - \tau \mathbf{D}^{(1)}(\mathbf{X}(t_i))]. \quad (2.28)$$

In turn, this relation defines the transition probability distribution

$$p(\mathbf{x}_{i+1}, t_{i+1} | \mathbf{x}_i, t_i) d\mathbf{x}_{i+1} = p[\Gamma(t_i) = \Gamma] J(\mathbf{x}_i, t_i) d\mathbf{x}_{i+1}, \quad (2.29)$$

where J is the determinant of the Jacobian

$$J_{\alpha\beta} = \frac{\partial \Gamma_\alpha(t_i)}{\partial \mathbf{x}_{i+1, \beta}}, \quad (2.30)$$

and $[g]^{-1}$ denotes the inverse of the matrix g (which is assumed to exist). In what follows it is convenient to define the so-called diffusion matrix $D^{(2)}(\mathbf{x}_i, t_i)$

$$D^{(2)}(\mathbf{x}_i, t_i) = g^T(\mathbf{x}_i, t_i) g(\mathbf{x}_i, t_i). \quad (2.31)$$

We are now able to explicitly state the short-time propagator of the process (2.3):

$$p(\mathbf{x}_i + \tau, t_{i+1} | \mathbf{x}_i, t_i) = \frac{1}{\sqrt{(2\pi\tau)^d \text{Det}[D^{(2)}]}} \exp[-S(\mathbf{x}_{i+1}, \mathbf{x}_i, t_i, \tau)] \quad (2.32)$$

where we have defined the quantity $S(\mathbf{x}_{i+1}, \mathbf{x}_i, t_i, \tau)$ according to

$$S(\mathbf{x}_{i+1}, \mathbf{x}_i, t_i, \tau) = \frac{1}{2} \tau \left[\frac{\mathbf{x}_{i+1} - \mathbf{x}_i}{\tau} - \mathbf{D}^{(1)}(\mathbf{x}_i, t_i) \right] [D^{(2)}(\mathbf{x}_i, t_i)]^{-1} \left[\frac{\mathbf{x}_{i+1} - \mathbf{x}_i}{\tau} - \mathbf{D}^{(1)}(\mathbf{x}_i, t_i) \right]. \quad (2.33)$$

As we see, the short-time propagator, which yields the transition probability density from state \mathbf{x}_i to state \mathbf{x}_{i+1} in the finite but small time interval τ is a normal distribution.

2.2.4. Short-time propagator of the Lévy processes

It is now straightforward to determine the short-time propagator of the Lévy processes. We must replace the Gaussian distribution by the (multivariate) Lévy distribution $p_{\alpha,\beta}(\eta)$. As a consequence, we obtain the conditional probability, i.e., the short-time propagator, of the Lévy processes:

$$p(\mathbf{x}_{i+1}, t_i + \tau | \mathbf{x}_i, t_i) = \frac{1}{\text{Det}[g(\mathbf{x}_i, t_i)]} p_{\alpha,\beta} \left\{ \frac{1}{\tau^{1/\alpha}} [g(\mathbf{x}(t_i), t_i)]^{-1} [\mathbf{x}(t_{i+1}) - \mathbf{x}(t_i) - \tau \mathbf{N}(\mathbf{x}(t_i))] \right\}. \quad (2.34)$$

2.2.5. Joint probability distribution and Markovian properties

Due to the statistical independence of the random vectors $\Gamma(t_i)$ and $\Gamma(t_j)$ for $i \neq j$, we obtain the joint probability distribution as a product of the distributions $p(\beta)$:

$$p(\Gamma_N, \dots, \Gamma_0) = p(\Gamma_N) p(\Gamma_{N-1}) \cdots p(\Gamma_0). \quad (2.35)$$

Furthermore, we observe that under the assumption that the random vector $\Gamma(t_i)$ is independent of the variables $\mathbf{X}(t_j)$ for all $j \leq i$, we can construct the N -time probability distribution

$$p(\mathbf{x}_n, t_n; \cdots; \mathbf{x}_1, t_1; \mathbf{x}_0, t_0) = p(\mathbf{x}_n, t_n | \mathbf{x}_{n-1}, t_{n-1}) \cdots p(\mathbf{x}_1, t_1 | \mathbf{x}_0, t_0) p(\mathbf{x}_0, t_0). \quad (2.36)$$

However, this is the definition of a Markov chain. Therefore, the transition probabilities are the short-time propagators, i.e., the representation (2.34) is valid in the short-time limit, $\tau \rightarrow 0$. The probability distribution (2.34) is the discrete approximation of the *path integral representation* of the stochastic process under consideration [14].

Let us summarize: the statistical description of the Langevin equation based on the N -times joint probability distribution leads to the representation in terms of the conditional probability distribution. This representation is the definition of a Markov process. Due to the assumptions on the statistics of the fluctuating forces, different processes arise. If the fluctuating forces are assumed to be Gaussian, the short-time propagator is Gaussian and, as a consequence, solely defined by the drift vector and the diffusion matrix. If the fluctuating forces are assumed to be Lévy-distributed, more complex short-time propagators arise [69].

We also remark that,

(a) The assumption of Gaussianity of the statistics of the noise is not necessary. One can consider fluctuating forces with non-Gaussian probability distributions. In this case the probability distributions must be characterized by the higher-order moments, or, more explicitly, by their cumulants.

(b) The Markovian property, i.e., the fact that the propagator $p(\mathbf{x}_i, t_i | \mathbf{x}_{i-1} t_{i-1})$ does not depend on the states \mathbf{x}_k at times $t_k < t_i$ is usually violated by many physical systems, due to the fact that the noise sources become correlated for small time differences t_M , a point which has already been emphasized in the famous work of Albert Einstein on the Brownian motion, which is one of the first works on stochastic processes [76]. This time scale is called the Markov–Einstein time scale, and appears to be a highly interesting quantity, especially for nonequilibrium systems such as turbulence [28,77], and earthquakes [52].

2.3. Finite-time propagators

Up to now, we have considered the short-time propagators $p(\mathbf{x}_i, t_i | \mathbf{x}_{i-1}, t_{i-1})$ for infinitesimal time differences $t_i - t_{i-1} = \tau$. However, one is interested in the conditional probability distributions for finite time intervals, $p(\mathbf{x}, t | \mathbf{x}', t')$, $t - t' \gg \tau$. So, let us consider this limit.

2.3.1. The Fokker–Planck equation

The conditional probability distribution $p(\mathbf{x}, t | \mathbf{x}', t')$, with, $t - t' \gg \tau$, is obtained from the solution of the Fokker–Planck equation (also known as the second Kolmogorov equation, Kolmogorov, [78]) [14]:

$$\frac{\partial}{\partial t} p(\mathbf{x}, t | \mathbf{x}', t') = - \sum_{i=1}^d \frac{\partial}{\partial x_i} D_i^{(1)}(\mathbf{x}, t) p(\mathbf{x}, t | \mathbf{x}', t') + \frac{1}{2} \sum_{i,j=1}^d \frac{\partial^2}{\partial x_i \partial x_j} D_{ij}^{(2)}(\mathbf{x}, t) p(\mathbf{x}, t | \mathbf{x}', t'). \quad (2.37)$$

$\mathbf{D}^{(1)}$ and $\mathbf{D}^{(2)}$ are the drift vector and the diffusion matrix, respectively. By considering the Itô’s definitions of the stochastic integrals, the coefficients $\mathbf{D}^{(1)}$, $\mathbf{D}^{(2)}$ of the Fokker–Planck equation, Eq. (2.37), and the functionals \mathbf{N} and \mathbf{g} of the Langevin equation, Eqs. (2.1) and (2.2) are related by

$$D_i^{(1)}(\mathbf{x}, t) = N_i(\mathbf{x}, t), \quad (2.38)$$

$$D_{ij}^{(2)}(\mathbf{x}, t) = \sum_{l=1}^d g_{il}(\mathbf{x}, t) g_{jl}(\mathbf{x}, t). \quad (2.39)$$

They are defined according to

$$\begin{aligned} D_i^{(1)}(\mathbf{x}, t) &= \lim_{\tau \rightarrow 0} \frac{1}{\tau} \langle X_i(t + \tau) - x_i \rangle \Big|_{\mathbf{X}(t)=\mathbf{x}} \\ &= \lim_{\tau \rightarrow 0} \frac{1}{\tau} \int d\mathbf{x}' p(\mathbf{x}', t + \tau | \mathbf{x}, t) (x'_i - x_i) \end{aligned} \quad (2.40)$$

$$\begin{aligned} D_{ij}^{(2)}(\mathbf{x}, t) &= \lim_{\tau \rightarrow 0} \frac{1}{\tau} \langle (X_i(t + \tau) - x_i)(X_j(t + \tau) - x_j) \rangle \Big|_{\mathbf{X}(t)=\mathbf{x}} \\ &= \lim_{\tau \rightarrow 0} \frac{1}{\tau} \int d\mathbf{x}' p(\mathbf{x}', t + \tau | \mathbf{x}, t) (x'_i - x_i)(x'_j - x_j). \end{aligned} \quad (2.41)$$

These expressions demonstrate that the drift vector and the diffusion matrix are determined as the first and second moments of the conditional probability distributions $p(\mathbf{x}', t + \tau | \mathbf{x}, t)$ in the small time limit.

2.3.2. Fractional Fokker–Planck equations

The finite-time propagators or conditional probability distributions of stochastic processes containing Lévy noise lead to the fractional diffusion equations. For a discussion of this topic we refer the reader to [69].

2.4. Measurement noise

We can now go a step forward and include the measurement noise [79,80,83,84]. Due to the measurement noise, the observed state vector, which we denote by $\mathbf{Y}(t_i)$, is related to the stochastic variable $\mathbf{X}(t_i)$ by an additional noise term $\epsilon(t_i)$:

$$\mathbf{Y}(t_i) = \mathbf{X}(t_i) + \epsilon(t_i). \quad (2.42)$$

We assume that the stochastic variables $\epsilon(t_i)$ have zero mean and are statistically independent with probability density $p(\epsilon)$. Then, the probability distribution for the variable $\mathbf{Y}(t_i)$ is given by

$$p(\mathbf{y}_n, t_n; \dots; \mathbf{y}_0, t_0) = \int d\epsilon_n \dots d\epsilon_0 p(\mathbf{y}_n - \epsilon_n, t_n; \dots; \mathbf{y}_0 - \epsilon_0, t_0) p(\epsilon_n) p(\epsilon_{n-1}) \dots p(\epsilon_0). \quad (2.43)$$

Recently, it was shown that even strong external measurement noise, as well as the dynamical noise that is an intrinsic part of the dynamical process, can be quantified correctly, solely on the basis of the measured time series and proper data analysis [80].

3. Stochastic data analysis as a function of time

Complex systems are composed of a large number of subsystems that behave in a collective manner. In systems far from equilibrium collectivity arises due to self-organization [3,4]. It results in the formation of temporal, spatial, spatiotemporal, and functional structures. As discussed in Section 2, a complex system can be described in terms of the order parameters $X_i(t)$ that obey a set of stochastic differential equations of the form

$$dX_i = N_i[X_1, \dots, X_n]dt + \sum_j g_{ij}(X_1, \dots, X_n)dW_j, \quad (3.1)$$

where W_j are independent Wiener processes. Although the state vector $\mathbf{X}(t)$ of the complex system under consideration is high dimensional, its long time behavior is entirely governed by the dynamics of typically a few order parameters:

$$\mathbf{q}(t) = \mathbf{Q}(X_1, \dots, X_n). \quad (3.2)$$

For hydrodynamic instabilities in the laminar flow regime, such as the Rayleigh–Bénard convection or the Taylor–Couette experiment, thermal fluctuations are usually small and can be neglected. However, in nonlinear optics, and particularly in biological systems, the impact of noise has been shown to be of great importance. In principle, the equations for the order parameters can be derived from the basic equations that characterize the system under consideration close to instabilities [3]. However, if the basic equations are not available, as is the case, e.g., for systems considered in biology, the order parameter concept yields a top-down approach to complexity [4].

In the top-down approach the analysis of the experimental time series becomes a central issue. Methods of analysis of nonlinear time series (see, e.g., [8]) have been widely applied to analyze complex systems. However, such methods aim at the understanding of deterministic systems and can only be successful if the stochastic forces are weak. Thus, it appears that these methods must be extended in order to include stochastic processes. In Section 2 we provided the complete mathematical tools for deriving Eq. (3.1) from experimental (or computer simulation) time series.

The ultimate goal of analysis of nonlinear time series, applied to deterministic systems, is to extract directly the underlying nonlinear dynamical system from the measured time series in the form of a system of differential equations [8].

The role played by dynamic fluctuations has not been fully appreciated. Instead, noise has usually been considered as a random variable that is additively superimposed on a trajectory generated by a deterministic dynamical system. Noise has been usually considered as extrinsic or measurement noise.

The natural extension of the methods for the analysis of nonlinear time series to (continuous) Markov processes is the estimation of the *short-time propagators* from the time series. In recent years, it has become evident that such an approach is feasible. In fact, noise may help in the estimation of the deterministic ingredients of the dynamics. Due to the dynamical noise the system explores a larger part of the phase space and, thus, measurements of the series yield considerably more information about the dynamics as compared to the purely deterministic case, where the trajectories rapidly converge to attractors, hence providing only limited information.

The analysis of data sets of stochastic systems exhibiting Markov properties must be performed along the following path:

- Evaluating Markovian properties
- Determining the short-time propagators
- Reconstructing the data.

3.1. Markovian properties and Markov–Einstein time (length) scale

It is a difficult task, in principle, to decide by inspection whether some experimental data possess Markovian properties. The main point to emphasize is that such properties are usually violated in small time increments τ , as was pointed out above and by Einstein [76]. There are at least two reasons for this fact. First, the dynamical noise sources become correlated over small time differences. If we consider Gaussian noise sources, one usually observes an exponential decay of the correlations

$$\langle I_i(t) I_j(t') \rangle = \delta_{ij} \frac{1}{t_M} \exp(-|t - t'|/t_M). \quad (3.3)$$

Markovian properties may be expected to hold only for time increments, $\tau > t_M$. Second, measurement noise can spoil Markovian properties. Thus, estimation of the Markovian time scale t_M is a necessary step for stochastic data analysis. Several methods have been proposed for testing and detecting the Markov properties.

In general, an experimental data set is either stationary or nonstationary. Establishing or rejecting the stationarity of the set can be done in a straightforward manner, by measuring, e.g., the numerical stability (constancy) of the average and variance of the stochastic process $X(t)$ in a moving time window. For nonstationary processes one should study the ensemble averages. Quite often, one can investigate the “derivative” of the data set, $D(t) \equiv X(t + 1) - X(t)$, or its returns defined as, $R(t) \equiv \ln[X(t + 1)/X(t)]$ (if the data are positive numbers, such as the heart interbeat and the stock price). Frequently, the derivative or returns turn out to be stationary, since a drifting mean value that renders the time series nonstationary is subtracted.

As the first step we check whether the data follow a Markov chain and, if so, estimate the ME time (length) scale t_M (l_M). As is well known, a given process with a degree of randomness or stochasticity may have a finite or an infinite ME time (length) scale. The ME time (length) scale is the minimum time interval (length scale) over which the data can be considered as a Markov process. Here, we present three different methods of estimating the ME time scale.

Method 1: In this method, the ME time scale is estimated using the least squares test. The exact mathematical definition of the Markov process is given by [14],

$$p(x_k, t_k | x_{k-1}, t_{k-1}; \dots; x_1, t_1; x_0, t_0) = p(x_k, t_k | x_{k-1}, t_{k-1}).$$

Intuitively, the physical interpretation of a Markov process is that, it is a process with no memory; it “forgets” its past. In other words, only the most nearby condition of data, say (x_{k-1}, t_{k-1}) , is relevant to the probability of finding the system at a particular state x_k at time t_k . Thus, the ability to predict the value of $X(t)$ at time t is not enhanced by knowing its values in steps prior to the most recent one. Therefore, an important simplification for a Markov process is that, a conditional multivariate joint PDF can be written in terms of the products of the simple two-parameter conditional PDFs [14] as,

$$p(x_k, t_k; x_{k-1}, t_{k-1}; \dots; x_1, t_1 | x_0, t_0) = \prod_{i=1}^k p(x_i, t_i | x_{i-1}, t_{i-1}). \quad (3.4)$$

Testing Eq. (3.4) for large values of k is beyond the present computational capability. However, for $k = 3$, i.e., for three points, the relation,

$$p(x_3, t_3 | x_2, t_2; x_1, t_1) = p(x_3, t_3 | x_2, t_2), \quad (3.5)$$

should hold for any value of t_2 in the interval $t_1 < t_2 < t_3$.

A process is Markov with a ME time scale t_M , if Eq. (3.5) is satisfied for a *certain* time separation or interval. To measure the ME time scale, we use a fundamental theory of probability that allows us to write any three point PDF in terms of the conditional probability functions as,

$$p(x_3, t_3; x_2, t_2; x_1, t_1) = p(x_3, t_3 | x_2, t_2; x_1, t_1) p(x_2, t_2; x_1, t_1). \quad (3.6)$$

Using the properties of Markov processes, and substituting Eq. (3.6), we obtain,

$$p_{\text{Markov}}(x_3, t_3; x_2, t_2; x_1, t_1) = p(x_3, t_3|x_2, t_2)p(x_2, t_2|x_1, t_1). \quad (3.7)$$

We then compute the deviations of p_{Markov} from that given by Eq. (3.6), using the least squares method:

$$\chi^2 = \int dx_3 dx_2 dx_1 \frac{[p(x_3, t_3; x_2, t_2; x_1, t_1) - p_{\text{Markov}}(x_3, t_3; x_2, t_2; x_1, t_1)]^2}{\sigma^2 + \sigma_{\text{Markov}}^2} \quad (3.8)$$

where $\sigma^2 + \sigma_{\text{Markov}}^2$ is the sum of the variances of the terms in the denominator. One then takes, $t_1 = 0$ and $t_2 = t_3/2$ and plots the reduced χ^2 , $\chi_v^2 = \frac{\chi^2}{N}$ (N is the number of degrees of freedom), as a function of the time scale t_2 . The ME time scale is that value of t_2 at which χ_v^2 is minimum [85,48].

Method 2: The second method is based on the direct evaluation of the definition of Markovian properties (2.25), considering the higher-order conditional probability distributions:

$$\begin{aligned} p(x_3, t_3|x_2, t_2; x_1, t_1) &= \frac{p(x_3, t_3; x_2, t_2; x_1, t_1)}{p(x_2, t_2; x_1, t_1)} \\ &= p(x_3, t_3|x_2, t_2). \end{aligned} \quad (3.9)$$

This procedure is feasible if used for large data sets. Due to the different conditioning, both probabilities are typically based on different numbers of events. As an appropriate method to show the similarity of (3.9), the Wilcoxon test has been proposed [87,29,38]. In principle, higher-order conditional probability distributions should be considered in a similar way, which becomes numerically intractable. However, the validity of relation (3.9) is a strong indication that the data set possesses Markovian properties (see also [49]).

Method 3: An indirect way is to use the Chapman–Kolmogorov equation, Eq. (2.26), the validity of which for describing the probabilities is a necessary condition for Markovian properties. The method is based on a comparison between the conditional PDF

$$p(x_k, t_k|x_i, t_i) \quad (3.10)$$

taken from the experiment and the one calculated by the Chapman–Kolmogorov equation

$$p(x_k, t_k|x_i, t_i) = \int dx_j p(x_k, t_k|x_j, t_j)p(x_j, t_j|x_i, t_i) \quad (3.11)$$

where t_j is an intermediate time $t_i < t_j < t_k$. A refined method can be based on an iteration of the Chapman–Kolmogorov equation, i.e., considering several intermediate times. If the Chapman–Kolmogorov equation is not satisfied, deviations from it are enhanced by each iteration. The conditional PDF $p(x_k, t_k|x_i, t_i)$ can be estimated via several methods such as parametric (Maximum Likelihood estimation of a Gaussian model), non-parametric (Histogram, Kernel based and K-nearest neighbor) and semi-parametric methods (EM algorithm and gradient based optimization).

3.2. Estimation of drift and diffusion coefficients

We now describe an operational approach, which allows one to estimate the drift vector and the diffusion matrix from data. We discuss the case in which the averages are taken with respect to an ensemble of experimental realizations of the stochastic process under consideration, in order to include nonstationary processes in the discussions. Replacing the ensemble averages by time averages for statistically stationary processes is straightforward. The procedure is as follows:

- The data is represented in a d -dimensional phase space
- The phase space is partitioned into a set of finite, but small d -dimensional volume elements.
- For each bin (denoted by α), located at point \mathbf{x}_α of the partition we consider the quantity

$$\mathbf{x}(t_j + \tau) = \mathbf{x}(t_j) + \mathbf{D}^{(1)}(\mathbf{x}(t_j), t_j)\tau + \sqrt{\tau}g(\mathbf{x}(t_j), t_j)\Gamma(t_j). \quad (3.12)$$

Therefore, the considered points $\mathbf{x}(t_j)$ are taken from the bin located at \mathbf{x}_α . Since we consider time-dependent processes, this must be done for each time step t_j separately.

3.2.1. Estimation of the drift vector

The drift vector assigned to the bin located at \mathbf{x}_α is determined as the small τ -limit of

$$\mathbf{D}^{(1)}(\mathbf{x}_\alpha, t) = \lim_{\tau \rightarrow 0} \frac{1}{\tau} \mathbf{M}^{(1)}(\mathbf{x}_\alpha, t, \tau) \quad (3.13)$$

of the conditional moment

$$\mathbf{M}^{(1)}(\mathbf{x}_\alpha, t_j, \tau) = \frac{1}{N_\alpha} \sum_{\mathbf{x}(t_j) \in \alpha} [\mathbf{x}(t_j + \tau) - \mathbf{x}(t_j)]. \quad (3.14)$$

The sum is over all the N_α points contained in the bin α .

Proof. The drift vector assigned to the bin α located at \mathbf{x}_α is approximated by the conditional expectation value

$$\mathbf{M}^{(1)}(\mathbf{x}_\alpha, t, \tau) = \tau \frac{1}{N_\alpha} \sum_{\mathbf{x}(t_j) \in \alpha} \mathbf{D}^{(1)}(\mathbf{x}_j, t_j) + \sqrt{\tau} \frac{1}{N_\alpha} \sum_{\mathbf{x}(t_j) \in \alpha} g(\mathbf{x}(t_j), t_j) \Gamma(t_j). \quad (3.15)$$

Therefore, the sum is over all points $\mathbf{x}(t_j)$ located in the bin assigned to \mathbf{x}_α . Assuming that $\mathbf{D}^{(1)}(\mathbf{x}, t)$ and $g(\mathbf{x}, t)$ do not vary significantly within the bin, the second contribution drops out since

$$\frac{1}{N_\alpha} \sum_{\mathbf{x}_j \in \alpha} \Gamma(t_j) \rightarrow 0. \quad \square \quad (3.16)$$

3.2.2. Estimation of the diffusion matrix

The diffusion matrix is estimated by the small τ -limit of

$$\mathbf{D}^{(2)}(\mathbf{x}_\alpha, t) = \lim_{\tau \rightarrow 0} \frac{1}{\tau} \mathbf{M}^{(2)}(\mathbf{x}_\alpha, t, \tau) \quad (3.17)$$

of the conditional second moment

$$\mathbf{M}^{(2)}(\mathbf{x}_\alpha, t, \tau) = \frac{1}{N_\alpha} \sum_j \{[\mathbf{x}(t_j + \tau) - \mathbf{x}(t_j)] - \tau \mathbf{D}^{(1)}(\mathbf{x}_j, t_j)\}^2. \quad (3.18)$$

Proof. We consider the quantity

$$\mathbf{M}^{(2)}(\mathbf{x}_\alpha, t, \tau) = \tau \frac{1}{N_\alpha} \sum_{\mathbf{x}(t_k) \in \alpha} \sum_k g(\mathbf{x}(t_k), t_k) \Gamma(t_k) g(\mathbf{x}(t_j), t_j) \Gamma(t_j). \quad (3.19)$$

If the bin size is small compared to the scale in which the matrix $g(\mathbf{x}, t)$ varies significantly, we can replace $g(\mathbf{x}(t_k), t_k)$ by $g(\mathbf{x}_\alpha, t_k)$ such that

$$\begin{aligned} \mathbf{M}^{(2)}(\mathbf{x}_\alpha, t, \tau) &= \tau g(\mathbf{x}_\alpha, t_k) \left[\frac{1}{N_\alpha} \sum_{\mathbf{x}_j \in \alpha} \sum_{\mathbf{x}_k \in \alpha} \Gamma(t_k) \Gamma(t_j) \right] g^T(\mathbf{x}_\alpha, t_k) \\ &= \tau g(\mathbf{x}_\alpha, t_k) g^T(\mathbf{x}_\alpha, t_k). \end{aligned} \quad (3.20)$$

Here, we have used the assumption of the statistical independence of the fluctuations

$$\frac{1}{N_\alpha} \sum_{\mathbf{x}(t_j) \in \alpha} \sum_{\mathbf{x}(t_k) \in \alpha} \Gamma(t_k) \Gamma(t_j) = \delta_{kj}. \quad \square \quad (3.21)$$

3.2.3. Higher-order cumulants

In a similar way one may estimate higher cumulants $M^{(n)}$ that, in the small time limit converge to the so-called Kramers–Moyal coefficients [14,88,89]. The estimation of such quantities allows one to answer the question of whether the noise sources actually are Gaussian-distributed random variables.

3.2.4. Lévy processes

A procedure to analyze Lévy processes along the same lines has been proposed by [90]. An important point here is the determination of the Lévy parameter α .

3.2.5. Differentiating between stochastic process and noise data

Looking at the joint statistics of the increments extracted from given data, it may be shown that nesting of the increments and the resulting statistics can be used to differentiate between noise-like data sets and those resulting from stochastic processes [91].

3.2.6. Estimation of the drift and diffusion coefficients from sparsely sampled time series

As we have already discussed, the results of an analysis of data sets can be reconsidered self-consistently. This fact can be used to extend the procedure to data sets with insufficient amount of data, or sparsely sampled time series, for which the estimation of the conditional moments $M^{(n)}(\mathbf{x}, t, \tau)$ and the subsequent limiting procedure $\tau \rightarrow 0$ cannot be performed accurately.

In this case, one may proceed as follows. In a first step one obtains a zeroth-order approximation of the drift vector $\mathbf{D}^{(1)}(\mathbf{x})$ and the diffusion matrix $\mathbf{D}^{(2)}(\mathbf{x})$. Based on the estimates one performs, as the second step, a suitable ansatz for the drift vector and the diffusion matrix that contain a set of free parameters σ

$$\mathbf{D}^{(1)}(\mathbf{x}, \sigma), \mathbf{D}^{(2)}(\mathbf{x}, \sigma) \quad (3.22)$$

that defines a class of the Langevin equations. Each Langevin equation is related with a joint probability distribution

$$p(\mathbf{x}_n, t_n; \dots; \mathbf{x}_1, t_1; \sigma). \quad (3.23)$$

The joint probability distribution can be compared with the experimental one, $p(\mathbf{x}_n, t_n; \dots; \mathbf{x}_1, t_1; \text{exp.})$. The best representative of the class of the Langevin equations for the reconstruction of experimental data is then obtained by minimizing a suitably defined distance between the two distributions:

$$\text{Dist}\{p(\mathbf{x}_n, t_n; \dots; \mathbf{x}_1, t_1; \sigma) - p(\mathbf{x}_n, t_n; \dots; \mathbf{x}_1, t_1; \text{exp.})\} = \text{Min.} \quad (3.24)$$

A reasonable choice is the so-called Kullback–Leibler distance between two distributions, defined as

$$K = \int dx_1 dx_2 \dots dx_n p(\mathbf{x}_n, t_n; \dots; \mathbf{x}_1, t_1, \text{exp.}) \ln \frac{p(\mathbf{x}_n, t_n; \dots; \mathbf{x}_1, t_1, \text{exp.})}{p(\mathbf{x}_n, t_n; \dots; \mathbf{x}_1, t_1; \sigma)}. \quad (3.25)$$

It was shown recently how the iteration procedure can be obtained from the maximum likelihood arguments. For more details, we refer the reader to [92,83,84]. A technical question concerns the determination of the minimum, [93] used the limited-memory Broyden–Fletcher–Goldfarb–Shanno algorithm for constraint problems, in order to determine the solution of the optimization problem. Estimation of Kramers–Moyal coefficients in short and nonstationary data sets has been investigated by [94–99].

3.2.7. Multiscale construction of time series

Nawroth et al. introduced a method which allows a reconstruction of time series based on higher-order multiscale statistics given by a hierarchical process [100]. This method is able to model the time series not only on a specific scale but for a range of scales. It is possible to generate complete new time series, or to model the next steps for a given sequence of data. The method itself is based on the joint probability density which can be extracted directly from given data, thus no estimation of parameters is necessary. The unconditional and conditional probability densities of the original and reconstructed time series are compared and the ability to reproduce both is demonstrated [101].

3.2.8. Mapping stochastic processes onto complex networks

Recently Shirazi et al., proposed a general method by which a given stochastic process is mapped onto a complex network with distinct geometrical properties [103]. The relation between the statistical properties of the stochastic time series, such as the intermittency and correlation length, and their stochastic behavior, as well as the properties of their equivalent networks, are then studied. They showed that for such processes the corresponding time series can be reconstructed with high precision by means of a random walk on the network equivalent, see also [104–106].

3.3. Level-crossing analysis of time series

In this subsection we provide the relation between the average frequency of crossing of the positive slope ν_α^+ for a time series $X(t)$, and the drift and diffusion coefficients of the underlying stochastic process. The level crossing has been introduced in the context of stochastic processes [64,65], rough surfaces [66] and stock markets [107,108], fluctuations of the velocity fields in the Burgers turbulence, and in the Kardar–Parisi–Zhang equation in [109,67]. The level-crossing analysis of a data set has the advantage that, it yields very important global properties of the time series, without any need for a scaling feature in the data set.

The level-crossing analysis is the complementary method to the other well-known methods such as the detrended fluctuation analysis (DFA) [110–119], detrended moving average (DMA) [120,121], wavelet transform modulus maxima (WTMM) [122], rescaled-range analysis (R/S) [123,124], scaled windowed variance (SWV) [125], detrended cross-correlation analysis [126], multifactor analysis of multiscaling [127], etc., and is very easy to apply to any data set and does not require a lot of computing efforts and computing time. For example, it is well known that the R/S, SWV and other non-detrending methods work well if the records are long and do not involve trends. Moreover, in the detrending method one must be aware that, in some cases, there exist one or more crossover (time) scales that separate regimes with different scaling exponents [116,117,119]. In this case the investigation of the scaling behavior is more complex, as different scaling exponents are required for different parts of the series [128,129]. Therefore, one needs a multitude of scaling exponents (known as the multifractal exponents or dimensions) for a full description of the scaling behavior. Generally, the crossover usually arises either because of the changes in the correlation properties of the series at different time (space) scales, or often arises from the trends in the data.

The level-crossing analysis is sensitive to the correlation when the time series is shuffled, and to the PDF with fat tails when the time series is surrogated [107]. The long-range correlations are destroyed by the shuffling procedure. In the

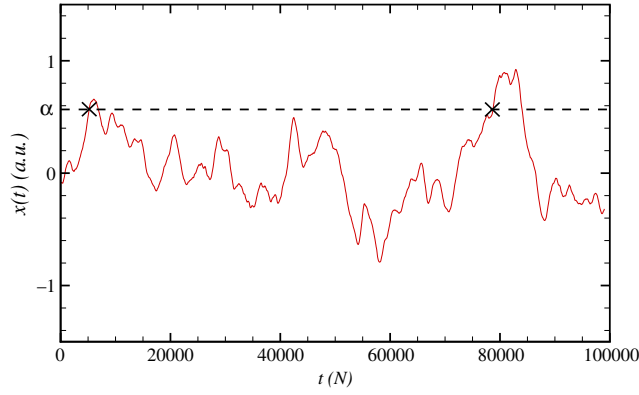


Fig. 2. Positive slope crossing in a fixed α level.

surrogate method the phase of the discrete Fourier transform coefficients of the time series are replaced by a set of pseudo-independent random variables, distributed uniformly in $(-\pi, +\pi)$. The correlations in the surrogate series do not change, but the PDF changes to Gaussian distribution [130–133]. Our aim for using the level-crossing method is to characterize the statistical properties of the data set, with the hope of gaining better understanding of the underlying stochastic dynamics.

We consider a time series of length n given by $\{x(t_1), x(t_2), \dots, x(t_n)\}$. Let N_α^+ denote the number of positive slope crossing of $x(t) - \bar{x} = \alpha$ for the interval T (see Fig. 2). Since the process is stationary (or homogeneous), if we take a second time interval of T immediately following the first, we will obtain the same result and, therefore, for the two intervals together we obtain, $N_\alpha^+(2T) = 2N_\alpha^+(T)$, from which it follows that, the average number of the crossing is proportional to the time interval T . Hence, $N_\alpha^+(T) \propto T$, or, $N_\alpha^+(T) = \nu_\alpha^+ T$, where ν_α^+ is the average frequency of positive slope crossing of the level α .

We now describe how the frequency ν_α^+ is deduced from the underlying PDFs for $x(t) - \bar{x}$. Using the drift and diffusion coefficients, we calculate the frequency of the level crossing at a given level α . Let ν_α^+ denote the number of positive-difference crossing of $x(t) - \bar{x} = \alpha$ (assuming $\bar{x} = 0$) for the interval T , which can be written in terms of the joint cumulative probability distribution, $\Pi(x(i) > \alpha, x_{i-1} < \alpha)$ as [41],

$$\begin{aligned} \nu_\alpha^+ &= \Pi(x_i > \alpha, x_{i-1} < \alpha) = \int_{-\infty}^\alpha \int_\alpha^\infty p(x_i, x_{i-1}) dx_i dx_{i-1} \\ &= \int_{-\infty}^\alpha \int_\alpha^\infty p(x_i | x_{i-1}) p(x_{i-1}) dx_i dx_{i-1}. \end{aligned} \tag{3.26}$$

The joint PDF, $p(x_i | x_{i-1})$ is given by the above equation in which $\Delta t = 1$,

$$p(x', t + \Delta t | x, t) = \frac{1}{2\sqrt{\pi D^{(2)}(x', t) \Delta t}} \times \exp\left[-\frac{(x' - x - D^{(1)}(x', t) \Delta t)^2}{4D^{(2)}(x', t) \Delta t}\right]; \tag{3.27}$$

where the PDF $p(x_{i-1})$ is given by,

$$p(x_{i-1}) = p(x) = \frac{N}{D^{(2)}(x)} \exp\left[\int^x \frac{D^{(1)}(x')}{D^{(2)}(x')}\right],$$

and N is the normalization constant [14].

For the case of continuous time the average level crossing ν_α^+ can be written in terms of joint PDF of x and x' , where x' is the time (space) derivative of stochastic series [64,65]. It can be shown that ν_α^+ satisfies the following relation in terms of the joint PDF $p(x, x')$:

$$\nu_\alpha^+ = \int_0^\infty p(\alpha, x') x' dx', \tag{3.28}$$

where, $x' = dx/dt$. In the next sections we will evaluate the precision of the results for the level-crossing analysis in the context of the oil price fluctuations. We can also define the quantity N_{tot}^+ that is given by, $N_{\text{tot}}^+ = \int_{-\infty}^\infty \nu_\alpha^+ d\alpha$, and measure the total number of crossing the series with positive slope. We will discuss the quantity N_{tot}^+ more in Section 5, in the context of rough surfaces.

3.3.1. Numerical aspects and precision

To estimate the drift and diffusion coefficients we note that the bin size influences the results. The bin size should allow for a reasonable number of events, such that the sums converge. It should, however, be reasonably small in order to allow for an accurate resolution of the drift vector and the diffusion matrix. Moreover, the data should allow for the estimation of the conditional moments in the limit, $\tau \rightarrow 0$ [134,135]. Here, a finite Markov–Einstein coherence length may cause problems. From the studies of the properties of the Fokker–Planck equation much is known on the τ -dependence of the conditional moments. This may be used for further improved estimations, as has been discussed by [136,88,89]. Furthermore, as we shall discuss below, extended estimation procedures have been devised, which overcome the problems associated with the small τ limit.

Indeed, the Langevin equation, Eq. (3.12), enables us to *reconstruct* a stochastic time series $x(t)$, which is similar to the original one *in the statistical sense*. However, the stochastic process that is reconstructed by iterating Eq. (3.12) yields a series of data *without memory*. To compare the regenerated data with the original ones, we must take the temporal interval in the numerical discretization of Eq. (3.12) to be unity (or normalize it to unity). However, the ME time scale is typically greater than unity. Therefore, we correlate the data over the ME time scale t_M , for which there are a number of methods [30,85,86].

3.3.2. Self-consistency

After determining the drift vector and the characteristics of the noise sources from data, it is straightforward to synthetically generate data sets by iterating the corresponding stochastic evolution equations. Subsequently, their statistical properties can be compared with the properties of the actual data. This yields a self-consistent check of the results. For a detailed discussion we refer the reader to [20].

4. Stochastic data analysis in length scale

In the case of self-similar structures, complexity is commonly investigated by a local measure $q(r, t)$ that characterizes the structure on the scale r and at the time (or position) t . The local measure can be defined as increment ΔX or as the absolute value of the increment $|\Delta X|$, what is also commonly used. Self-similarity means that in a certain range of r the processes

$$q(r, t), \quad \lambda^\xi q(\lambda r, \lambda^\gamma t) \quad (4.1)$$

should have the same statistics. The exponent γ is known as dynamical exponent [137]. More precisely, the probability distribution of the quantity q takes the form

$$p(q, r) = r^{-\xi} F(q/r^\xi), \quad (4.2)$$

with a universal function $F(Q)$. Furthermore, the moments exhibit scaling behavior,

$$\langle q^n(r) \rangle = \int dq \quad q^n \frac{1}{r^\xi} F(q/r^\xi) = Q_n r^{n\xi}. \quad (4.3)$$

Such properties have been called *fractal scaling behavior*.

There are many experimental examples of real systems, such as turbulent fields or surface roughness, just to mention two, for which such a simple picture of a complex structure is only a rough, first approximation. In fact, particularly for turbulence for which $q(r, t)$ is taken as a velocity increment, it has been argued that *multifractal behavior* is more appropriate, where the n th-order moments scale according to

$$\langle q^n(r) \rangle = Q_n r^{\zeta(n)}, \quad (4.4)$$

where the scaling indices $\zeta(n)$ are nonlinear functions of the order n ,

$$\zeta(n) = n\xi_0 + n^2\xi_1 + n^3\xi_2 + \dots \quad (4.5)$$

Such a relation can formally be obtained by assuming that the probability distribution $f(q, r)$ has the following form

$$p(q, r) = \int d\xi \quad p(\xi, r) \frac{1}{r^\xi} F(q/r^\xi). \quad (4.6)$$

This above formula is based on the assumption that in a data set, regions with different scaling indices ξ exist, where $p(\xi, r)$ provides a measure of the scaling indices ξ at scale r . The major shortcoming of the fractal and multifractal approaches to complexity in scale is the fact that, they only address the statistics of the measure $q(r, t)$ at a single scale r . In general though, one expects $q(r, t)$ and $q(r', t)$ to depend on the scales considered. The question, which we will address in the following, arises as to whether there exist methods that lead to a more comprehensive characterization of the scale disorder by the general joint statistics

$$p(q_N, r_N; q_{N-1}, r_{N-1}; \dots; q_1, r_1; q_0, r_0) \quad (4.7)$$

of the local measure q at multiple scales r_i .

4.1. The Langevin dynamics in scale

Processes that depend on time and scale can be analyzed in a similar way, if we generalize the time process given by [3] to a stochastic equation evolving in scale

$$q(r + dr) = q(r) + N(q, r)dr + g(q, r)dW(dr) \quad (4.8)$$

where dW belongs to a random process. The aim of the data analysis is then to disentangle deterministic dynamics and the impact of fluctuations. Loosely speaking, this amounts to detect *trends* and *chances* in data series of complex systems.

A complete analysis of experimental data, which is generated by the interplay of deterministic dynamics and dynamical noise, has to address the following issues

- Identification of the order parameters
- Extracting the deterministic dynamics
- Evaluating the properties of the fluctuations

In the following, we summarize the description of stochastic processes in scale, focusing mainly on their Markovian nature.

4.2. Deformation of the PDF on scale and cascade of information, from large to small scales

One of the main properties of almost all the data sets is their small-scale intermittency. Its qualitative signature is the non-Gaussian shape of the PDF of the increments defined by, $\Delta X(r) = X(t+r) - X(t)$, for given r . The stretched exponential-like tail of the PDF of $\Delta X(r)$ changes when the distance r decreases from the largest inertial scales to the smallest dissipation ones. Using stochastic analysis one can analyze the data and investigate its intermittency behavior as pointed out by [10,30]. They studied the evolution of the PDF of several stochastic properties, such as turbulent free jets, and rough surfaces, and showed that the conditional PDF of the *increments* of a stochastic field, such as the increments in the velocity field in the turbulent flow or heights fluctuations of the rough surface, satisfies the Chapman–Kolmogorov equation. This enables one to derive a Fokker–Planck equation for describing the systems under study. We now describe the conditions under which such a formulation can be utilized.

One computes the drift and diffusion coefficients or, more generally, the Kramers–Moyal (KM) coefficients, for the *increments* of time series, $\Delta X(r) = X(t+r) - X(t)$, and check whether the first and second KM coefficients that represent, respectively, the drift and diffusion coefficients of the Fokker–Planck equation, have well-defined and finite values, while the third- and fourth-order KM coefficients are small (theoretically, they should be zero). According to the Pawula theorem [14], the KM expansion,

$$-\frac{\partial}{\partial r}p(\Delta X, r|\Delta X_0, r_0) = \sum_{k=1}^{\infty} \left(-\frac{\partial}{\partial \Delta X}\right)^k [D^{(k)}(\Delta X, r)p(\Delta X, r|\Delta X_0, r_0)], \quad (4.9)$$

can be truncated after the second (diffusive) term, provided that the fourth-order coefficient $D^{(4)}$ vanishes. If so, which is often the case, then the KM expansion, Eq. (4.9), reduces to a Fokker–Planck evolution equation. In that case, the Fokker–Planck equation is numerically constructed (by computing the drift and diffusion coefficients) for the PDF $p(\Delta X, r)$ that, in turn, is used to gain information on evolution of the shape of the PDF as a function of the time scale r . The negative sign of the left hand side of Eq. (4.9) is due to the direction of the cascade from large to smaller length scale r . In essence, if the first two KM coefficients are found to have numerically meaningful values (i.e., not very small), while the third and higher coefficients are small (compared with the first two coefficients), the above reconstruction method, can be also used for the *increments* of the times series.

Using the increments one can investigate one of the most important issues in the time series, which is the intermittent behavior of the fluctuations in various scaling region. Intermittency is known as the structures that arise in a random data set and manifest themselves as high peaks at random time or length scales. The intervals between them are characterized by a low intensity and a large size. Rare peaks are the hallmarks of PDF's non-Gaussian tails. Such strongly non-Gaussian activities are responsible for the information cascade from large to small scales. Intermittency is usually analyzed by means of the statistical properties of the increments, $\Delta X(r) = X(t+r) - X(t)$ [55]. The overwhelming experimental and theoretical studies have been brought forward for characterization of the structure functions, i.e., $S_p(r) = \langle [\Delta X(r)]^p \rangle$.

For this case the method has been used as an alternative description of the multifractal behavior. Multifractals are usually analyzed by looking at the fluctuating quantities, such as the velocity increments, temperature increments, etc., at each scale separately as a random variable. The motivation for multifractal investigation is related to the fact that, the complexity of most disordered systems depends on the scale at which they are observed. The derived Fokker–Planck evolution operator for the PDF of the increments also yields important information about the changing shape of the distribution as a function of the time interval r . In Section 6 we derive the relation between the Kramers–Moyal coefficients and the structure functions $S_p(r)$, for scale-invariant series, such as turbulence.

4.2.1. Multiscale correlation functions

As mentioned above, one of the most important issues in stationary time series is the intermittent behavior of the small-scale fluctuations. Recently, it was proposed [59,60,138] that it would be more natural for scale-invariant series to look at

the correlations in the fluctuations of a time series increments at various scales:

$$\mathcal{F}_n(r|r_1, r_2, \dots, r_n) = \langle \Delta_{r_1} X(t) \Delta_{r_2} X(t) \cdots \Delta_{r_n} X(t) \rangle \quad (4.10)$$

where all the scales r_i are within the scaling region. Writing $\mathcal{F}_n(t|r_1, r_2, \dots, r_n)$ in terms of the structure function of each increment is known as the *fusion rules* [59,60,57,58,138]. The fusion rules describe the asymptotic properties of the n -point correlation functions, when some of the coordinates approach one. The fusion rules have been tested experimentally only for turbulence data, and good agreement between experiment and theory has been observed [62,61]. If $p < n$ pairs of the coordinates of a time series increments merge, with the typical separations $r_i \sim r$ for $i \leq p$ and the remaining separation on the order of R , such that R belongs to the scaling region, the fused multiscale correlation is defined by

$$\begin{aligned} \mathcal{F}_{p+q}(r, R) &\equiv \langle [X(t+r) - X(t)]^p [X(t+R) - X(t)]^q \rangle \\ &\equiv \langle [\Delta_r X(t)]^p [\Delta_R X(t)]^q \rangle. \end{aligned} \quad (4.11)$$

In this section we show that the multiscale correlation functions for a wide class of processes can be written as

$$\mathcal{F}_{p+q}(r, R) \sim S_p(r) S_{p+q}(R) / S_p(R) \quad (4.12)$$

where $S_p(r) = \langle [\Delta_r \mathbf{X}(t)]^p \rangle$.

Suppose that one is able to determine all the Kramers–Moyal coefficients and, therefore, the solution of Eq. (4.9) for $p(X_r, r)$ can obviously be written as a scale-ordered exponential [14],

$$p(X_r, r) = \mathcal{T} \left(e_+^{\int_{r_0}^r dr' L_{KM}(X_{r'}, r')} p(X_0, r_0) \right)$$

where L_{KM} is the Kramers–Moyal (KM) evolution operator, and we have defined $X_r = \Delta_r X(t)$. Using the properties of the scale-ordered exponentials, the conditional probability density will satisfy the Chapman–Kolmogorov equation. Equivalently, we derive that the probability density and, as a result, the conditional probability density of increments satisfy a KM evolution equation:

$$-\frac{\partial p}{\partial r} = \sum_{n=1}^{\infty} (-1)^n \frac{\partial^n}{\partial X_r^n} [D^{(n)}(X_r, r) p]. \quad (4.13)$$

The coefficients $D^{(n)}(X_r, r)$ are the small-scale limit of the conditional moments [14]. They fully characterize the statistics of the fluctuations as:

$$D^{(n)}(X_2) = \lim_{r_1 \rightarrow r_2} \frac{1}{r_1 - r_2} \int (X_1 - X_2)^n p(X_1, r_1 | X_2, r_2) dX_1.$$

The KM coefficients are the main observable of a Markov process, from which all the terms in the KM operator are determined. As mentioned before, it is a well-known theorem – the Pawula theorem [14] of Markov processes – that whenever the fourth-order KM coefficient tends to zero, all the other terms with higher-order derivatives also tend to zero. So, the distinction between Markov processes and the Fokker–Planck description when only the first two terms in the evolution operator in scale are important should be kept in mind. Thanks to the detailed analysis carried over experimental data, one can obtain the functional form of all the KM coefficients.

Recalling the original idea for suggesting the Markovian property of the increments cascade in scale, we take a step further and calculate the more general objects of the cascade, i.e., the unfused multiscale correlations. Assuming the Markovian nature of the increments in scale and the proposed form of the evolution operator $L_{KM}(X, r)$, one can, in principle, calculate any correlation among the increments in different scales [63]:

$$\mathcal{F}_n(X|r_1, r_2, \dots, r_n) = \langle X(r_1) X(r_2) \cdots X(r_n) \rangle = \int dX(r_1) \cdots dX(r_n) X(r_1) \cdots X(r_n) p(X_1, r_1; X_2, r_2; \cdots; X_n, r_n).$$

The joint probability $p(X_1, r_1; X_2, r_2; \cdots; X_n, r_n)$ can be calculated by taking advantage of the Markovian property in terms of the conditional probabilities, i.e.,

$$p(X_1, r_1; X_2, r_2; \cdots; X_n, r_n) = p(X_1, r_1 | X_2, r_2) \times p(X_2, r_2 | X_3, r_3) \cdots p(X_{n-1}, r_{n-1} | X_n, r_n) p(X_n, r_n). \quad (4.14)$$

The conditional PDF of the increments is then written as a scalar-ordered operator as

$$p(X_1, \lambda_1 | X_2, \lambda_2) = \mathcal{T} \left(e_+^{\int_{\lambda_2}^{\lambda_1} d\lambda L_{KM}(X_1, \lambda)} \right) \delta(X_1 - X_2)$$

where $\lambda_1 = \ln(L/r)$ and $\lambda_2 = \ln(L/R)$. Therefore, in the calculation of the n -point multiscale correlations a series of conditional operators would emerge in the integrand of (4.14). When some of the coordinates coalesce, the conditional operator tends to a dirac delta function. The reduction of the conditional probability between the coalescing coordinates simplify the calculations. The only remaining conditional operator will be the probability of observing the typical increment X_1 between one subclass of fused points, conditioned on observing the typical increment X_2 in the other subclass of fused

points. Explicitly, we examine the behavior of $\mathcal{F}_{p+q}(\lambda_1, \lambda_2)$ defined in Eq. (4.10), where $\lambda_1 = \ln(L/r)$, $\lambda_2 = \ln(L/R)$, and L is the size of the data.

$$\mathcal{F}_{p+q}(\lambda_1, \lambda_2) = \langle X^p(\lambda_1)X^q(\lambda_2) \rangle = \int dX_1 dX_2 \delta(X_1 - X_2) p(X_2, \lambda_2) (e^{-(\lambda_1 - \lambda_2) L_{KM}^1(X_1)} X_1^p X_2^q). \quad (4.15)$$

For the case in which the fourth KM coefficients are small compared with the first and second coefficients, the KM equation with a Fokker–Planck evolution kernel is interpreted as if the increment X is evaluated in “scale” λ (logarithmic time scale) by the Langevin equation,

$$\frac{\partial X}{\partial \lambda} = \tilde{D}^{(1)}(X, \lambda) + \sqrt{\tilde{D}^{(2)}(X, \lambda)} \Gamma(\lambda) \quad (4.16)$$

where $\Gamma(\lambda)$ is a white noise, and the diffusion term acts as a multiplicative noise. Resorting to the Ito’s prescription, the multipoint correlation function can be written in the form of a path integral as

$$\mathcal{F}(\lambda_1, \lambda_2) = \int \mathcal{D}X X^p(\lambda_1) X^q(\lambda_2) e^{\int_{\lambda_1}^{\lambda_2} \left(\frac{\partial X}{\partial \lambda} - D^1(X, \lambda) \right) d\lambda} p(X_2, \lambda_2). \quad (4.17)$$

By a simple application of the Bayesian rule, the probability density in the outer scale λ_2 is also written as a path integral entering the information of the integral scale PDF. Building up all the terms in a descriptive way, the joint probability $p(X_1, \lambda_1; X_2, \lambda_2)$ is represented as a path integral over all the possible *paths* between $X(\lambda_1)$ and $X(\lambda_2)$, transferring in an intermittent way all the information of the integral scale to the calculation. Without further attempt for calculating the multiscale correlations by path integral representation, we turn our attention to the Langevin dynamics instead.

4.2.2. Multipliers

Almost all the experimental data with scaling behavior satisfy the following expression for the drift and diffusion coefficients, $D^{(1)}(X) = -\alpha_1(\lambda)X$, and, $D^{(2)}(X) = \alpha_2(\lambda)X^2$, (with very small $D^{(n)}(X)$, for $n \geq 3$), where the resulting process can be approximate by the well-known Black–Scholes multiplicative process [14]. Using the Ito prescription, one can deduce that

$$\Delta_{\lambda_1} X(t) = \mathcal{W}(\lambda_1, \lambda_2) \Delta_{\lambda_2} X(t). \quad (4.18)$$

The multiplier $\mathcal{W}(\lambda_1, \lambda_2)$ can be easily derived in terms of α_1 and α_2 and Wiener process, W , at two logarithmic scales as [63],

$$\mathcal{W}(\lambda_1, \lambda_2) = \exp \left[\left(-\alpha_1 - \frac{\alpha_2}{2} \right) (\lambda_1 - \lambda_2) + \sqrt{\alpha_2} [W(\lambda_1) - W(\lambda_2)] \right] \quad (4.19)$$

where $W(\lambda_1)$ is the Wiener process. Eq. (4.18) encodes a simple cascade process. Cascade processes are simple and useful tools for describing the leading phenomenology of the intermittent information cascade in the scaling region. The structure functions are described in terms of the multiplier, $\mathcal{W}(\lambda_1, \lambda_2)$ through $S_p(r) = C_p \langle [\mathcal{W}(r/L)]^p \rangle$, where from the Langevin equation pure power law arises in the scaling region, $\langle [\mathcal{W}(r/L)]^p \rangle \sim (r/L)^{\zeta(p)}$. In this case the scaling exponents are, $\zeta(p) = \alpha_1 + p(p-1)\alpha_2/2$.

In this approximation, when the higher-order KM are small with respect to the first and the second coefficients, one can solve the corresponding Fokker–Planck equation. To solve the equation one needs to have the shape of the PDF at large scale. Assuming that the PDF have the Gaussian shape at large scale, $\lambda \rightarrow 0$, then the Fokker–Planck equation yields the change of its shape when going to small scales, $\lambda \rightarrow \infty$, and, consequently, give rise to intermittent behavior. The solution of the Fokker–Planck equation as a scalar-ordered exponential can be converted to an integral representation for the probability measure of X when $D^{(1)} \cong -\alpha_1(\lambda)X$ and $D^{(2)} \cong \alpha_2(\lambda)X^2$, i.e., when [139,12,63];

$$p(X, \lambda) = \frac{e^{\gamma_0(\lambda)}}{\sqrt{4\pi\gamma(\lambda)}} = \int_{-\infty}^{+\infty} e^{-\frac{s^2}{4\gamma(\lambda)}} \phi(Xe^{\gamma_1(\lambda)-s}) ds \quad (4.20)$$

where, $\gamma_0(\lambda) = \int_0^\lambda (-\alpha_1(\lambda') + 2\alpha_2 = (\lambda')) d\lambda'$, $\gamma_1(\lambda) = \int_0^\lambda (-\alpha_1(\lambda') + 3\alpha_2 = (\lambda')) d\lambda'$, and, $\gamma(\lambda) = \int_0^\lambda \alpha_2(\lambda') d\lambda'$. $\phi(X)$ is the probability measure in the integral length scales ($\lambda \rightarrow 0$), where one can assume its form to be Gaussian distribution [12,63].

One can consider the Gaussian distribution, $\phi(X) \cong e^{-mX^2}$ in the integral scale, which is a reasonable choice, and derive the dependence of the variance of the probability density on the scales in the limit when the original distribution satisfies the condition $m \ll 1$. The result indicates an exponential dependence, such as, $m \rightarrow me^{2\zeta}$, where $\zeta = 3\alpha_2 - \alpha_1$. The consistent picture with the shape change of the probability measure under the scale is that when λ grows, the width decreases and vice versa, which has been reported in the previous works, both in the simulation and experimental studies. Moreover, we should emphasize that the shape change is somehow complex, which gives some corrections on the order of $\mathcal{O}(m^2X^4)$, even in the simplifying limit that, $m \ll 1$.

Although Eq. (4.20) is equivalent to that for a log-normal cascade model, originally introduced to study fully developed turbulence [140–144], it also describes approximately the non-Gaussian PDFs observed in a wide range of other phenomena, such as the foreign exchange markets [145–149], heartbeat interval fluctuations [150], and seismic time series [53,54].

There is a close relation between Eq. (4.20) and the Castaing equation [140–142]. For a fixed t , the fluctuations at scales r and λr are related through the cascading rule, $X_{\lambda r}(t) = W_\lambda X_r(t)$, $\forall r, \lambda > 0$, where $\ln(W_\lambda)$ is a random variable. Iterating this equation forces implicitly the random variable W_λ to follow a log infinitely divisible law [151–153]. One of the simplest candidates for such processes is [148,154], $X_r(t) = \zeta_r(t) \exp[\omega_r(t)]$, where ζ_r and $\omega_r(t)$ are independent Gaussian variables with zero mean and variances σ_ζ^2 and σ_ω^2 . The PDF of $X_r(t)$ has fat tails that depend on the variance of ω_r , and is expressed by Castaing equation,

$$p(X, r) = \int F_r \left(\frac{X_r}{\sigma} \right) \frac{1}{\sigma} G_r(\ln \sigma) d \ln \sigma, \quad (4.21)$$

where F_r and G_r are both Gaussian with zero mean and variances σ_r^2 and λ_r^2 , respectively, e.g., $G_r(\ln \sigma) = (\sqrt{2\pi} \lambda_r)^{-1} \exp(-\ln^2 \sigma / 2\lambda_r^2)$. In this case, $p(X, r)$ is expressed by above equation and converges to a Gaussian distribution as $\lambda_r^2 \rightarrow 0$. Comparison of the Castaing equation (4.20) and Eq. (4.20) gives, $\lambda_r^2 = 2\gamma(\lambda)$, where $\lambda = \ln(L/r)$. This means that the Castaing parameter λ_r^2 is related to the diffusion coefficient $\alpha_2(\lambda)$. In Section 6 we will discuss the importance of λ_r^2 risk analysis of impending earthquakes.

Finally from the direct calculation by the Langevin equation one can easily determine the behavior of the multiscale correlation function $\mathcal{F}_{p+q}(r, R)$. In the same framework, it is straightforward to show that [63],

$$\begin{aligned} \mathcal{F}_{p+q}(r, R) &\sim \langle [\mathcal{W}(r, R)]^p [\mathcal{W}(R, L)]^q \rangle \\ &\sim \left\langle \left[\mathcal{W} \left(\frac{r}{R} \right) \right]^p \right\rangle \left\langle \left[\mathcal{W} \left(\frac{R}{L} \right) \right]^q \right\rangle \sim S_p(r) S_{p+q}(R) / S_p(R). \end{aligned} \quad (4.22)$$

The independence of the multipliers in two different scales is always assumed for the underlying cascade process. Otherwise, the above relation would not hold. Equivalently, this modeling encodes the following requirement by the obvious independency of increments in a Wiener process; see also [62].

5. Applications: processes in time and space

The method outlined in the previous section has been used for revealing nonlinear deterministic behavior in a variety of problems ranging from physics, to meteorology, biology, and medicine. In most of such cases, alternative procedures with strong emphasis on deterministic features have been only partly successful due to their inappropriate treatment of the dynamical fluctuations. The following list (with some exemplary citations) gives an overview on the investigated phenomena, which range from technical applications over many particle systems to biological and geophysical systems.

- Chatter in cutting processes [19,20]
- Identification of bifurcations toward drifting solitary structures in a gas-discharge system [155–157]
- Electric circuits [79,158,18]
- Wind energy converters [159–162]
- Traffic flow [25]
- Cosmic microwave background radiation [48]
- Inverse grading of granular flows [163]
- Heart rhythms [26,164,46,47,45,165]
- Tremor data [18]
- Meteorological data, such as data for El NINO [23,24,168]
- Seismic time series [52–54]
- Epileptic brain dynamics [50,51]
- Experimental chaotic time series and synchronization [169–171]
- Rhythmic human movement [94,95,89]
- Solar wind turbulence [172]
- Decoding the time evolution of the control parameters in a system of neurons modeled as FitzHugh–Nagumo oscillators [173]
- Porous media [174]
- Gel and glass transitions [175]
- Amorphous organic films [176]
- Electrical discharge current fluctuations in plasma [177]
- Light scattering-intensity fluctuations [178]
- Brain dynamics and synchronization [179]
- Cellular automaton model of tumor–immune interactions [180]
- Random ameboid motion [181]

- Fractal-generated turbulence [182]
- Nanocrystalline thin films [183]
- Solar granulation [184]
- Biological macromolecules [185].

See also [186,187,43,44,188–191,169,192,193] for more applications of the Markov method. The main advantage of the method of stochastic data analysis is its independence from the modeling assumptions. It is purely data driven and is based on the mathematical features of the Markov processes. As mentioned above, such properties can be verified and validated self-consistently. Before we proceed to consider some exemplary applications, we would like to add the following comment. The analysis method that we describe removes from the data dynamical and measurement noise, and provides the drift vector field, i.e., one obtains the underlying deterministic dynamical system. In turn, the system can be analyzed by the methods for the analysis of nonlinear time series: one can determine the proper embedding, the Lyapunov-exponents, the dimensions, fixed points, stable and unstable limit cycles, etc. [194]. We also point out that the determination of such quantities from noisy data is usually flawed by the presence of dynamical noise.

In this section we review the application of the Markov method to analysis of epileptic seizures, heart interbeat dynamics, financial time series, and characterization of rough surfaces.

5.1. Epileptic brain dynamics and stochastic qualifiers

As the first application of the analysis of nonlinear stochastic time series, we consider an important medical problem, namely, epileptic brain dynamics.

There has been increasing interest over the last few years in the application of nonlinear dynamics theory to modeling of brain activity. Many studies have been concerned with electroencephalographic EEG signals from intracranial or scalp recordings, in animals or human subjects, and considered in particular epilepsy, sleep, cognitive, and evoked responses (see, e.g., [195–197]). A standard approach is using the chaos theory [198–200,196] that allows a characterization of the dynamics of complex systems from the analysis of a series generated by the system, which consists of a series of measurements in time of a pertinent and easily accessible variable. The EEG signals exhibit, in general, great irregularity that may have different origins, e.g., due to noise or, otherwise, a reflection of the presence of nonlinearity and stochastic behavior. Chaos theory allows one to distinguish the irregularities in the EEG signal due to chaos from those due to noise. In the presence of chaos, the complexity of the dynamics can be quantified in terms of the properties of the attractor in the phase space, e.g., its correlation fractal dimension. The fractal dimension may, therefore, provide a classification of brain activity in terms of its complexity. However, a careful discussion is necessary in order to distinguish chaos from noise, because determining a correlation dimension is a necessary but not sufficient condition for chaos.

There are different types of epilepsy [201] with a focal or generalized nature. Epileptic seizures may occur spontaneously or may be induced by various means. Well-controlled intracranial EEG recordings were performed in rats with focal epilepsy, and the resulting data were analyzed using the chaos theory [202] in order to test the ability of the theory to detect the epileptogenic focus and the spread of the seizure activity. A decrease of the correlation dimension was observed at the seizure onset. Later, the chaos analysis was applied to intracranial EEG recordings from a group of patients with unilateral temporal lobe epilepsy [203]. Recently [204] carried out a very thorough analysis of chaos in intracranially EEG signals, during interictal and ictal states, of temporal lobe epileptic patients. They found significant evidence of the existence of a considerable degree of determinism in the system that generated the series. On the contrary, they found that signals from areas that did not exhibit seizure activity were almost indistinguishable from their randomized versions, regardless of whether they were recorded during interictal or ictal states. They then concluded that, in the particular case that they studied, the chaos analysis yields insightful results in terms of locating the epileptogenic region and following the ictal spread throughout the brain.

Despite the many promising findings, there are a number of problems for which there are currently no satisfactory solutions. This can be attributed to the fact that in many cases crucial aspects of pathological brain dynamics must be regarded as a high-dimensional stochastic process and, thus, the dynamics may not be captured if techniques for the analysis of time series are used that preferentially focus on the low-dimensional deterministic part of the dynamics.

Recently [50] used the Markovian Method to analyze the EEG time series, and showed that, such dissipative dynamical systems under the influence of noise can often be successfully modeled by a Fokker–Planck or, equivalently, the associated Langevin equation. It was shown that using this approach, an improved characterization of pathological brain dynamics can be achieved by explicitly taking into account the stochastic part of the dynamics. For this purpose they studied long-lasting, multichannel EEG time series that cover physiological and pathophysiological activities from the seizure-free interval of eight patients suffering from focal epilepsies. Despite limitations that are attributed to the fact that the EEG time series may not entirely meet the prerequisites of the underlying theoretical framework, a one-dimensional Fokker–Planck model appeared to be appropriate for the description of the physiological activities. It may not be possible, however, to capture all aspects of the pathophysiological activities in such a model. Nevertheless, they were able to derive stochastic qualifiers that allowed a more comprehensive characterization of the epileptic process. It was shown that the drift and diffusion coefficients appear to be quite useful characterizing quantities [169]. One expects that this approach, along with further improvements,

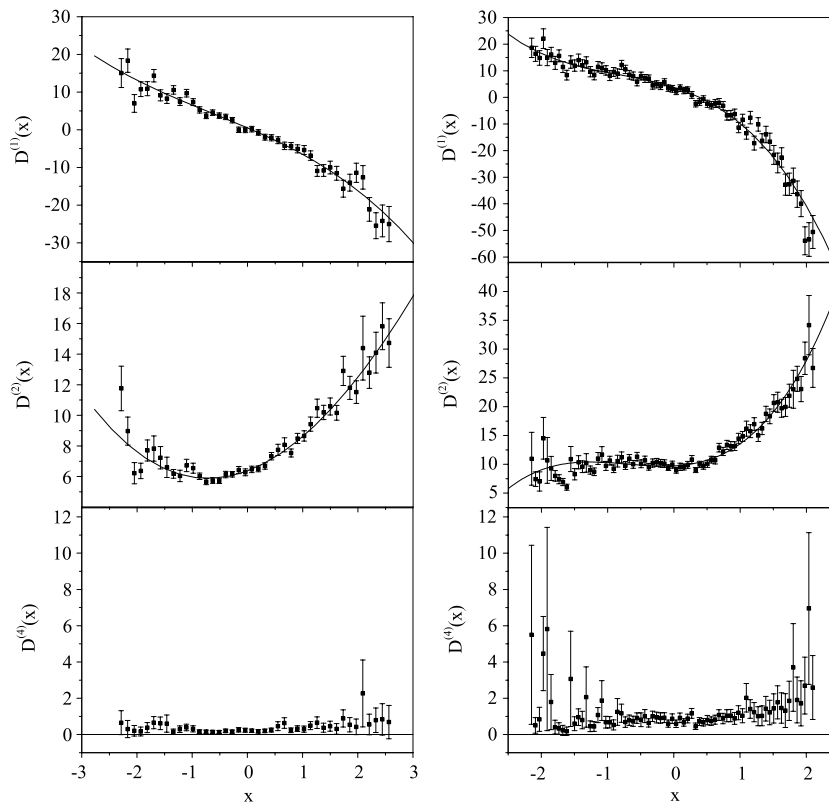


Fig. 3. Estimated coefficients $D^{(1)}$, $D^{(2)}$, and $D^{(4)}$ for exemplary EEG time series. Left: from a distant brain region; right: from within the epileptic focus. Shown are the estimates for time series consisting of 10^5 data points (squares) as well as fits with low-order polynomials (black lines). Source: From [50].

can yield valuable information for diagnostic purposes, and may even advance our understanding of the complex dynamical system that epileptic brains represent.

Prusseit et al. analyzed multichannel (20–60 recording sites), multiday (5–12 days) EEG recordings from eight patients with pharmacoresistant focal epilepsy, who had undergone evaluation for resective therapy [50]. The EEG data were recorded from the cortex and from within the relevant structures of the brain, hence with a high signal-to-noise ratio. The time series were sampled at 200 Hz using a 16 bit analog-to-digital converter, and filtered within a frequency band of 0.53 to 85 Hz. After surgery all the patients achieved complete seizure control, so that the brain structure responsible for seizure generation (epileptic focus) could be assumed to be contained within the resected brain volume. They analyzed exemplary EEG time series, recorded from within the epileptic focus and from a distant brain region during the seizure-free interval of one patient. For epoch lengths ranging from about 2–8 min, they used the Chapman–Kolmogorov equation to estimate the Markov–Einstein time scale, and showed that it is unity (in units of the sampling interval).

Fig. 3 shows typical examples of the drift and diffusion coefficients estimated from the EEG time series. Both coefficients are well approximated by low-order polynomials. As expected for this one-dimensional model, $D^{(1)}$ indicates an overall linear damping behavior. For the EEG time series recorded from within the epileptic focus, they observed small nonlinearities toward higher amplitude values, which is in line with the findings from studies that used nonlinear time series analysis techniques [205]. The behavior of $D^{(2)}$ indicates the multiplicative influence of the noise. The fourth-order coefficient $D^{(4)}$ is also shown in Fig. 3, which allows one to determine whether the driving noise process $\Gamma(t)$ exhibits deviations from a Gaussian distribution [14]. For the EEG recorded from a distant brain region, $D^{(4)}$ took on values slightly above zero, but its magnitude was less than $1/20$ of $D^{(2)}$. In contrast, for the EEG recorded from within the epileptic focus, $D^{(4)}$ took on values clearly above zero. These findings indicate that a description of the pathological brain dynamics by a one-dimensional Fokker–Planck model may be inadequate, and one needs to also take into account the effect of the higher Kramers–Moyal coefficients. This is further corroborated by the results obtained from integrating the Langevin equation using the estimated functions $D^{(1)}$ and $D^{(2)}$ for both EEG time series; see Fig. 4. While both the stationary and the conditional PDFs of the integrated model and of the EEG time series coincided quite well for the recording from a distant brain region, [50] observed more pronounced deviations for the recordings from within the epileptic focus. These findings clearly indicate that specific characteristics of the estimated drift and diffusion coefficients allow one to differentiate between physiological and pathological activities.

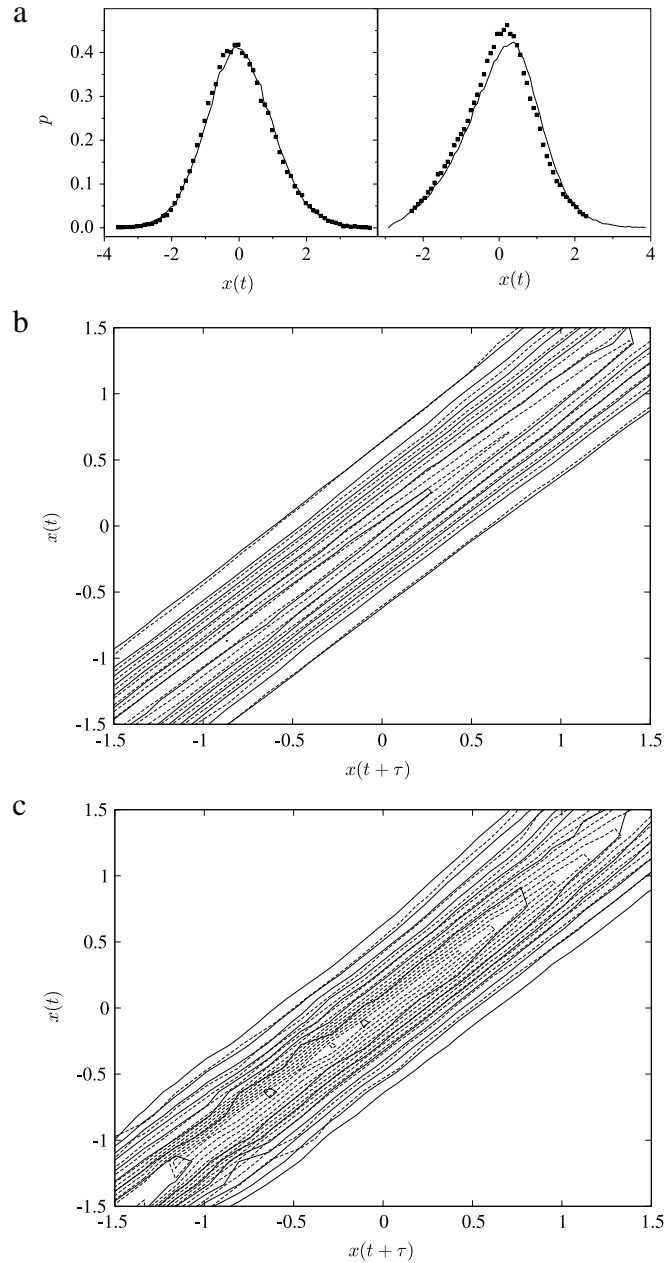


Fig. 4. Comparison of the stationary PDFs (a), and contour plots of conditional PDFs for $\tau = 1$ (b) and (c) for the EEG time series [squares in (a), dashed lines in (b) and (c)] and time series generated by integrating the associated Langevin equations (straight lines). (a) left plot and (b) from a distant brain region; (a) right plot and (c) from within the epileptic focus. Contour plots were generated using an increment between contour lines of 0.02 in (b) and 0.012 in (c).
Source: From [50].

One may define various quantities based on the estimated coefficients that serve as stochastic qualifiers of epileptic brain dynamics. As an example, consider the range covered by the values of the estimated coefficients $R_{1,2} = |\max D^{(1,2)} - \min D^{(1,2)}|$. They only took into account values of $D^{(1,2)}$ for which at least 100 data points were available for the estimation procedure. For the multichannel, multiday EEG recordings from all patients, they performed a time resolved estimation of $R_{1,2}$ using a moving-window technique. The windows were of size $N = 50,000$ points, and windows overlapped by 50%. This choice represents a compromise between sufficient statistics for a reliable estimation of $D^{(1,2)}$ and temporal resolution, which might be of interest for further EEG analysis.

Fig. 5a shows a typical spatiotemporal distribution of R_2 , calculated for a multichannel EEG (52 contacts) and recorded during the seizure-free interval, for a patient with an epileptic focus located in the right hemisphere of the brain. When

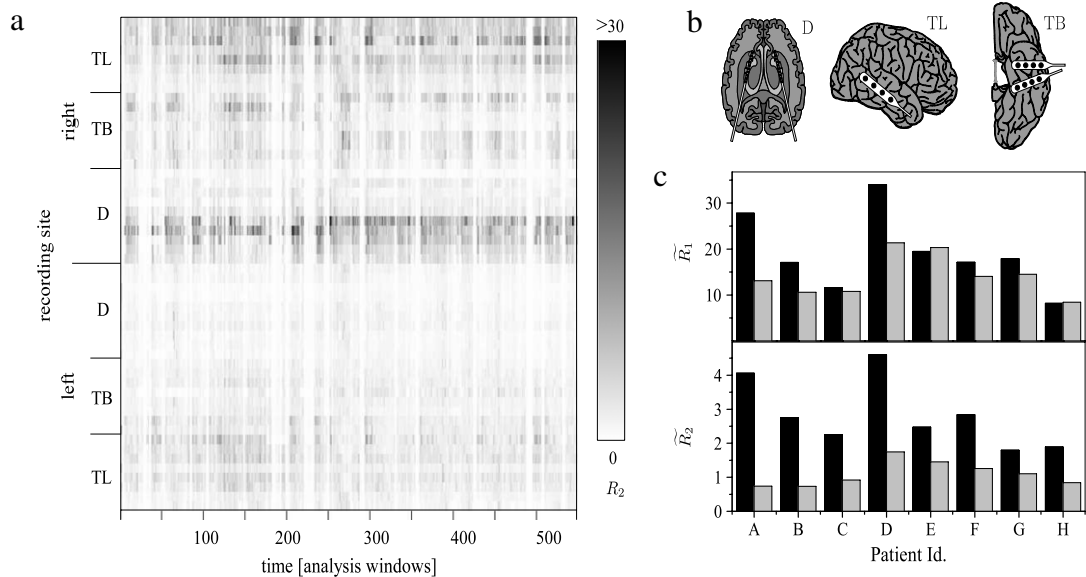


Fig. 5. (a) Time resolved estimates of R_2 calculated from a multichannel EEG recording (approximately 19 h) of a patient suffering from a right-sided focal epilepsy (patient *F*). (b) Implantation scheme of intracranial electrodes: hippocampal depth electrodes (10 contacts each, *D*), lateral (4–16 contacts, *TL*), and basal (4 contacts each, *TB*) strip electrodes. (c) Spatiotemporal means of R_1 and R_2 for all investigated patients. Black bars denote values from the focal and gray bars from the nonfocal hemisphere.

Source: From [50].

comparing findings from the left and right brain hemisphere, one observes the highest values of R_2 confined to regions close to or within the epileptic focus.

Since these values exhibit only little variance over time, for each contact, their temporal average, $(\langle R_{1,2} \rangle_t)$, was calculated and eventually averaged over all contacts c from each hemisphere ($\tilde{R}_{1,2} = \langle \langle R_{1,2} \rangle_t \rangle_c$). This allowed further condensing of the information contained in the spatiotemporal distribution of the stochastic qualifiers, and to investigate retrospectively whether they can provide diagnostically relevant information. One can refer to the brain hemisphere that contains the epileptogenic focus (determined by the presurgical workup and by the postoperative complete seizure control) as the focal side, whereas the opposite hemisphere is referred to as the nonfocal side; see Fig. 5b. In six of the eight patients \tilde{R}_1 was higher on the focal side. Interestingly, it was observed that \tilde{R}_2 allowed correct identification of the focal side in all the patients; see Fig. 5c.

5.2. Heart interbeat fluctuations

As the second example of the application of the methods described above, we consider the application of Markov method to complex heart interbeat fluctuations. Cardiac interbeat intervals fluctuate in a complex manner [206,110,207–212,26,46,47,45,165–167]. Recent studies reveal that, under normal conditions, beat-to-beat fluctuations in the heart rate may display extended correlations of the type typically exhibited by dynamical systems far from equilibrium. It was shown in [209], for example, that the various stages of sleep may be characterized by long-range correlations in the heart rates, separated by a large number of beats.

In general, interbeat fluctuations are *nonstationary* processes. In addition, they exhibit extended correlations. Thus, deducing their statistical properties by the standard methods of analyzing such processes is very difficult. One approach to analyze such processes was proposed by Stanley et al. [110,111,213,210,212,214–216] and others [217,218,206,219,220]. They studied data for heart-rate fluctuations for both healthy subjects and those with congestive heart failure (CHF), in terms of self-affine fractal distributions, such as the fractional Brownian motion (FBM). The FBM is a nonstationary stochastic process that contains long-range correlations, the successive increments of which are, however, stationary and follow a Gaussian distribution. The power spectrum of a FBM is given by, $S(f) \propto f^{-(2H+1)}$, where H is the Hurst exponent that characterizes the type of the correlations that the data contain. Thus, one may distinguish healthy subjects from those with the CHF in terms of the numerical value of H associated with the data: negative or antipersistent correlations for $H < 1/2$, as opposed to positive or persistent correlations for $H > 1/2$. The analysis of Stanley et al. indicated that there may be long-range correlations in the heart-rate fluctuations data that may be characterized by the FBM and similar fractal distributions. In addition, the data for the healthy subjects seem to be characterized by $H < 1/2$, whereas those with the CHF by $H > 1/2$. This was a significant discovery over the traditional methods of analyzing nonstationary data for heart-rate fluctuations.

However, values of the Hurst exponent H associated with the two groups of subjects are nonuniversal. Thus, it would, for example, be difficult to distinguish the two groups of subjects if their associated Hurst exponents are both close to $1/2$.

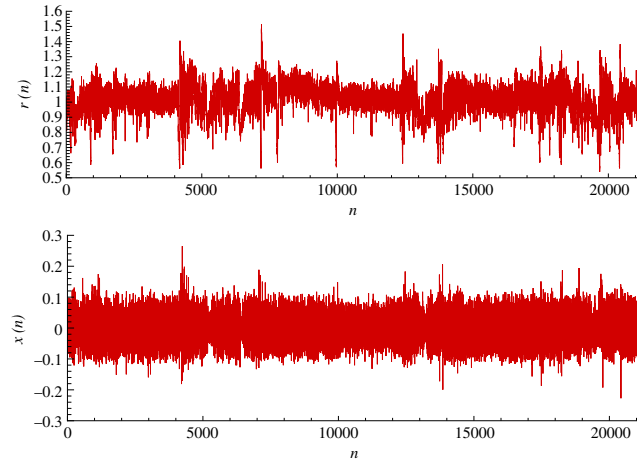


Fig. 6. Interbeats fluctuations of healthy subjects (top) and their returns (bottom).
Source: From [47].

In addition, the FBM is a *non-self-averaging* distribution, i.e., given a fixed Hurst exponent H , each realization of a FBM may be significantly different from its other realizations with the same H . As a result, estimating H alone and characterizing the data by a FBM cannot enable one to predict the *future* trends of the data. One may also analyze such data by the detrended fluctuating analysis [209–212] that, in many cases, is capable of yielding accurate and insightful information about the nature of the data.

In the next subsection, we present and describe the results of the application of the Markov method to the analysis of nonstationary interbeat data, and show that the method may potentially lead to a novel way of distinguishing healthy subjects from those with the CHF.

5.2.1. Markov analysis of nonstationary heart interbeat data

Given a (discrete) nonstationary time series r_i , i.e., the interbeat data, we introduce a quantity x_i , called the *return* of r_i , defined by [47];

$$x_i = \ln(r_{i+1}/r_i), \quad (5.1)$$

where r_i is the value of the stochastic quantity at step i . If there are long-range positive correlations in the series, then r_i and r_{i+1} are close in their values and, therefore, we expect the series x_i to have very small values for all t . For positive white noise, as well as data that exhibit negative or anti-correlations, r_i and r_{i+1} can be completely different and, therefore, the time series x_i will fluctuate strongly. Figs. 6 and 7 present the typical data for r_i and the corresponding returns x_i for healthy subjects and those with the CHF. The number of data points is of the order of 30,000–40,000, taken over a period of about 6 h. It is evident that the returns series for the subjects with the CHF has small amplitudes, implying that the r_i data set contains long-range positive correlations, which is consistent with the previous analysis [110]. It can be verified straightforwardly that the series x_i is *stationary*, by measuring the stability of its average and variance in a moving window (that is, over a period of time that varies over the length of the series).

Due to the stationarity of the series $x(t)$, we can construct an effective stochastic equation for the returns series of the two groups of the subjects, and distinguish the data for healthy subjects from those with the CHF. We apply the Markov method to the fluctuations in the human heartbeats of both healthy subjects and those with the CHF. Ghasemi et al. showed that the drift and diffusion coefficients of the data that appear in the effective stochastic continuum equations that describe the data have distinct behavior for healthy subjects and patients with the CHF, when analyzed by the Markov method, hence enabling one to distinguish the two groups of the subjects [47].

They analyzed both daytime (12:00 pm to 18:00 pm) and nighttime (12:00 am to 6:00 am) heartbeat time series of healthy subjects, and the daytime records of patients with the CHF. The data base included 10 healthy subjects (7 females and 3 males with ages between 20 and 50, and an average age of 34.3 years), and 12 subjects with the CHF (3 females and 9 males with ages between 22 and 71, and an average age of 60.8 years). Figs. 6 and 7 present the data. In Fig. 8 the spectral density of the return for healthy patients and those with the and CHF is plotted, which shows that there is no long-range order in the return signals.

Ghasemi et al. computed the Markov–Einstein time scale t_M for the returns series of the interbeat fluctuations [using the chi-square method described by Eq. (3.8), [47]. In Fig. 9 the results for the χ^2_{ν} values for a subject with the CHF are shown. For the healthy subjects the average t_M for the returns for both the day- and nighttime data, was computed to be (all the values are measured in units of the average time scale for the beat-to-beat times of each subject), $t_M = 10$. On the other hand, for the daytime records of the patients with the CHF, the estimated average t_M was, $t_M = 20$. Therefore, the data for

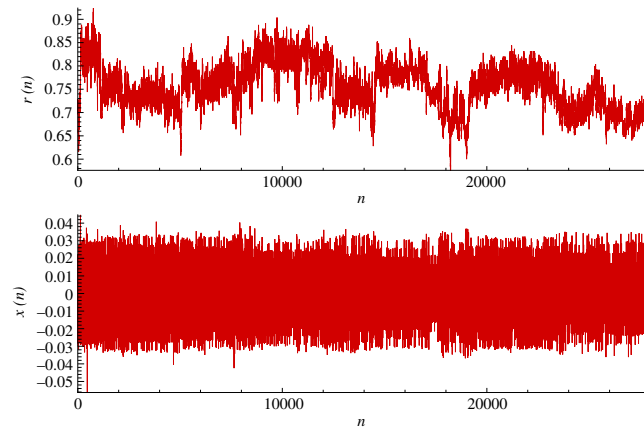


Fig. 7. Interbeats fluctuations of subjects with the CHF (top) and their returns (bottom).
Source: From [47].

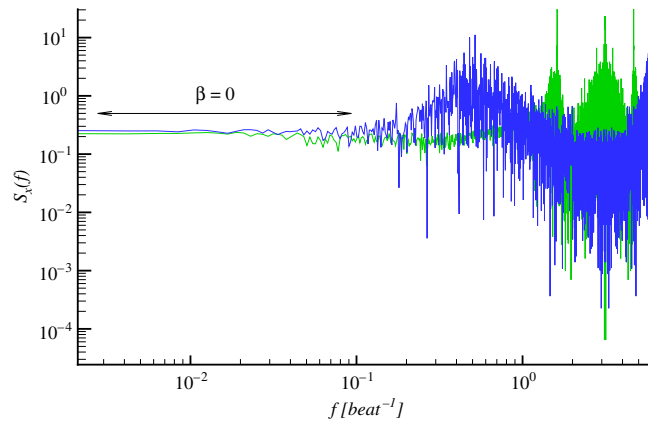


Fig. 8. Spectral density of the return data for healthy subjects (green) and those with the CHF (blue), which show that the return series do not have long-range order. (For interpretation of the references to colour in this figure legend, the reader is referred to the web version of this article.)
Source: From [47].

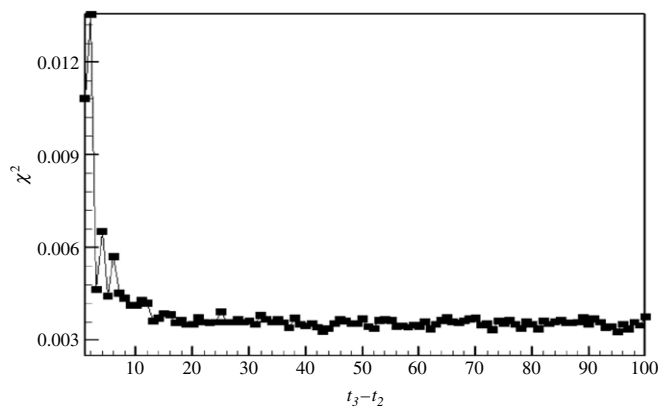


Fig. 9. χ_v^2 values for a typical subject with the CHF for several time scales.
Source: From [47].

the healthy subjects are characterized by t_M values that are smaller than those of the patients with the CHF by a significant factor of 2.

The validity of the CK equation for several x_1 was also checked for triplets by comparing the directly evaluated conditional probability distributions $p(x_3, t_3 | x_1, t_1)$ with the ones calculated according to right side of Eq. (2.26). In Fig. 10, the two

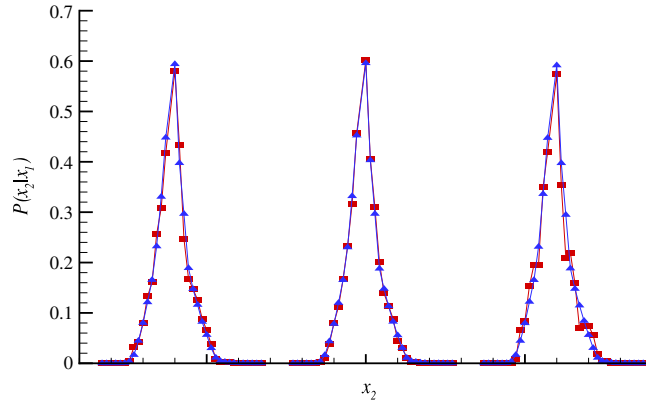


Fig. 10. Test of the Chapman–Kolmogorov equation for the time separation between t_3 and t_1 equal to the Markov time scale, for $x_1 = -6 \times 10^{-2}$, $x_1 = 0$, and $x_1 = 6 \times 10^{-2}$. Squares and triangles represent, respectively, the directly evaluated PDF and that computed PDF according to the right side of Eq. (2.26). For clarity, the PDFs are shifted in the vertical directions.
Source: From [47].

differently computed PDFs are compared. Assuming the statistical errors to be proportional to the square root of the number of events in each bin, the two PDFs are *statistically identical*.

Using Eqs. (2.40) and (2.41) directly, one can calculate the drift and diffusion coefficients, $D^{(1)}(x)$ and $D^{(2)}(x)$, for the entire set of data for the healthy subjects, as well as those with the CHF. The corresponding $D^{(1)}(x)$ and $D^{(2)}(x)$ are displayed in Fig. 11 [47]. It is found that these coefficients provide another important indicator for distinguishing the ill from the healthy subjects: the drift $D^{(1)}$ and the diffusion coefficients $D^{(2)}(x)$ follow, respectively, linear and quadratic approximants in x with distinct coefficients for the healthy subjects and patients with the CHF. The analysis of the data yielded the following estimates for the healthy subjects (averaged over the samples) [47],

$$\begin{aligned} D^{(1)}(x) &= -0.1x, \\ D^{(2)}(x) &= 3.7 \times 10^{-5} - 6.6 \times 10^{-5}x + 0.06x^2, \end{aligned} \quad (5.2)$$

with $-0.15 < x < 0.15$, whereas for the patients with the CHF the results were,

$$\begin{aligned} D^{(1)}(x) &= -0.06x, \\ D^{(2)}(x) &= 8.6 \times 10^{-6} - 2.7 \times 10^{-5}x + 0.03x^2. \end{aligned} \quad (5.3)$$

with $-0.04 < x < 0.04$. Thus, Ghasemi et al. found two important differences between the heartbeat dynamics of the two classes of subjects [47]:

- (1) Compared with the healthy subjects, the drift and diffusion coefficients for the patients with the CHF are small.
- (2) The fluctuations of the returns for healthy subjects are distinct from those with the CHF. They also fluctuate over different intervals, indicating that the returns data for the healthy subjects fluctuate over large interval. The fluctuations intervals are, $-0.04 < x < 0.04$ and $-0.15 < x < 0.15$ for patients with the CHF and healthy subjects, respectively. Hence, Ghasemi et al. suggested that one may use the magnitudes of the drift and diffusion coefficients, as well as the fluctuations intervals for the returns, for characterizing the dynamics of human heartbeats, and to distinguish healthy subjects from those with the CHF [47].

5.2.2. Comparison with other methods

Lin et al. argued that the daytime heart-rate variability of healthy subjects may exhibit *discrete* scale invariance (DSI) [221]. A stochastic process $x(t)$ possesses *continuous* scale-invariant symmetry if its distribution is preserved under a change of variables, $t \rightarrow \lambda t$ and $x \rightarrow x/\mu$, where λ and μ are *real* numbers, so that,

$$x(t) = \frac{1}{\mu}x(\lambda t). \quad (5.4)$$

If Eq. (5.4) holds only for a countable (discrete) set of values of λ , $x(t)$ is said to possess DSI, which implies a power-law behavior for $x(t)$ that has a log-periodic correction of frequency $1/\log \lambda$, so that

$$x(t) = t^\gamma F(\log t / \log \lambda), \quad (5.5)$$

with, $\gamma = \log \mu / \log \lambda$, with $F(x) = F(x + 1)$ being a period scaling function. Generally speaking, one may write, $x(t) = c(t)t^\zeta$, with, $\zeta = \gamma + 2n\pi i / \log \lambda$, with $n = 1, 2, \dots$. The existence of log-periodicity was first suggested by Novikov [222] in small-scale energy cascade of turbulent flows. It has been argued in [223,224] that log-periodicity may

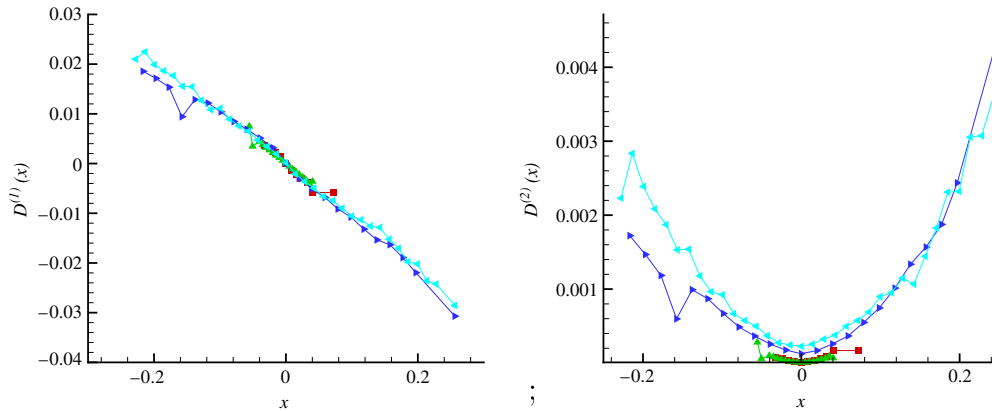


Fig. 11. The drift and diffusion coefficients, $D^{(1)}(x)$ and $D^{(2)}(x)$. For the healthy subjects (triangles) and for patients with CHF (squares), $D^{(1)}(x)$ and $D^{(2)}(x)$ follow linear and quadratic equations in x .
Source: From [47].

exist in the dynamics of stock market crashes [225], turbulence [226], earthquakes [227], diffusion in disordered material [228,229] and in fracture of materials near the macroscopic fracture point [230]. The log-periodicity implies the existence of a cascade for the multifractal spectrum of HRV, previously reported by others.

The Markovian method distinguishes the healthy subjects from those with CHF in terms of the differences between the drift and diffusion coefficients of the Fokker–Planck equations that one constructs for the returns data, which provide a clearer and more physical way of understanding the differences between the two groups of the subjects. It might eventually provide a diagnostic tool for detection of CHF in patients with small amounts of data.

5.3. Econophysics: financial data

Since Bachelier's pioneering work dating back to 1900 [231], the complex statistical properties of economic systems have attracted the attention of many researchers, and an extensive literature has evolved for modeling fluctuations of financial markets. Traditionally, fluctuations of financial assets were viewed and modeled as random variables. Well-known examples are the ARCH-type models (see, for example, [232–236] and stochastic volatility (SV) models [237–241]).

Since advances in computer technology have made high frequency data available, many physicists have joined the field, adapting methods from statistical physics in order to analyze financial data. This has given rise to the field of *econophysics*. One line of studies within econophysics focusses on the statistical properties of financial time series, such as stock prices, stock market indices, and currency exchange rates. Rather than comparing the predictions of the models with the various aspects of empirical data (which is the traditional approach), physicists try to extract information about the stochastic processes that govern financial markets by analyzing empirical data. There is already an extensive literature on the subject [242–256,234,236,257,233,258–262,188,263–275].

Despite all the efforts spent, some of the most basic questions concerning the statistics of financial assets remain unanswered. In particular, the mechanism leading to the fat-tailed (leptokurtic) probability distributions of the fluctuations on small time scales is still unknown. Compared to a Gaussian, the PDFs of such fluctuations predict an unexpectedly high probability for large fluctuations. Quantifying the risks of such large fluctuations is of utmost importance for the risk management and the pricing of options.

In the next subsections a summary of the application of the Markov method to the oil price [41] and fluctuation of currency exchange rates [42] are given.

5.3.1. Analysis of the fluctuations in the daily price of oil

Fig. 12 shows the daily fluctuations in the oil price $x(t)$ in the period 1998–2006. It is not difficult to show that the fluctuations do not constitute a stationary process by, for instance, showing that the variance of $x(t)$ in some window is not stable under increasing its size. As before, let us define the returns $y(t)$ by, $y(t) = \ln[x(t+1)/x(t)]$ [243]. The resulting series for $y(t)$ is shown in Fig. 13. It can be shown straightforwardly, by measuring the average and variance of $y(t)$ in a moving window, that $y(t)$ is stationary. Moreover, one can compute the spectral density $S(f)$ of $y(t)$ in order to check whether there are long-range, and in particular nondecaying, correlations in $y(t)$. The result, $S(f) \propto f^\beta$ with $\beta \simeq 0$, indicates the absence of such correlations in $y(t)$. In addition, the Hurst exponent was calculated by the detrended fluctuation analysis (DFA) and the rescaled-range analysis (R/S), the return can be considered as a stationary series [110]. Indeed, the Hurst exponent of the return time series is, $H = 0.51 \pm 0.2$.

The method for analyzing the fluctuations in $y(t)$ is then based on constructing a Langevin equation for $y(t)$; see also [245]. The construction of the Langevin equation is carried out in two steps. Since long-range, nondecaying correlations

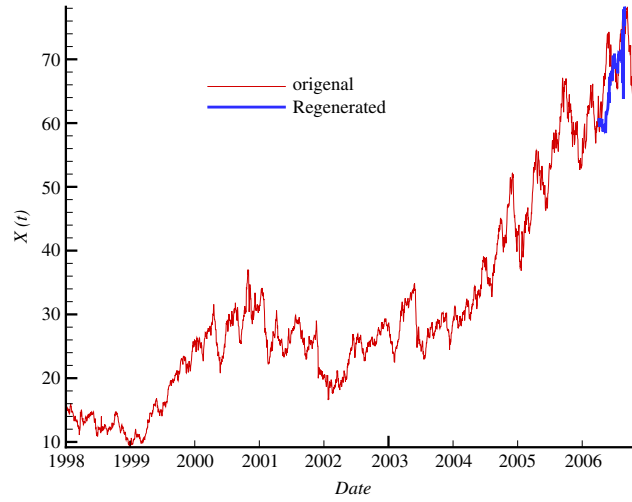


Fig. 12. Daily fluctuations in the oil price. The time lag is one day. Shown are a sample of the actual daily oil prices (red) and the reconstructed data (blue), using the Langevin equation. The inset shows the predicted range. (For interpretation of the references to colour in this figure legend, the reader is referred to the web version of this article.)

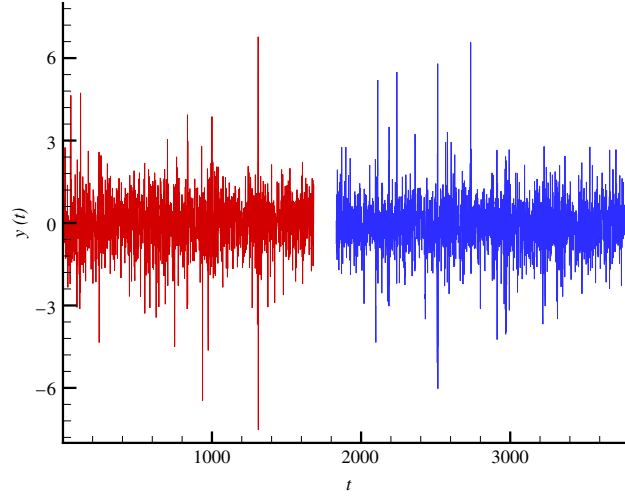


Fig. 13. Comparison of the actual return data (red) and the reconstructed ones using the corresponding Langevin equation (blue). For clarity of presentation the time series have been shifted on the t -axis. (For interpretation of the references to colour in this figure legend, the reader is referred to the web version of this article.)

Source: From [41].

are absent in $y(t)$, but short-range decaying correlations do exist, one first checks whether the time series follows a Markov chain, in which case one estimates its Markov–Einstein time scale t_M . Using the least squares method, one determines the Markov–Einstein time scale of the $y(t)$. Fig. 14 shows the normalized χ_v^2 as a function of the $t_3 - t_1$, where, $\chi_v^2 = \chi^2/N$, with N being the number of degrees of freedom. The minimum value of χ_v^2 is ≈ 0.6 , corresponding to $t_M = t_3 - t_1 \approx 1$ day. Fig. 15 shows the likelihood function of the Markov–Einstein time scale of the $y(t)$. Using the method proposed in Section 2, one estimates the Markov–Einstein time scale via a direct check of the CK equation. The result is again $t_M \approx 1$ day.

For the data for oil price fluctuations, one finds that, $D^{(4)} \approx 10^{-2}D^{(2)}$, where values of $y(t)$ are measured in units of the maximum of the time series, y_{\max} . This allows the truncation of the KM expansion. In that case, the KM expansion reduces to a Fokker–Planck (FP) equation [i.e., Eq. (4.9) with $D^{(k)}(y, t) = 0$ for $k \geq 3$]. It also turns out that the resulting drift and diffusion coefficients, estimated directly from the data, are, respectively, linear and quadratic functions of y , and are well represented by the approximates,

$$D^{(1)}(y) = -1.09y,$$

$$D^{(2)}(y) = 0.0033 - 0.003y + 0.716y^2.$$

(5.6)

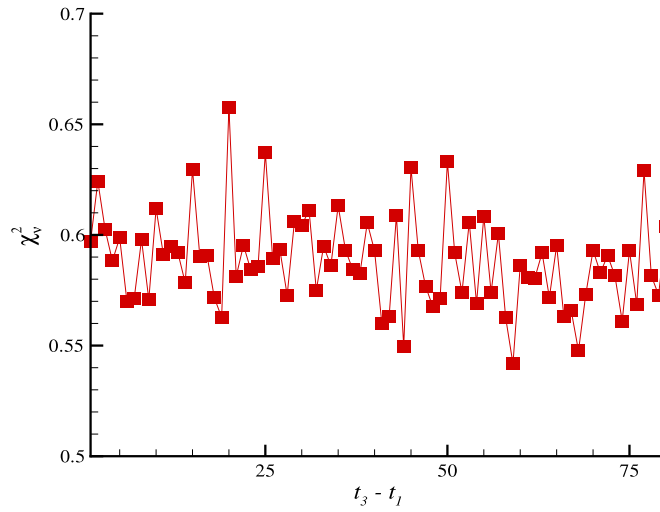


Fig. 14. The χ^2 test for estimation of Markov time scale of the time series of the returns, indicating that the Markov time scale t_M is 1 day. Source: From [41].

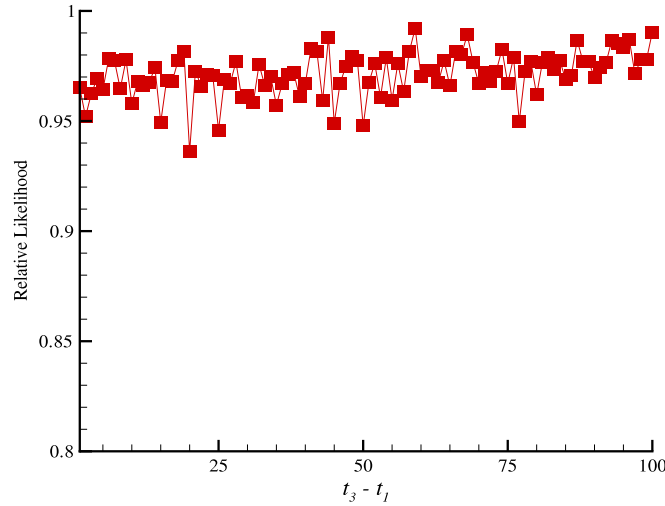


Fig. 15. Relative likelihood function for the Markov–Einstein time scale of the $y(t)$ fluctuations, as a function of $t_3 - t_1$. Source: From [41].

Estimates of $D^{(1)}(y)$ and $D^{(2)}(y)$ become poor for large y and, thus, the uncertainty in the estimates increases. Eq. (5.6) enables us to reconstruct a time series for $y(t)$ which is similar to the original one *in the statistical sense*. In Fig. 13 the original and reconstructed time series for $y(t)$ are shown.

Next, one evaluates the precision of the reconstructed $y(t)$. This is done by reconstructing the conditional PDF through the numerical solution of the FP equation for the conditional PDF, which is very sensitive to the errors in $D^{(1)}$ and $D^{(2)}$. The solution of the FP equation for small Δt is given by,

$$p(y_2, t + \Delta t | y_1, t) = \frac{1}{2\sqrt{\pi D^{(2)}(y_2)\Delta t}} \exp\left[\frac{-(y_2 - y_1 - D^{(1)}(y_2)\Delta t)^2}{4D^{(2)}(y_2)\Delta t}\right]. \quad (5.7)$$

Eq. (5.7) enables one to predict the probability of an “observation” y_2 at time $t + \Delta t$, if one knows y_1 at time t . In Fig. 16 we show the computed conditional PDFs using the data, and those using Eq. (5.7), for three values of y_1 with $\Delta t = 1$. To do more checking, we used the Kolmogorov–Smirnov test [276,279] to compare the cumulative distribution function for the original and reconstructed time series. With 1682 data points one finds the maximum difference between the two cumulative PDFs to be about 0.030. For α –levels of %10, %5 and %1, one finds the critical values to be, 0.042, 0.046 and 0.056, respectively [41].

To make predictions, one uses the definition of $y(t)$ to write $x(t + 1)$ in terms of $x(t)$. But, since the reconstructed data have unit variance and zero mean, we have

$$x(t + 1) = x(t) \exp\{\sigma_y[y(t) + \bar{y}]\}, \quad (5.8)$$

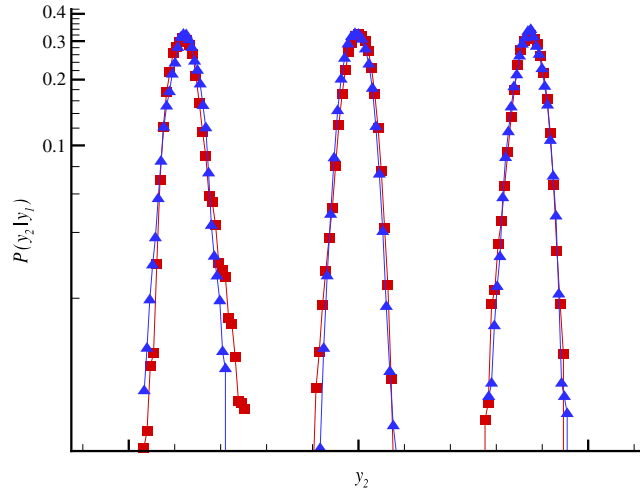


Fig. 16. Comparison of the directly evaluated PDFs using the actual data, and the PDFs obtained from Eq. (2.24). Values for y_1 , from left to right, are -0.1 , 0.0 , and 0.1 [measured in units of $y_{\max}(t)$]. For better presentation, the PDFs have been shifted on the horizontal axis. Source: From [41].

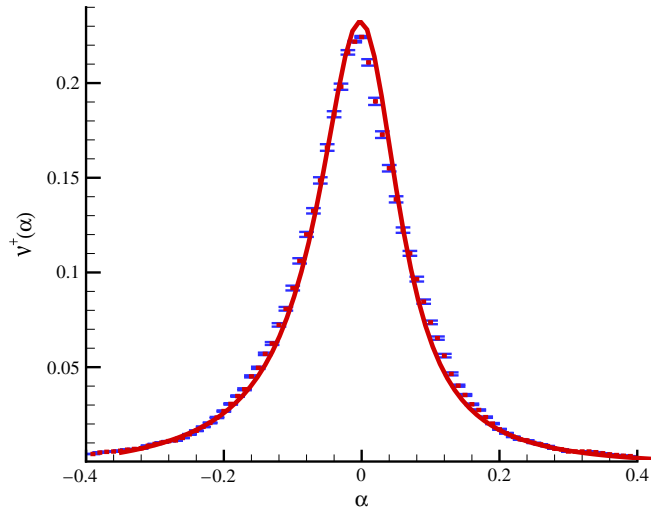


Fig. 17. The level crossing $v^+\alpha$ for the returns time series. Source: From [41].

where \bar{y} and σ_y are the mean and standard deviations of $y(t)$. To use Eq. (5.8) to predict $x(t + 1)$, one needs $[x(t), y(t)]$. It is possible to select three consecutive points in the series $y(t)$ and search for three consecutive points in the reconstructed series of $y(t)$ that have the smallest difference with the selected points. Shown in Fig. 12 are the actual data and the predictions for some interval in the oil price $x(t)$, beginning with $t \simeq 2006$ (blue). Moreover, it is possible to predict the time series using the multiscale reconstruction of time series [100,101] or mapping the time series to a complex network [103].

Finally, using the calculated drift and diffusion coefficients, one computes the frequency of the level crossings at a given level α (see Section 6). This quantity is given by, $v_\alpha^+ = P(y_i > \alpha, y_{i-1} < \alpha)$, where v_α^+ is the number of positive-difference crossings of $y(t)$, $y(t) - \bar{y} = \alpha$, in the interval T . The time scale $T(\alpha) = 1/v_\alpha^+$ is then the average time interval that one should wait in order to observe the given $y = \alpha$ again. The frequency v_α^+ is given by Eq. (3.26) with $\Delta t = 1$. Figs. 17 and 18 represent the computed level-crossing frequency and $T(\alpha)$, in units of the data (days) over a time interval, for both the actual data set and the one reconstructed by Eq. (5.6). The Maximum and minimum of y are 0.4 and -0.4 , respectively.

5.3.2. Fluctuations in the currency exchange rates

In this subsection we give a summary of the results of the application of the Markov method to analyzing the data for the rates of exchange of various currencies versus the US dollar. The method analyzes the return time series of the data as a Markov process, and develops an effective equation which reconstructs the data. It is found that the Markov–Einstein time scale is one day for the majority of the daily exchange rates.

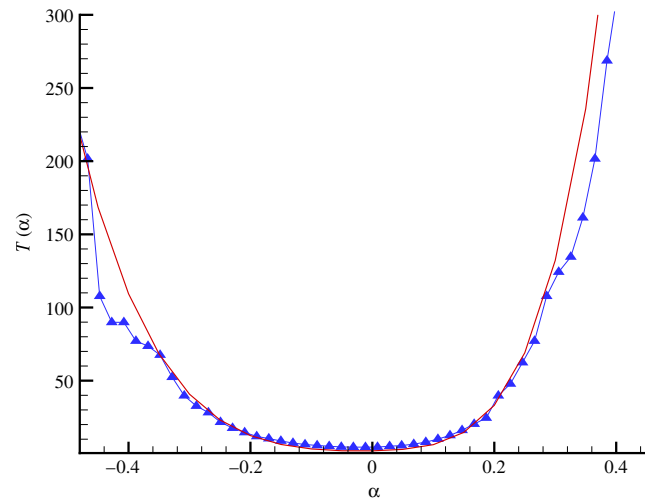


Fig. 18. The average waiting time for observing $y(t) = \alpha$ again.
Source: From [41].

Table 1

The Markov–Einstein time scale t_M , and the drift and diffusion coefficients for the various exchange rates versus the US dollar. The results are, from top to bottom, for French, German (Mark), Dutch, Swiss, Japanese, Austrian, British, and Canadian currencies [42].

Currency	t_M	$D^{(1)}$	$D^{(2)}$
FRNFR/US	1	$-1.0328r$	$0.0081 + 0.0096r + 0.4133r^2$
GERDM/US	1	$-0.0082 - 0.9474r$	$0.0078 + 0.0110r + 0.5942r^2$
DTCHG/US	1	$-0.0033 - 1.0071r$	$0.0043 - 0.0007r + 0.7134r^2$
SWISF/US	1	$-0.0051 - 1.0142r$	$0.0067 + 0.0087r + 0.4736r^2$
JAPYN/US	1	$-0.0033 - 1.0571r$	$0.0029 - 0.0088r + 0.6716r^2$
AUSTR/US	1	$-0.0014 - 1.1629r$	$0.0080 + 0.0126r + 0.6385r^2$
BRITP/US	1	$-0.0013 - 0.9439r$	$0.0053 + 0.0117r + 0.5853r^2$
CDNDL/US	1	$-0.0008 - 1.0460r$	$0.0039 + 0.0091r + 0.7006r^2$
EURO/US(hourly)	1	$-0.04242 - 0.0287r$	$0.00069 + 0.00123r + 0.00045r^2$

Let us start with applying the method to construct the fluctuations in the rates of exchange of various currencies versus the US dollar, by calculating the Markov–Einstein time scale t_M [42]. For this purpose, one first, as usual, constructs the return series r_i . Then, to determine t_M , the validity of the CK equation for various r_1 is checked by comparing the directly evaluated conditional probability distributions $p(r_2, t_2 | r_1, t_1)$ with those calculated according to right side of Eq. (2.26). The data were taken from the source, (<http://finance.yahoo.com/>), and are all related to the same time period, namely, 31 December, 1979 to 31 December, 1998. Except for the hourly price of the EURO over a period of 4 months (30 January to 31 May, 2003), the rest had been recorded for each trading day. In Table 1, the Markov–Einstein time scale t_M for different currencies versus the US dollar are given. Since the price index returns can be represented by a Markov process, we can derive an effective stochastic equation that describes the fluctuations of the returns r_n . From the analysis of the data set one obtains the approximates that are presented in Table 1. To estimate the drift and diffusion coefficients, they are measured in units of the σ , where σ is the standard deviation of r ; see Figs. 19 and 20 [42].

To make predictions for the future trends, one can use the definition of $r(t)$ to write $x(t + 1)$ in terms of $x(t)$. But, since the reconstructed data have a variance equal to 1 and a zero mean, we have, $x(t + 1) = x(t) \exp\{\sigma_r[r(t) + \bar{r}]\}$ where \bar{r} and σ_r are the mean and standard deviations of $r(t)$. To use this equation for predicting $r(t + 1)$, we need $[x(t), r(t)]$. We select again three consecutive points in the series $r(t)$ and search for three consecutive points in the reconstructed series of $r(t)$ that have the smallest difference with the selected points. Shown in Fig. 21 are the actual data and the predictions for some interval in the time series for the hourly rates of EURO versus the US dollar.

5.4. Rough surfaces

So far, we considered stochastic data that vary in time. We now consider those that vary in space.

5.4.1. Reconstruction of rough surfaces

Studying the formation, growth, and the morphology of interfaces has been a recent research field of much interest, because of its high technical importance and rich theoretical value [137,280]. The Markov method is applicable to

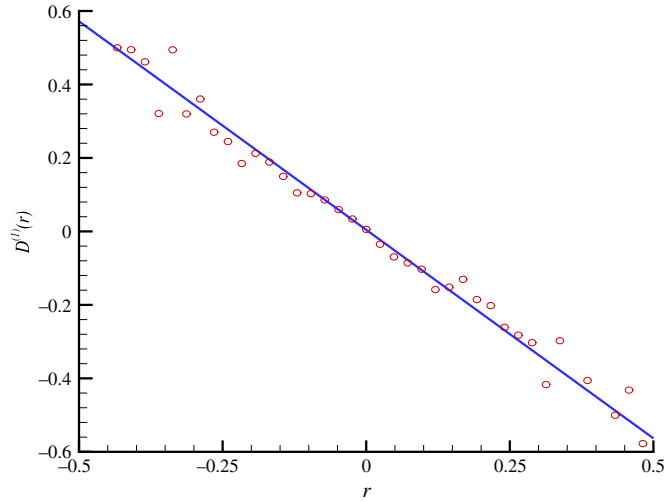


Fig. 19. The drift coefficient for the EURO versus the US dollar.
Source: From [42].

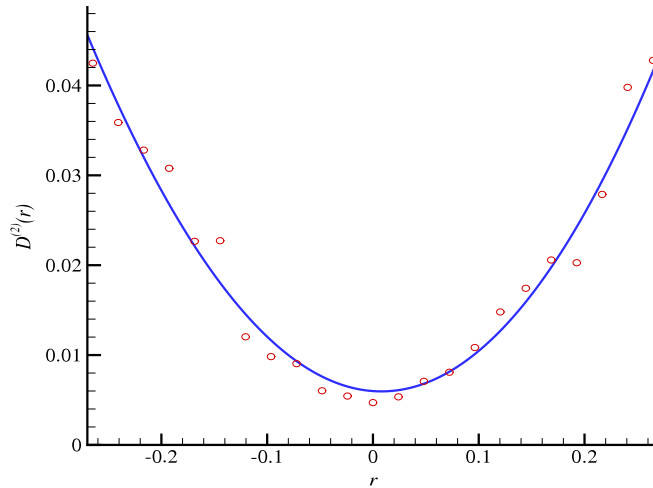


Fig. 20. The diffusion coefficient for the EURO versus the US dollar.
Source: From [42].

the analysis of such surfaces and interfaces. As an example, we summarize in this section the measurement of the Kramers–Moyal (KM) coefficients for the fluctuating field $h(x)$, the height of a deposited copper film [30]. It is shown that the first and second KM coefficients have nonzero values, while the third- and fourth-order coefficients in the KM expansion tend to zero. Thus, the first and second KM coefficients for the fluctuations of $h(x)$ enable us to write down a Langevin equation for the evolution of the height $h(x)$ with respect to x . Using this equation one reconstructs the surface with statistical properties similar to the original one, obtained by atomic force microscopy (AFM). An application of this stochastic description of rough surfaces to a variety of different surfaces, like road surfaces, steel crack surfaces or gold films, can be found in [31].

The reconstruction of a surface is known as the inverse method. There are other inverse approaches introduced in the literature [281,282]. In the previous attempts, in order to regenerate the surface, an evolution equation for $h(x, t)$ vs t was evaluated. The Markov method enables one to develop an evolution equation for $h(x)$ vs. x , for a given time.

A copper film was deposited on a polished Si (100) substrate by the resistive evaporation method in a high vacuum chamber. The pressure during evaporation was 10^{-6} Torr (see [30], for details of the experiment). The resulting surface was then analyzed using the AFM.

It is a common procedure to characterize the complexity of a rough surface by checking the scaling behavior of the moments $C_q = \langle |h(x_1) - h(x_2)|^q \rangle$ in terms of the length scale $\Delta x = |x_1 - x_2|$. Jafari et al. investigated the scaling behavior of the q -th moment C_q and observed that all of the moments (up to $q = 20$) behave as $|\Delta x|^{q\xi_q}$ within the scaling region ~ 10 to 150 nm [30]. They found a nonlinear relation between ξ_q and q , indicating that the height fluctuations are intermittent

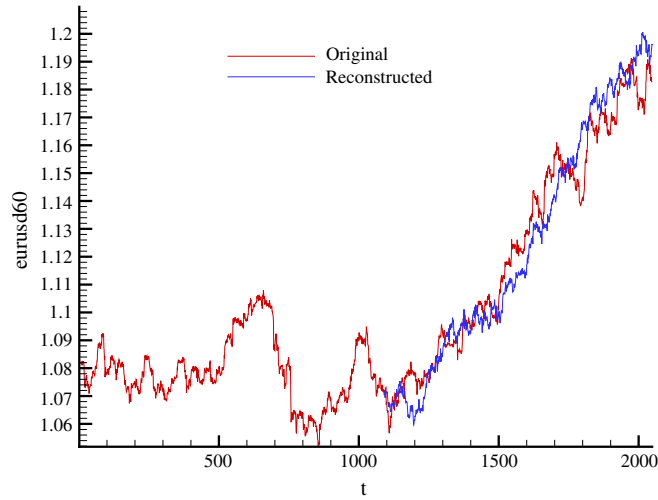


Fig. 21. Comparison of the actual and reconstructed hourly data for the EURO.
Source: From [42].

or multifractal (see [283,284] and references therein). The roughness exponent α is related to the exponent ξ_2 as $\alpha = \xi_2/2$. For the stationary samples with thickness 440 nm, the roughness exponent α was found to be 0.83 ± 0.03 .

From the stochastic point of view, one must recall that the multifractality is based on properties of the roughness on distinct length scales. However, checking the scaling behavior does not explain a possible correlation between the roughness measures on different scales. Moreover, it is noted that the methods based on multifractality are limited to the subclass of rough surfaces that exhibit scaling properties. The Markov method, on the other hand, is a general method that can explain the complexity of the surface roughness, with no scaling feature to be explicitly required. The method yields an effective stochastic equation in the form of a Fokker–Planck equation. The connection between the multifractality and the Markov approach was discussed by Friedrich and Peinke [10].

As usual, one checks the Markov nature of the fluctuations in the height, $h = h(x) - \bar{h}$ of the Cu film surface. One then finds the following expression for $D^{(1)}(h)$ and $D^{(2)}(h)$:

$$\begin{aligned} D^{(1)}(h) &= -0.01h \\ D^{(2)}(h) &= 0.088 - 0.004h + 5.19 \times 10^{-5}h^2. \end{aligned} \quad (5.9)$$

The height field is measured in units of the standard deviation of $h(x)$. Thus, we write a Fokker–Planck equation for the PDF of $h(x)$. As usual, the Fokker–Planck equation is equivalent to the following Langevin equation (using the Ito interpretation):

$$\frac{d}{dx}h(x) = D^{(1)}(h) + \sqrt{D^{(2)}(h)}f(x). \quad (5.10)$$

Here, $f(x)$ is a random force with zero mean and Gaussian statistics, δ -correlated in x , i.e., $\langle f(x)f(x') \rangle = 2\delta(x - x')$. Furthermore, with the last expression, it becomes clear that the method is able to separate the deterministic and the noisy components of the surface height fluctuations in terms of the coefficients $D^{(1)}$ and $D^{(2)}$. Eq. (5.10) enables us to reconstruct rough surfaces that are similar to the original one (in the statistical sense). In Fig. 22 the AFM and reconstructed images are shown. The reconstructed surface is very similar, in a statistical sense, to the original one. All reconstructed patterns are statistically similar. To demonstrate this fact we show, for example, in Fig. 23 a plot of the second moment of the structure function C_2 for the AFM and a reconstructed surfaces. Their roughness exponents were found to be, 0.83 ± 0.03 and 0.83 ± 0.01 , respectively (see [30], for more details).

5.4.2. Controlling surface statistical properties using bias voltage

As an another example we consider the effect of voltage bias on the statistical properties of rough surfaces, and investigate its stochastic nature via the Markov method. In practice, an effective way of modifying the roughness of the surfaces is applying a negative voltage bias during deposition of thin films [285], while their sample size and thickness are held constant. In bias sputtering, the electric fields near the substrate are modified to vary the flux and energy of the incident charged species. This is achieved by applying either a negative DC or RF bias to the substrate. Due to charge exchange processes in the anode dark space, very few discharge ions strike the substrate with full voltage bias. A rather broad low energy distribution of ions bombard the growing films. Generally, bias sputtering modifies the films' properties, such as the surface morphology, resistivity, stress, density, adhesion, and so on through the roughness improvement of the surface, elimination of the interfacial voids and the subsurface porosity, creation of a finer and more isotropic grain morphology,

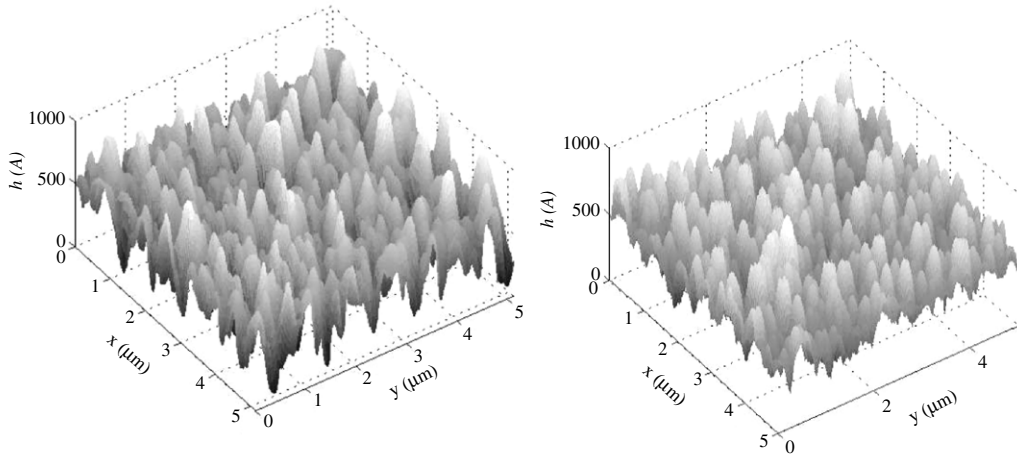


Fig. 22. The AFM and regenerated surface images (from up to bottom), which we have regenerated the rough surface using the Langevin equation for dynamics of $h(x)$. As drift term $D^{(1)}(h) = -0.01h$ and as diffusion term $D^{(2)}(h) = 0.088 - 0.004h + 5.19 \times 10^{-5}h^2$. Source: From [30].

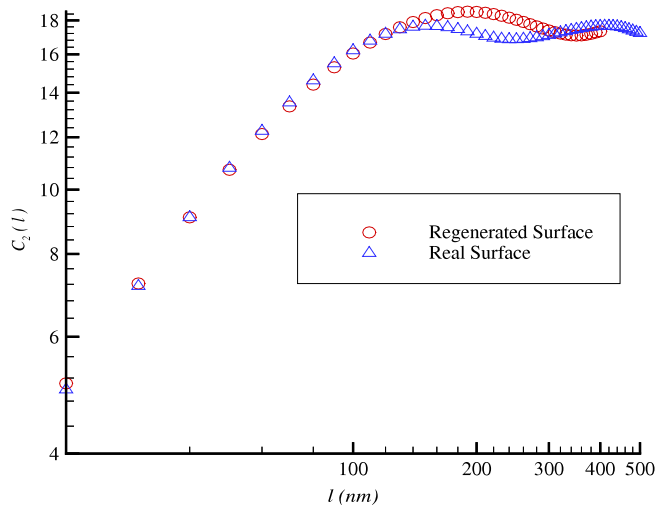


Fig. 23. Log–log plot of the second moment of height difference vs. l for real sample and regenerated sample. The roughness exponents for real and regenerated are 0.83 ± 0.03 and 0.83 ± 0.01 , respectively. Source: From [30].

and the elimination of columnar grains [285]. Here, the effect of voltage bias on the statistical properties of a surface, i.e., its roughness exponent, the level crossing, the probability density function, as well as the drift and diffusion coefficients, has been studied [35].

It is known that to derive a quantitative information of a surface morphology one may consider a sample of size L and define the mean height of a growing film, \bar{h} , and its roughness w by the following expressions [286,287]: $\bar{h}(L, t, \lambda) = L^{-1} \int_{-L/2}^{L/2} h(x, t, \lambda) dx$, and, $w(L, t, \lambda) = [(\langle h^2 \rangle - \bar{h}^2)]^{1/2}$, where t is proportional to the deposition time, and $\langle \dots \rangle$ denotes an averaging over different samples. Moreover, one can introduce λ as an external factor that can be applied in order to control the surface roughness of thin films. We introduce a parameter, $\lambda \equiv V/V_{\text{opt}}$, where V and V_{opt} are the applied and the optimal voltage biases, so that for $\lambda = 1$ the surface exhibits its optimal properties. For simplicity, one can assume that $\bar{h} = 0$, without loss of generality. Starting from a flat interface (one of the possible initial conditions), one conjectures that a scaling of space by a factor b and of the time by a factor b^z (z is the dynamical scaling exponent) rescales the roughness w by a factor b^x , so that, $w(bL, b^z t, \lambda) = b^{x(\lambda)} w(L, t, \lambda)$, which implies that, $w(L, t, \lambda) = L^{x(\lambda)} f(t/L^z, \lambda)$. If for large t and fixed $L(t/L^z \rightarrow \infty)$, w saturates and, $f(x, \lambda) \rightarrow g(\lambda)$, as $x \rightarrow \infty$. However, for fixed and large L and $t \ll L^z$, one expects that correlations of the height fluctuations are set up only within a distance $t^{1/z}$ and, thus, must be independent of L . This implies that for $x \ll 1$, $f(x) \sim x^\beta g'(\lambda)$, with, $\beta = x/z$. Thus, dynamic scaling postulates that

$$w(L, t, \lambda) = \begin{cases} t^{\beta(\lambda)} g(\lambda) \sim t^{\beta(\lambda)}, & t \ll L^z =; \\ L^{x(\lambda)} g'(\lambda) \sim L^{x(\lambda)}, & t \gg L^z. \end{cases} \quad (5.11)$$

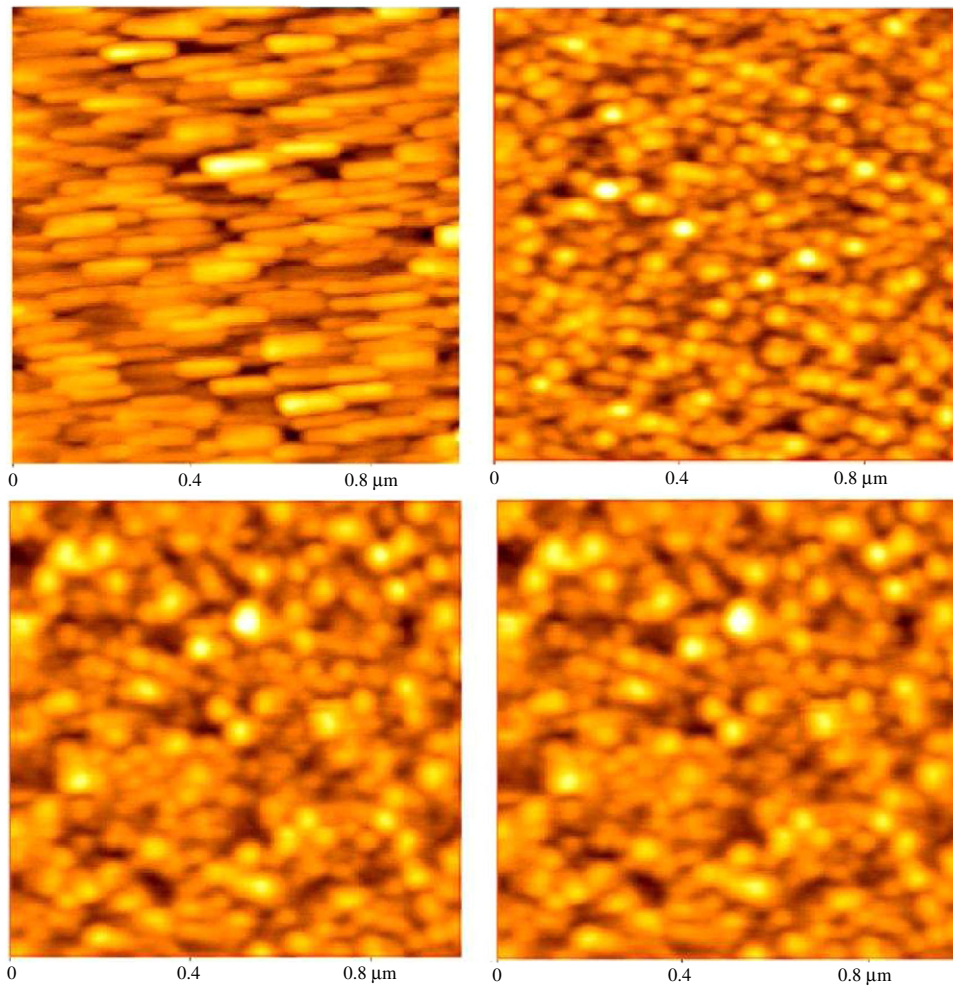


Fig. 24. AFM surface images (all $1 \times 1 \mu\text{m}^2$) of Co (3 nm)/NiO (30 nm)/Si (100) thin films deposited at the voltage biases of, from the top, (a) 0; (b) -20 ; (c) -40 , and (d) -60 V.

Source: From [35].

The roughness exponent χ and the dynamic exponent z characterize the self-affine geometry of the surface and its dynamics, respectively. The dependence of the roughness w on the \bar{h} or t indicates that w has a fixed value for a given time.

The common procedure to measure the roughness exponent of a rough surface is based on the use of a surface structure function that depends on the length scale $\Delta x = r$, which is defined by, $S(r) = \langle |h(x+r) - h(x)|^2 \rangle$ [288,289]. It is equivalent to the statistics of the height–height correlation function $C(r)$ for stationary surfaces, i.e., $S(r) = 2w^2(1 - C(r))$. The second-order structure function $S(r)$ scales with r as, $S(r) \sim r^{\xi_2}$, where $\chi = \xi_2/2$.

Sangpour et al. analyzed the surface of Co (3 nm)/NiO (30 nm)/Si (100) structure [as a base structure in the magnetic multilayers, e.g., spin valves operated using giant magnetoresistance (GMR) effect [290,291], fabricated by bias sputtering method at different voltage biases [35]. The behavior of the statistical characterizations obtained by the nanostructural analysis has been also compared with that of the sheet resistance measurement of the films deposited at the different voltage biases. The details of the experiments are given by [35]. To study the effect of the voltage bias on the surface statistical characteristics, Sangpour et al. utilized the AFM method for obtaining microstructural data from the Co layer deposited at the various voltage biases in the Co/NiO/Si (100) system. Fig. 24 shows the AFM micrographs of the Co layer deposited at various negative voltage biases of -20 , -40 , -60 , and -80 V, as compared with the unbiased samples [35].

Fig. 24a presents, for the unbiased very thin Co layer, a columnar structure of the Co grains, grown over the evaporated NiO underlying surface. Fig. 24b shows, however, that by applying the negative voltage bias during the Co deposition, the columnar growth is eliminated. Moreover, Fig. 24c and d show that, by increasing the voltage bias up to -60 V, the grain size of the Co layer is increased which means a more uniform and smoother surface is formed. But, for the voltage bias of -80 V, due to the initiation of resputtering of the Co surface by the high energy ion bombardment, one obtains a nonuniform surface, even at the macroscale. Therefore, based on the AFM micrographs, the optimum surface morphology of the Co/NiO/Si (100) system was achieved at the voltage bias of -60 V for the experimental conditions.

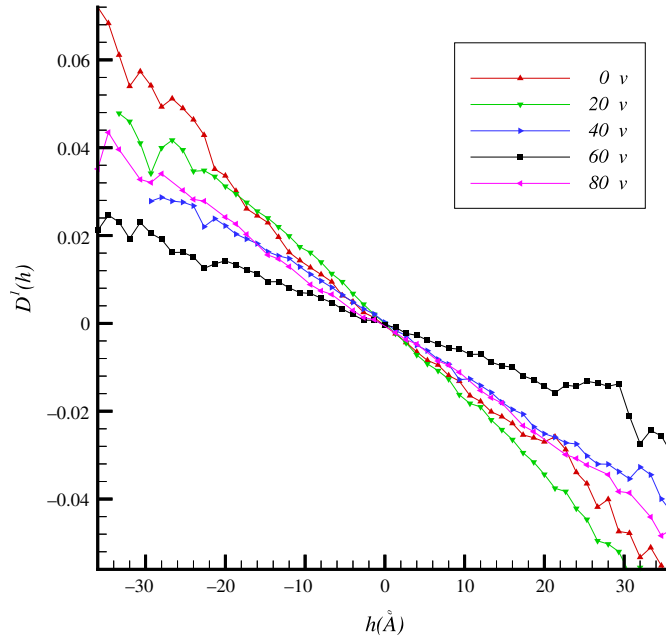


Fig. 25. Drift coefficient of the surface at various voltage biases.
Source: From [35].

Now, by using the statistical parameters introduced in Sections 2–6, it is possible to obtain some quantitative information about the effect of the voltage bias on the surface topography of the Co/NiO/Si (100) system. It has been shown that the surface grown at the optimal voltage bias (−60 V) exhibits a minimum roughness with $\chi \simeq 0.60$, which should be compared with what is obtained with the other biased samples, $\chi \simeq 0.75, 0.70$, and 0.64 for $V = -20, -40$, and -80 V, respectively [35]. For the unbiased sample, one finds two roughness exponents, 0.73 and 0.36 , due to the nonisotropic structure of the surface (see Fig. 24a).

For the unbiased sample, it is shown that it has two correlation lengths of 30 and 120 nm, due to the columnar structure of the grains. However, by applying the voltage bias, one attributes just one correlation length to each curve, indicating the elimination of the columnar structure in the biased samples. For the voltage bias of -20 V, the correlation length r^* is determined to be 56 nm. By increasing the value of the bias voltage to -40 and -60 V, it was shown that $r^* = 76$ and 95 nm, respectively [35]. However, at -80 V, due to the initiation of the destructive effects of the high energy ions on the surface, the correlation length is reduced to 76 nm. Thus, based on the above analysis, if one assumes that $V_{\text{opt}} = -60$ V, then, the roughness exponent and the correlation length may be expressed in terms of the parameter λ as follows, respectively,

$$\chi(\lambda) = 0.61 + 0.16 \sin^2(2\pi\lambda/3.31 + 1.07) \quad (5.12)$$

$$r^*(\lambda) = 53.50 + 40.23 \sin^2(2\pi\lambda/3.00 + 2.62) \text{ (nm)}. \quad (5.13)$$

To obtain the stochastic continuum equation for describing the surface, one needs, as usual, to measure the drift coefficient $D^{(1)}(h)$ and diffusion coefficient $D^{(2)}(h)$. Fig. 25 shows $D^{(1)}(h)$ for the surfaces at the various voltage biases. It can be seen that the drift coefficient exhibits a linear behavior with h :

$$D^{(1)}(h, \lambda) = -f^{(1)}(\lambda)h \quad (5.14)$$

where

$$f^{(1)}(\lambda) = [0.55 + 1.30 \sin^2(2\pi\lambda/3.50 + 1.40)] \times 10^{-4}. \quad (5.15)$$

The minimum value of $f^{(1)}(\lambda)$ for the biased samples at $\lambda = 1$ indicates that the deterministic component of the height fluctuations for the samples is smaller than the other biased and unbiased ones.

Fig. 26 presents $D^{(2)}(h)$ for the several voltage biases. For $\lambda = 0$, the maximum value of the diffusion coefficient is obtained for any h , as compared with the other cases. By increasing the voltage bias, the value of $D^{(2)}$ is decreased, as can be seen for $\lambda = 1/3$ and $2/3$. The minimum value of $D^{(2)}$, which is nearly independent of h , is achieved when $\lambda = 1$. This indicates that the noisy component of the surface height fluctuation at $\lambda = 1$ is negligible, when compared with the unbiased and the other biased samples. The behavior of $D^{(2)}$ at $\lambda = 4/3$ becomes similar to that for $\lambda = 2/3$. It is seen that the diffusion coefficient $D^{(2)}$ is approximately a quadratic function of h . Using the data analysis, it was found that [35];

$$D^{(2)}(h, \lambda) = f^{(2)}(\lambda)h^2 \quad (5.16)$$

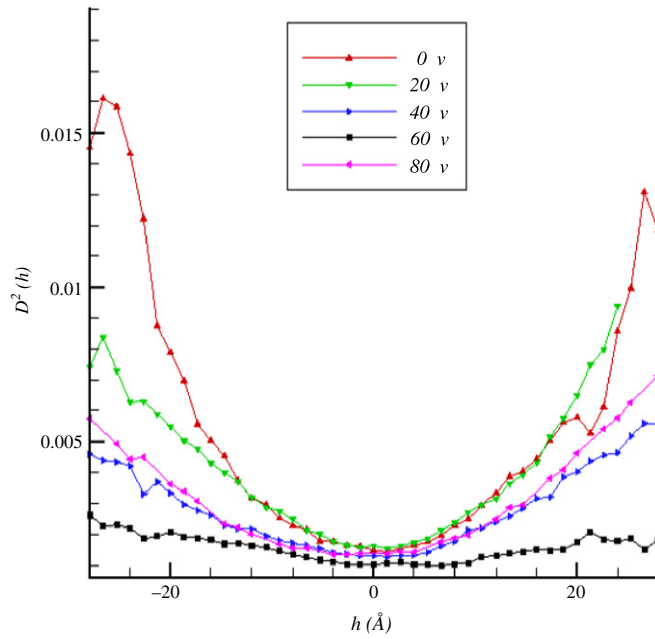


Fig. 26. Diffusion coefficient of the surface at different voltage biases.
Source: From [35].

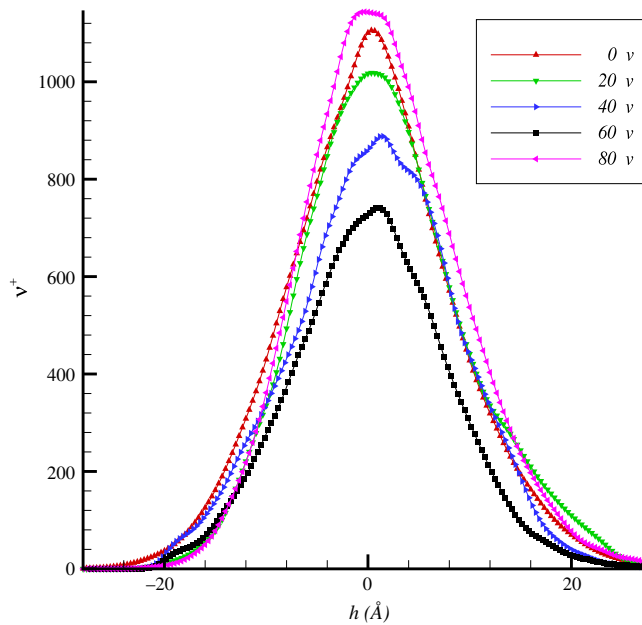


Fig. 27. Level crossing of the surface at various voltage biases.
Source: From [35].

where

$$f^{(2)}(\lambda) = [3.20 + 3.53 \sin^2(2\pi\lambda/3.33 + 1.34)] \times 10^{-6}. \tag{5.17}$$

Now, using the Langevin equation and the measured drift and diffusion coefficients, one concludes that the height fluctuations have their minimum value at $\lambda = 1$, which means a smoother surface at the optimal condition. Moreover, the approximants for the coefficients [Eqs. (5.14) and (5.16)] may be used to reconstruct the rough surfaces that are similar to the AFM images [30].

To complete the study, roughness of a surface can be also evaluated by the level-crossing analysis. Fig. 27 shows the observed average frequency ν_{α}^{+} as a function of h for several voltage biases. As λ is increased from 0 to 1, the value of ν_{α}^{+}

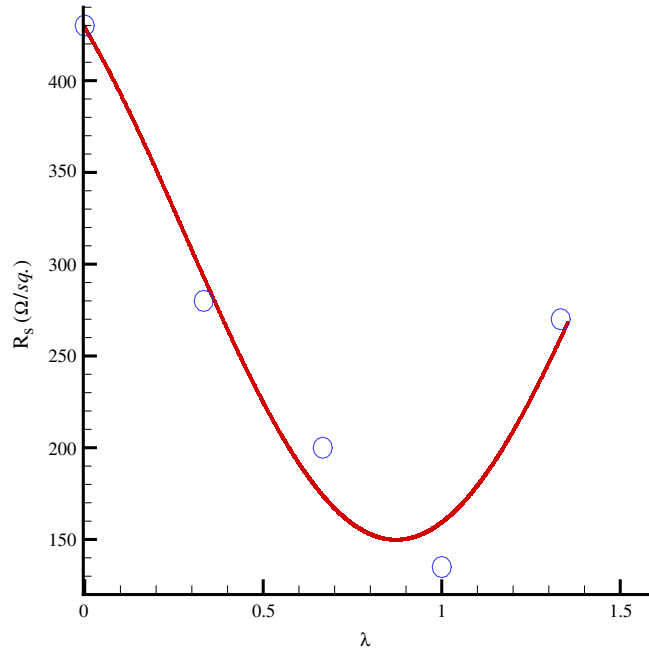


Fig. 28. Sheet resistance measurement of the coating layer as a function of the applied bias voltage.
Source: From [35].

decreases at any height. Once again, the optimal situation is observed for the voltage bias of -60 V, indicating that the surface formed at $\lambda = 1$ condition is a smoother surface with lower height fluctuations than the one formed under the other conditions. It is seen that for $\lambda = 4/3$ the height fluctuations of the surface take on the maximum value, as compared with the other surfaces. Similar to the behavior of the roughness exponent and the correlation length in terms of λ , the quantity N_{tot}^+ may be also expressed as:

$$N_{\text{tot}}^+(\lambda) = [1.20 + 0.17 \sin^2(2\pi\lambda/3.52 + 1.40)]. \quad (5.18)$$

Since the system under investigation has a thin Co layer, which is the only conductive layer, it is clear that the lower height fluctuations correspond to smaller electrical resistivity of the surface. Fig. 28 shows the resistance of the Co surface grown at the various voltage biases [35]. For the voltage bias ranging from 0 to -60 V, the resistance R_s is reduced from 432 to 131 Ω/sq . The minimum value of R_s is measured at the optimal condition of -60 V ($\lambda = 1$), which can be related to a modified and smooth surface roughness. Elimination of interfacial voids, as well as the porosity, reduces the impurities in the Co layer. A similar behavior was also observed at $V_{\text{opt}} = -50$ V for Ta/Si (111) system [292,293]. By increasing the applied biased voltage to values greater than its optimal value, surface roughness increases, due to the surface bombardment by high energy ions. This can be seen by the observed increase in the R_s value at the biased voltage of -80 V ($\lambda = 4/3$). It is easy to approximate the variation of R_s with λ by

$$R_s(\lambda) = [135.48 + 307.74 \sin^2(2\pi\lambda/3.93 + 1.77)]. \quad (5.19)$$

R_s behaves similar to the roughness characteristics of the surface. Therefore, it was shown that the roughness behavior explained by the statistical characterization of the surface, which was obtained by using microstructural analysis of the AFM, can be related to the sheet resistance measurement of the rough surfaces, as a tool of macrostructural analysis. Moreover, Sangpour et al. [35], studied the effect of the tip convolution [294,295] on the drift and diffusion coefficients. Their analysis showed that, although the measured values of the surface parameters by the AFM method are different from the real ones, the general behavior of the parameters as a function of the biased voltage is not affected by the tip convolution. In this direction, the stochastic nature of the etching surfaces was studied by [32] (see also [33]).

6. Applications: processes in scales

In this section we describe examples on the application of Markov method in scale for turbulence, passive scalar, financial and seismic time series. As mentioned in the introduction, the Markov method is also applicable to understanding the cascade nature of processes in scale and, therefore, intermittency issue of complex series. In this particular case the method has been used as an alternative and generalization of the multifractal description. Multifractals are usually analyzed by looking at the fluctuating quantities, such as velocity and temperature increments, etc., at each scale separately and as random variables.

The stochastic analysis of such systems uses scale-dependent quantities for their characterization. As described earlier, the term “scale” means that, for a data set $X(t)$ the scale r is the distance between two arbitrary points t and t' with $t' - t = r$ (t may denote time as well as space in this context). The *increment* $\Delta X(t, r) = X(t+r) - X(t)$ is a common scale-dependent complexity measure of a given system. Traditionally, the investigation of the statistical properties is performed on distinct scales, e.g., by means of the structure functions $\langle \Delta X(t, r)^n \rangle$, given by the probability density functions (PDF) $p(\Delta X(t, r))$. Here, using the Markovian approach we try to describe the joint statistics of the selected measure on many different scales. This is achieved by the knowledge of the joint PDF $p(\Delta X(t, r_1); \dots; \Delta X(t, r_n))$. Through such joint PDFs the correlations between the scales are also worked out, showing how the complexity is linked between scales.

Using the Markovian method, one can measure the Kramers–Moyal (KM) coefficients for the increments. For almost of the processes, the first and second KM coefficients are nonzero and significant, whereas the third- and fourth-order coefficients tend to zero. Therefore, by addressing the implications dictated by the theorem, a Fokker–Planck evolution operator is developed. The Fokker–Planck equation for $p(\Delta X, r)$ is used to obtain information on changing the shape of PDF as a function of the length scale r [10,14].

6.1. Turbulence

Small-scale turbulence is not yet fully understood. A complete theory based on the Navier–Stokes equation has not been developed yet. Thus, our present understanding relies for the most part on phenomenological and experimental approaches. It is typically assumed that turbulence forms a *universal* state which exhibits stationarity, isotropy and homogeneity in a statistical sense [296,55]. In general, turbulence is driven on large scale, i.e., the energy is injected into large-scale motion and is dissipated on the small scales, resulting in a net flux of energy from large to small scales [297]. The energy flux results from the inherent instability and the subsequent breakup of vortices into smaller ones.

For locally isotropic turbulence the main challenge is to understand the spatial correlation. Usually the turbulent velocity field $\mathbf{U}(\mathbf{x}, \mathbf{t})$ is characterized by increments $u_r = \mathbf{e} \cdot [\mathbf{U}(\mathbf{x} + \mathbf{r}, t) - \mathbf{U}(\mathbf{x}, t)]$, where \mathbf{e} denotes a unit vector in a certain direction, \mathbf{x} denotes a reference point and \mathbf{r} a displacement vector. The increments are taken as stochastic variables that depend on the scale variable $r = |\mathbf{r}|$. By varying r the correlations on various scales can be studied. In the following we denote by u_r the longitudinal increments, which means that \mathbf{e} is parallel to \mathbf{r} , and v_r to represent the transversal increments, for which \mathbf{e} is orthogonal to \mathbf{r} . For a specific length r_i we simply use u_i and v_i . The central challenge in turbulence is to explain the statistics of the exceptional frequent occurrence of large velocity increments on small scales r , which cannot be understood with the usual statistics. This is the so-called intermittency problem.

The work of Kolmogorov is still the theoretical foundation of the small-scale turbulence [298,299]. The starting hypothesis is that the possible symmetries of the Navier–Stokes equation are recovered in a statistical sense for high Reynolds number flows. The symmetries include homogeneity, i.e., the statistics of the increments being independent of the reference point \mathbf{x} ; isotropy, implying that the statistics do not change under rotation of the frame of reference, and stationarity, meaning that the statistics are not time dependent. A further hypothesis is scale invariance. Loosely speaking, scale invariance means that the structures of different scales look similar (see Eqs. (4.1)–(4.6) for more details). Kolmogorov considered the statistics in terms of the structure functions (moments of the velocity increments), for which scale invariance reads as $\langle u_r^n \rangle = (r/r_1)^{\xi_n} \langle u_{r_1}^n \rangle$ implying $\langle u_r^n \rangle \propto r^{\xi_n}$ with two different scales, r and r_1 .

Using this hypothesis, Kolmogorov furthermore assumed that for high Reynolds number flows the statistics of the velocity increments depend only on the energy dissipation ϵ and the scale r , and ended up by using dimensional arguments with $\langle u_r^n \rangle = C_n \epsilon^{n/3} r^{n/3}$ for $\eta \ll r \ll L$. C_n is called the Kolmogorov constant, η is the scale where the dissipation takes place, and L , the integral length scale, is the largest scale of the flow. However, there are corrections due to the fluctuating dissipation energy, leading to deviations from the exponent $\xi_n = n/3$. This property of turbulence is an other aspect of the above mentioned intermittency. According to the refined self-similarity hypothesis (RSH) of Kolmogorov, which takes into account the fluctuating energy dissipation $\langle \epsilon_r \rangle$, averaged over a volume V with the extension r ($\epsilon_r = \int_V \epsilon dx$), the scale invariance is expressed by

$$\langle u_r^n \rangle = c_n \langle \epsilon_r^{n/3} \rangle r^{n/3} \propto r^{\xi_n}. \quad (6.1)$$

The first model for the exponents ξ_n is Kolmogorov’s log-normal model, which results in $\xi_n = n/3 - \mu n(n-3)/18$ [300]. If, instead of the structure functions, the probability density functions (PDF) $p(u_r)$ are considered, this nontrivial scaling behavior corresponds to a change of the form of the PDFs with r . To explain the intermittency, i.e., the nontrivial scaling behavior, is still one of the most prominent challenges in turbulence; see, for example, [301]. These scaling exponents for Kolmogorov theories can easily be expressed by stochastic processes evolving in the scale. Following the Eq. (4.13) and setting

$$D^{(1)}(u_r, r) = -\left(\frac{1}{3} + 2Q\right) \cdot \frac{u_r}{r}; \quad D^{(2)}(u_r, r) = Q \frac{u_r^2}{r}$$

we see that the $\xi_n = n/3$ scaling is the trivial solution for $Q = 0$, whereas Kolmogorov’s log-normal scaling corresponds to a cascade process with multiplicative noise, $Q = \mu/18$ (see also [205]).

At first, the studies were only concentrated on the longitudinal increments. There was hope that the exponent ξ_n can describe the self-similarity of every quantity of the velocity field. But, recently, considerable efforts were devoted to also understanding the transverse increments, as they seem to have essential distinct properties [302,57,58,138,303–309,128,129,310–323,226,324,325]. This implies that the models as well as the considerations concerning only the longitudinal increments are too specific, and a better understanding of the turbulence has to include the transverse increments.

Longitudinal and transverse increments belong to different geometric/kinematic structures in the flow. The longitudinal increments is associated with strain-like structures, the transverse increments with vorticity-like structures. Thus, it is natural to modify the RSH of Eq. (6.1) and to use local averaged enstrophy (squared vorticity) rather than local averaged dissipation for the transverse increments. This is referred to as the refined similarity hypothesis (RSHT) for transverse increments (see, for example, [128,129,310–312])

$$\langle v_r^n \rangle = C_{t,n} \langle \Omega_r^{n/3} \rangle r^{n/3} \propto r^{\xi_{t,n}}. \tag{6.2}$$

If intermittency results from the fluctuating energy dissipation and enstrophy, then, the deviations from the Kolmogorov theory of 1941 can be investigated by the scaling of $\langle \epsilon_r^{n/3} \rangle$ and $\langle \Omega_r^{n/3} \rangle$, respectively [298,299]. For infinite high Reynolds number the scaling of the averaged dissipation and enstrophy should be the same [321], but in many experiments and simulation one observes differences in both exponents for finite Reynolds numbers [302,306,310–312,308,309,304,315,326,322,325,327].

At least four arguments are used to explain such observations. They are based on, (1) anisotropy, (2) the effect of the Reynolds number, (3) the influence of the boundary conditions, and (4) the intermittency. Anisotropy typically exists in every flow on large scales and can influence the exponent stronger than the intermittency itself [326,325]. Decreasing the Reynolds number affects the scaling exponents in such a way that the differences between them increase [328,315,326,323,325].

The structure functions $\langle u_r^n \rangle$ and $\langle v_r^n \rangle$, as well as the scaling properties involved, cannot define unambiguously the turbulent field. For instance, flows with different structures may have the same scaling properties [327]. The same is true for the probability distributions $p(u_r)$ and $p(v_r)$, which are in essence equivalent to the structure functions. The reason is that these quantities are just two-point statistics.

Definitively more general and detailed are the multipoint (or multiscale) distributions $p(u_1, v_1, r_1; \dots; u_n, v_n, r_n)$ (or multiscale structure functions $\langle \prod_i u_i^{m_i} \prod_j v_j^{m_j} \rangle$) for separate scales r_i . Such probabilities also consider the joint statistics of the longitudinal and transverse increments and, thus, enable one to also describe the interaction between them. Furthermore, they describe the simultaneous occurrence of the increments u_i, v_i on several length scales r_i .

In this section, we focus on the Markovin approach to characterization of the multiscale statistics. It has been shown that, it is possible to gain access to the joint probability distribution $p(u_1, r_1; u_2, r_2; \dots; u_n, r_n)$ via a Fokker–Planck equation, constructed directly from the measured data [10,329]. This has attracted interest and has been applied to various problems of the complexity of turbulence, such as the energy dissipation [330–333], universality of turbulence [334], the theoretical derivation of the Fokker–Planck equation from the Navier–Stokes equation in the limit of high Reynolds number [12] and the analysis of stochastic time series for turbulence [335,90,336,18,39,30,21,22]. As already emphasized, the characteristic of the Markovin method is that, it is based on pure data analysis, i.e., it is a parameter-free method, and that the few underlying assumptions are verifiable. Thus, no special model ideas are interwoven with the procedure.

Using the two-dimensional Fokker–Planck equation for the longitudinal and transverse increments, one can estimate the mixed structure functions $\langle u^m v^n \rangle = \int u^m v^n p(u, v, r) dudv$ [337]:

$$\begin{aligned} -\frac{\partial}{\partial r} \langle u^m v^n \rangle &= +m \langle u^{m-1} v^n D_1^{(1)}(u, v, r) \rangle + n \langle u^m v^{n-1} D_2^{(1)}(u, v, r) \rangle + \frac{m(m-1)}{2} \langle u^{m-2} v^n D_{11}^{(2)}(u, v, r) \rangle \\ &+ \frac{n(n-1)}{2} \langle u^m v^{n-2} D_{22}^{(2)}(u, v, r) \rangle + mn \langle u^{m-1} v^{n-1} D_{12}^{(2)}(u, v, r) \rangle. \end{aligned} \tag{6.3}$$

This equation allowed a direct comparison of the Fokker–Planck equation with the structure functions [337]. Two data sets measured in the central region of a wake behind a cylinder were used. The Reynolds numbers were $R_\lambda = 180$ and $R_\lambda = 550$, respectively. Unless specified otherwise, the data set with $R_\lambda = 180$ is used. The high Reynolds number data set was used for comparison.

6.1.1. Two-point statistics

First of all, let us characterize the data by two-point statistics (structure functions, PDF of the increments, etc.). A central pre-assumption for many considerations of small-scale turbulence is the isotropy. To study isotropy, one uses the Kármán equation (isotropy relation), because it is the simplest exact relation for the structure functions that rely on isotropy. The Kármán equation connects the second-order longitudinal and transversal structure functions:

$$\langle v_r^2 \rangle = \langle u_r^2 \rangle + \frac{r}{2} \frac{\partial}{\partial r} \langle u_r^2 \rangle. \tag{6.4}$$

Fig. 29 shows the left and right hand side of the Kármán equation, i.e., the second transverse structure function and the hypothetical transverse structure function for isotropic flows, calculated based on the longitudinal one. Taking the validity

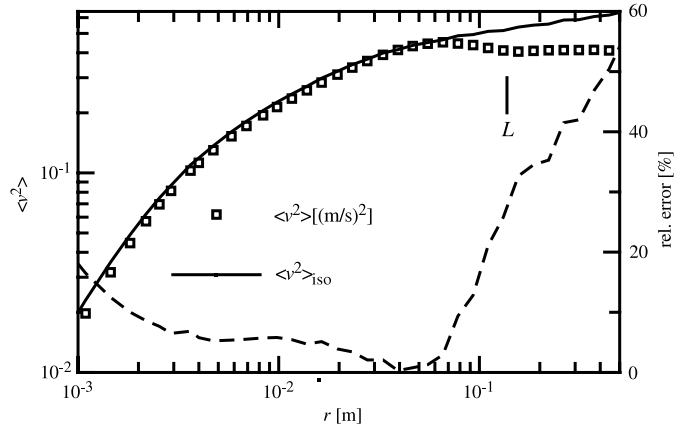


Fig. 29. Second-order transverse structure function estimated based on the one hand directly from the data (squares) and, on the other hand, based on the longitudinal structure function via the Kármán equation (straight line), i.e., the left and right hand side of Eq. (6.4). The relative deviations are shown by a dashed line. For small scales $r < L$ the Kármán equation is well fulfilled within 5% and is isotropic in this sense. On larger scales the data indicate clearly anisotropy.

Source: From [337].

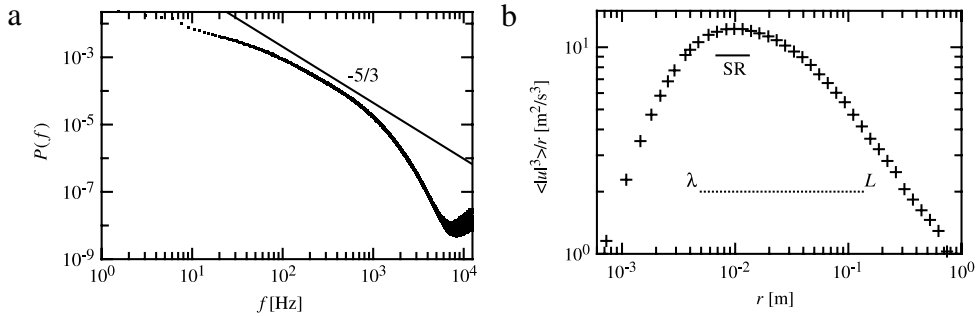


Fig. 30. (a) Energy spectrum (dots) with a $-5/3$ -power law, and (b) the compensated plot of the third-order structure function. The plateau of $\langle |u_r^3| \rangle / r$ defines the scaling range. The data are for $R_\lambda = 180$.

Source: From [337].

of the Kármán equation as indication of the isotropy, one sees that for small distances $r < L$ the isotropic relation is well fulfilled; the relative error is within 5%. For large distances $r > L$, isotropy is violated (large-scale anisotropy), with the ratio $\langle v_r^2 \rangle / \langle u_r^2 \rangle$ being approximately 0.66, which is a typical value in the literature.

Next, let us review the analysis of the data with respect to the scaling properties [337]. Fig. 30(a) shows the energy spectrum, together with the Kolmogorov’s $-5/3$ -law for comparison. In Fig. 30(b) the third-order structure function is plotted in a compensated representation, i.e., $\langle |u_r^3| \rangle / r$ is plotted against r to estimate the scaling range. The maximum lies at 10^{-2} m, which defines according to Kolmogorov’s $4/5$ -law the position and the width of the scaling range.

Because the scaling range is narrow, one can use the extended self-similarity (ESS) [338,339];

$$\langle |u_r|^n \rangle \propto \langle |u_r|^3 \rangle^{\xi_n^l} \tag{6.5}$$

$$\langle |v_r|^n \rangle \propto \langle |u_r|^3 \rangle^{\xi_n^t} \tag{6.6}$$

to estimate the scaling exponents of the structure functions. Fig. 31 shows the application of the ESS to the third-, fourth-, and sixth-order structure functions. The third-order structure function is of special interest, because it serves as the reference in the ESS. It can be seen in all the three figures that the transverse exponent is smaller than the longitudinal one, $\xi_n^t < \xi_n^l$. This result is well accepted [306,315,313,226,128,129]. To make this more clear, Fig. 32 shows the exponents ξ_n^l and ξ_n^t up to order 8. For the sixth-order structure function one finds, $\xi_6^l = 1.76 \pm 0.04$. Fitting Kolmogorov’s log-normal model to the values of ξ_n^l yields the intermittency parameter $\mu = 0.24$ [300]. Both estimates are in good agreement with the experimentally expected values; see, for example, [340]. The transverse exponents are clearly smaller than the longitudinal exponents for $n > 3$, i.e., the transverse structures are significantly more intermittent; see Fig. 32.

An other quantity that enables one to quantify intermittency is the flatness $F_\alpha \equiv \langle \alpha^4 \rangle / \langle \alpha^2 \rangle^2$, where α is u_r or v_r , respectively. For a Gaussian distribution, $F_\alpha \equiv 3$, and for an intermittent distribution, $F_\alpha > 3$. As shown in Fig. 33, for

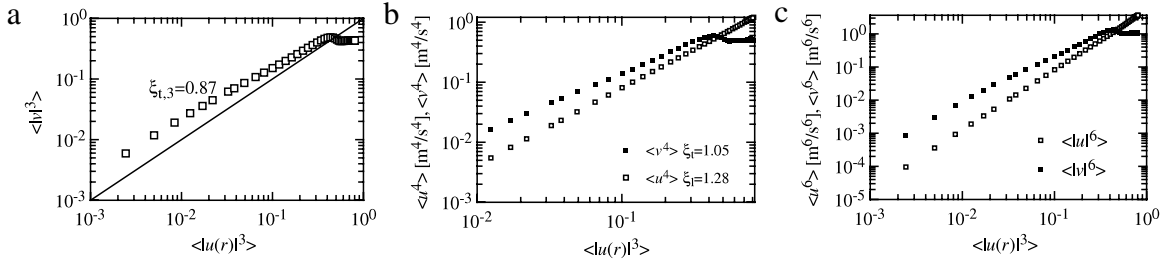


Fig. 31. The ESS representation of the longitudinal and transverse structure functions. (a) The transverse third-order structure function versus the longitudinal third-order structure function. The exponent is $\xi_{t,3}^t = 0.87$. The line has a slope of 1, which is expected from Kolmogorov’s 4/5-law for the third-order longitudinal structure function. (b) The fourth-order structure functions, and (c) the sixth-order structure functions. Clear difference between the longitudinal and transverse structure functions can be discerned.
 Source: From [337].

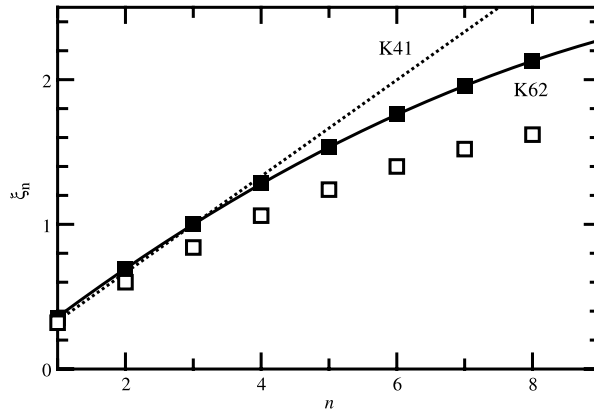


Fig. 32. The scaling exponents estimated with the ESS. Bold squares: the scaling exponents ξ_n^l up to order 8. The dotted line is the forecast of Kolmogorov’s 1941 theory. The straight line includes the intermittency corrections of Kolmogorov’s 1962 theory with the fitted intermittency parameter $\mu = 0.24$. Open squares: transverse exponents.
 Source: From [337].

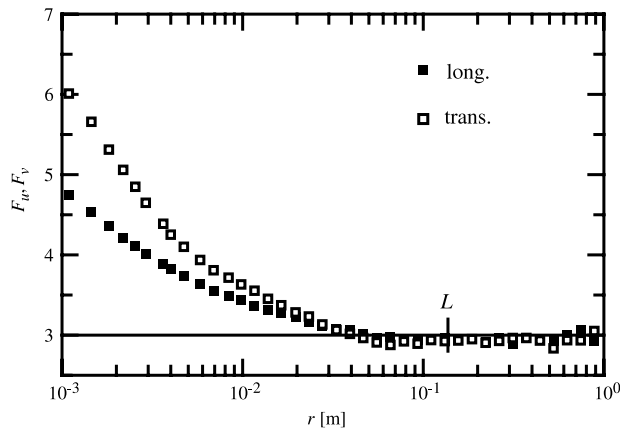


Fig. 33. Flatness of the longitudinal and transverse increments. For scales $r < L$ the flatness lies for both components over the Gaussian value of 3. Furthermore, the flatness is larger for the transverse component, i.e., it is more intermittent.
 Source: From [337].

$r < L$ both components are intermittent. For small r the transverse increments are considerably more intermittent than the longitudinal one.

In Fig. 34 the probability density of the longitudinal and transverse velocity increments are plotted. The velocity distribution on each scale is normalized with the respect to the respective standard deviation, i.e., $u_\sigma := u_r/\sigma_{u,r}$ and $v_\sigma := v_r/\sigma_{v,r}$, in order to compare only the form of the curves. In Fig. 35 the longitudinal and transversal probability densities for two different length scales ($r = L/5$ and $r = \lambda$) are shown. In both figures, the intermittent character of

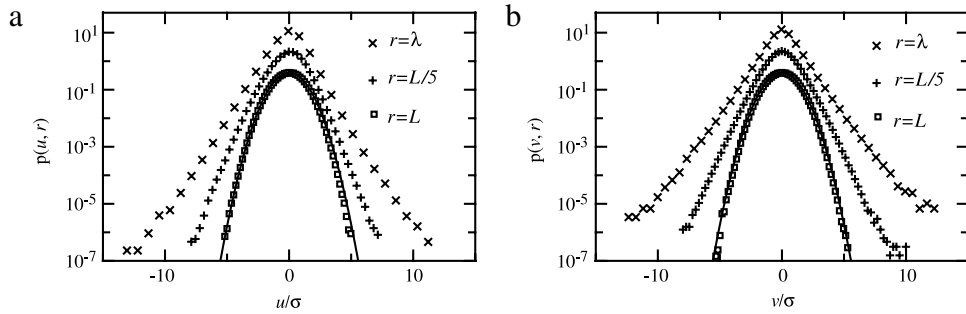


Fig. 34. Probability density functions (PDFs) for, (a) longitudinal, and (b) transverse increments on three different length scales $r = L, L/5, \lambda \approx \lambda$. The PDFs' width are normalized with respect to their standard deviations and are shifted along the axis for a better representation. On the largest scale L a Gaussian distribution is fitted for comparison. Toward smaller scales the deviations from the Gaussian form become obvious.

Source: From [337].

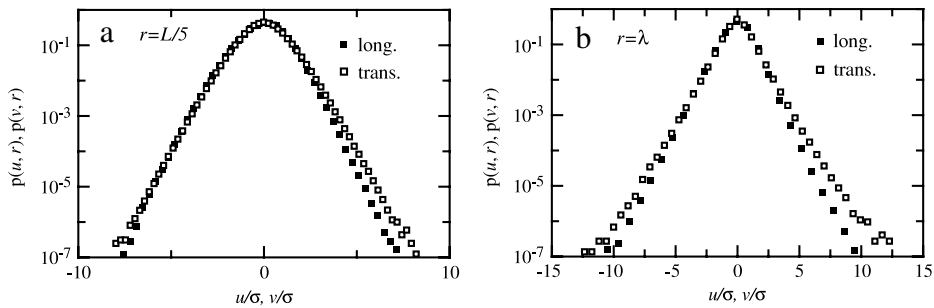


Fig. 35. A direct comparison between the longitudinal and transverse PDFs for, (a) $r = L/5$, and (b) $r = \lambda$. The longitudinal PDFs are represented by black squares, the transverse PDFs by white squares. The width of the PDFs are normalized with respect to their standard deviation. For $r = L/5$ the deviations are mainly given by the skewness, for $r = \lambda$ also differences in intermittency, i.e., exponential tails, occurs.

Source: From [337].

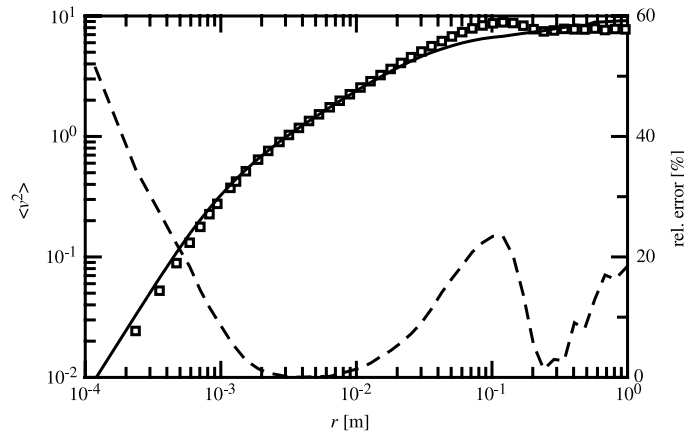


Fig. 36. The second-order transverse structure function, calculated from the data (squares) and from the longitudinal structure function via the Kármán equation (line). Because the differences in the scaling range cannot be discerned, the relative errors between them are also plotted (dashed line). $R_\lambda = 550$. Source: From [337].

the statistics can be seen. For $r = L/5$ the main difference is seen only for positive increments, i.e., the main difference is the skewness [337].

Now, let us state briefly the results from the high Reynolds number data set. The Kármán equation is well fulfilled, i.e., the data are isotropic to a good degree of approximation; see Fig. 36. Fig. 37a presents the energy spectrum of the longitudinal increments that shows a distinct scaling range with the exponent $-5/3$, in agreement with the Kolmogorov's theory [337]. The scaling range is more pronounced for this data set, as can be seen also from the third-order structure function; compare Figs. 37(b) and 30(b).

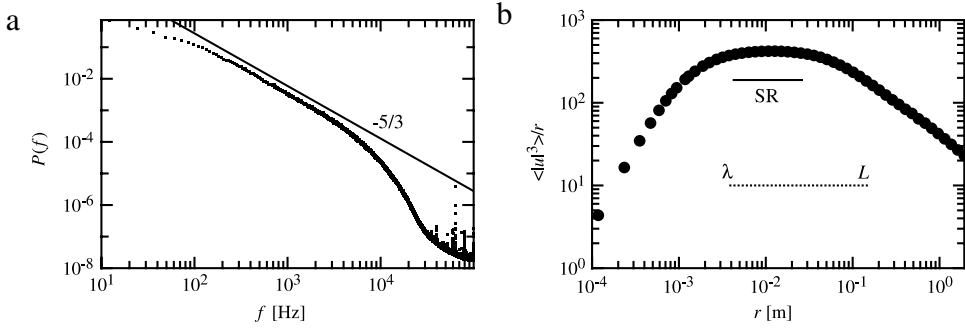


Fig. 37. (a) Energy spectrum (dots) with a $-5/3$ -power law, and (b) the third-order structure function for $R_\lambda = 550$. The plateau of $\langle |u|^3 \rangle / r$ defines the scaling range.

Source: From [337].

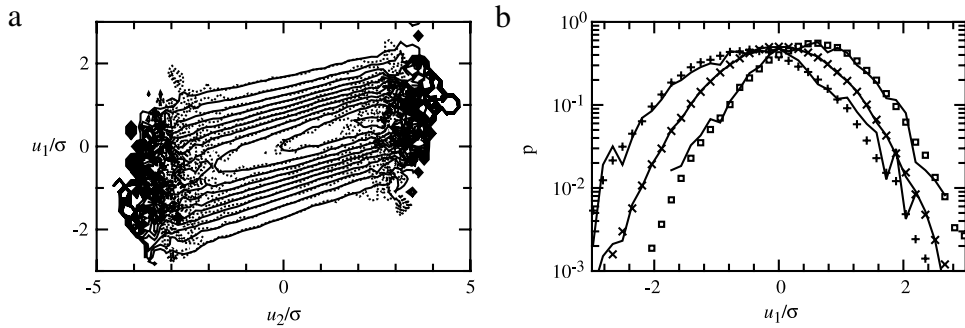


Fig. 38. (a) Contour plot of the single (straight line) and double conditioned probability distribution (dashed line), $p(u_1, r_1|u_2, r_2)$ and $p(u_1, r_1|u_2, r_2; u_3 = 0, r_3)$ of the longitudinal increments for the length scales, $r_1 = \Delta r, r_2 = 2\Delta r$, and $r_3 = 3\Delta r$ with $\Delta r = 68.3$ mm. The distance between the contour lines is $\Delta p = 0.05$. (b) Three cuts through the contour plot are presented for $u_2 = -2\sigma, u_2 = 0$, and $u_2 = 2\sigma$. It can be seen that the Markov properties are fulfilled.

Source: From [337].

So far, we have presented the results for the two-point statistics, i.e., the statistics of the increments for one fixed scale separately. In the following we describe the results of the Markov analysis of the interdependence between different length scales and the interaction between both the longitudinal and transverse increments.

6.1.2. Multipoint statistics: the Fokker–Planck analysis

In this section we present the analysis of the multipoint statistics separately for the longitudinal and transverse increments, as was described in the previous subsection [337]. As always, there are three steps: first, one checks the validity of the Markov properties. Second, one calculates the Kramers–Moyal coefficients to show that the data follow a diffusion process. At last, as a verification, one integrates the resulting Fokker–Planck equation for the simple and for the conditioned probability distribution, in order to show that the constructed Fokker–Planck equation describes correctly the data. Siefert et al. defined the increments for the multipoint examinations according to, $u_r := \mathbf{e} \cdot [\mathbf{U}(\mathbf{x} + \mathbf{r}/2) - \mathbf{U}(\mathbf{x} - \mathbf{r}/2)]$ [337].

6.1.3. Markov properties

The foundation for using the Markov analysis is the validity of the data being Markovian. This can be tested directly on the data by the definition, Eq. (3.6). Due to the number of the measured data points being finite, we restrict ourselves to the verification of $p(u_1, r_1|u_2, r_2) = p(u_1, r_1|u_2, r_2; u_3, r_3)$. Fig. 38 shows the plots of both sides of the equation for the longitudinal increments for the three length scales, $r_1 = \Delta r, r_2 = 2\Delta r$, and $r_3 = 3\Delta r$, with $\Delta r = 68.3$ mm $\approx L/2$. It is seen that both distributions coincide. For a length scale (l_m) below a certain threshold, the Markov properties are not fulfilled; see Fig. 39 [28].

To quantify the results and to get a more objective and systematic measure for the Markov properties and the Markov length, one can use the Wilcoxon test, which compares two random samples with sizes m and n [87]. For the Wilcoxon test, one must count the number of inversions of two samples, here for the single and double conditioned variable $u_1|u_2$ and $u_1|u_2, u_3$. One calculates $\langle t \rangle := |Q - \langle Q \rangle_{\bar{p}=p}| / \sigma(m, n)$, where Q is the number of inversions calculated from the experimental data for the variables $u_1|u_2$ and $u_1|u_2, u_3$, $\langle Q \rangle_{\bar{p}=p} = mn/2$, and $\sigma(m, n) = \sqrt{mn(m+n+1)/12}$ are the number of inversions and the standard deviation, respectively, assuming that both variables have the same distribution. Thus, it is $\langle t \rangle = 1$, if both samples come from the same universe, or have the same distribution. Fig. 40 shows the measurement and its dependence

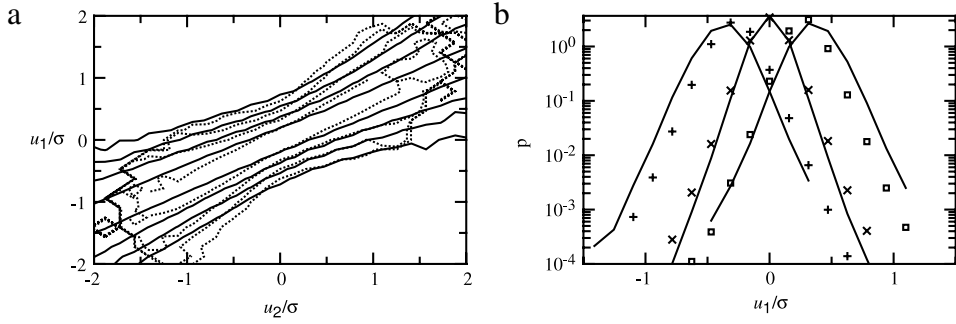


Fig. 39. Same as in Fig. 38, but for smaller values $\Delta r = 2.54 \text{ mm} \approx \lambda/3$. (a) Contour plot for the single conditioned (straight line) and double conditioned probability distribution (dashed line). Deviations between them are visible. The distance between the lines correspond to a factor 10. (b) Three cuts through the contour plot are presented for $u_2 = -2\sigma$, $u_2 = 0$, and $u_2 = 2\sigma$. It can be seen that the Markov property is not fulfilled. Source: From [337].

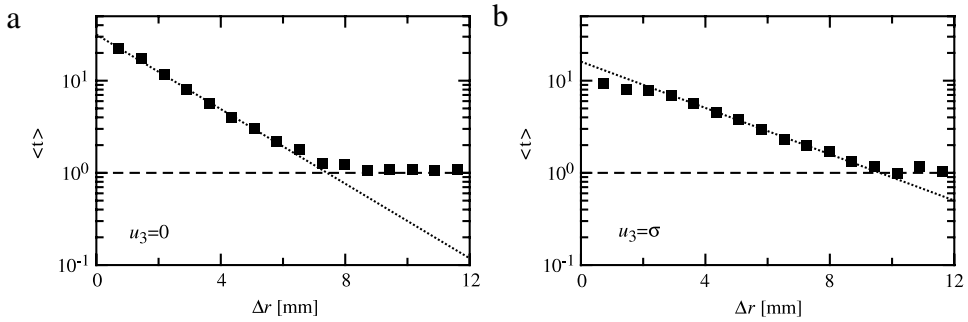


Fig. 40. The expectation value $\langle t \rangle$ of the Wilcoxon test and its dependence on the length scale differences Δr for the longitudinal increments with the reference scale, $r_1 = 14.64 \text{ mm}$, (a) for $u_3 = 0$, and (b) for $u_3 = \sigma$. The constant line marks the expectation value for the fulfilled Markov properties, the dotted line is an exponential decay. Source: From [337].

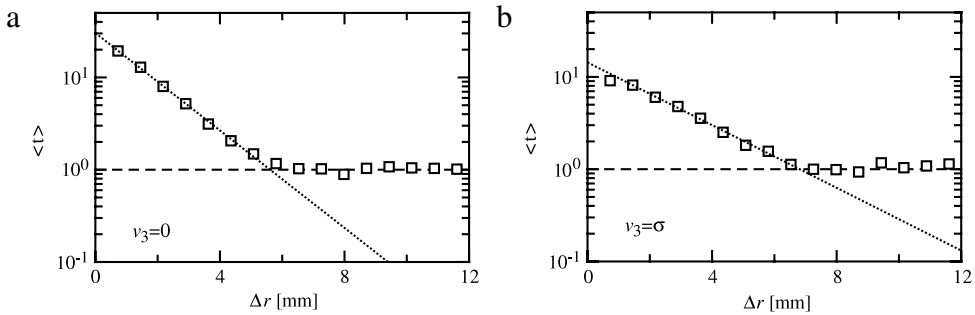


Fig. 41. The as in Fig. 40, but for the transverse increments. The only differences is in the smaller Markov length. Source: From [337].

on Δr . For small Δr the Markov properties are not fulfilled, whereas for larger distances the deviations are not significant anymore. Indeed, the distance $\Delta r = l_m$, where $\langle t \rangle$, drops to 1 and is the Markov–Einstein length scale. This value can be estimated by fitting an exponential function to the data and by interpreting the passage through the value 1 as the Markov–Einstein length, as presented in Fig. 40.

The Markov properties are also fulfilled for the transverse increments, but with a smaller Markov–Einstein length; see Fig. 41. The Markov–Einstein length varies within 20% with respect to the condition u_2 , but remains about constant with respect to r . For the longitudinal increments the Markov–Einstein length lies in the range $7.4 \text{ mm} < l_{m,l} < 9.6 \text{ mm}$, for the transverse increments the Markov–Einstein length lies in the range, $5.5 \text{ mm} < l_{m,t} < 6.8 \text{ mm}$. The ratio is $l_{m,l}/l_{m,t} \approx 1.4$, as it is known for the Taylor length λ [341]. We note that $l_m \approx \lambda$ [29]. The analysis of the data $R_\lambda = 550$ yield analogous results.

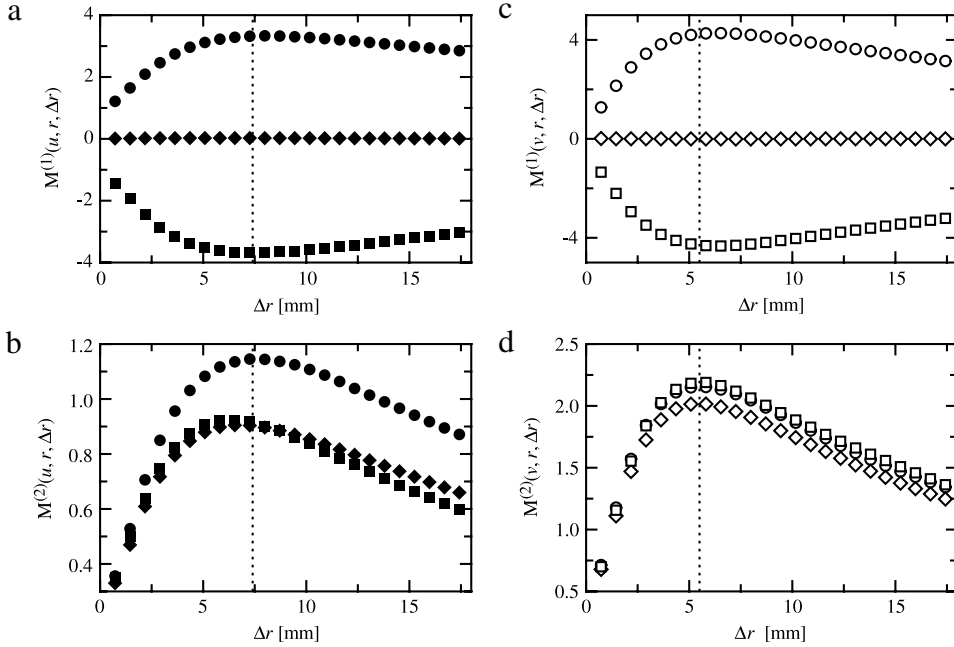


Fig. 42. The dependence of the coefficients $M^{(1)}$ and $M^{(2)}$ on the step size Δr for $r = L/2$. The two upper and two lower figures show, respectively, the limit of the drift and diffusion coefficients for the longitudinal and transverse increments. The dotted lines represent the Markov length. Circles: $u, v = -2\sigma$, diamonds: $u, v = 0$, squares: $u, v = 2\sigma$.

Source: From [337].

We conclude from the results that the ‘cascade’ of the longitudinal and transverse increments can be described by a Markov process for step sizes larger than the Markov–Einstein length l_m , which becomes important again for the estimation of the Kramers–Moyal coefficients, as described in the next section.

6.1.4. Kramers–Moyal coefficients

The drift coefficients $D^{(1)}$ and the diffusion coefficients $D^{(2)}$ are calculated according to Eqs. (2.40) and (2.41) directly from the measured data following the procedure described above and by [29,136]. The crucial point is the estimation of the limit $\lim_{\Delta r \rightarrow 0} M^{(i)}$; see Fig. 42. Only the points with $\Delta r > l_m$ are used to estimate the limit. For $\Delta r < l_m$ the Markov properties are violated, while for $\Delta r > l_m$ the dependence of $M^{(i)}$ on Δr is linear; see Fig. 42. Thus, one can use a first-order polynomial to extrapolate to the limit, $\Delta r \rightarrow 0$. The linear dependence is the first-order approximation of the limit; see [136].

The resulting drift coefficients $D^{(1)}$ and diffusion coefficients $D^{(2)}$ are shown in Fig. 43 for the length scale $r = L/2$. The drift coefficients can be approximated by a straight line with negative slope. Small deviations from this behavior are visible for the transverse component. For the diffusion coefficient qualitative differences between both increments are visible. In contrast to the transverse coefficient, the longitudinal coefficient is not symmetric under the reflection, $u \rightarrow -u$. This is compatible with Kolmogorov’s 4/5-law, which states that the longitudinal distributions are skewed. The diffusion coefficient can be approximated by a second-order polynomial, so we have

$$\begin{aligned} D^{(1)}(\alpha, r) &= d_1^\alpha(r)\alpha \\ D^{(2)}(\alpha, r) &= d_2(r) + d_2^\alpha(r)\alpha + d_2^{\alpha\alpha}(r)\alpha^2, \end{aligned} \quad (6.7)$$

where $\alpha = u, v$. Due to the reflection symmetry $v \rightarrow -v$ of the transverse increments, we have $d_2^v(r) \equiv 0$.

As described earlier, the drift and diffusion coefficients are the first two coefficients in the Kramers–Moyal expansion. We already pointed out that, according to the Pawula theorem all higher-order coefficients vanish, if the fourth-order coefficients are zero and, thus, the expansion simplifies to a Fokker–Planck equation. In Fig. 44 the fourth-order coefficients are plotted for $r = L/2$. The coefficient $D^{(4)}$ for the longitudinal coefficient vanishes within the error bars. The corresponding transverse coefficient has a value slightly above zero. But one can estimate with the Kramers–Moyal expansion that the contribution of this coefficient is less than one-hundredth of the diffusion term and, therefore, can be neglected.

Next, the r -dependence indicated by Eq. (6.7) is investigated. It can be estimated by fitting the approximation (6.7) to the numerical values of the Kramers–Moyal coefficients. The results are depicted in Fig. 45 for the longitudinal (black squares) and transverse increments (white squares). The approximates are remarkably simple, and may be represented by

$$D_1^{(1)} : d_{1,1}^u(r) = \alpha_{1,1}^u + \beta_{1,1}^u r \quad (6.8)$$

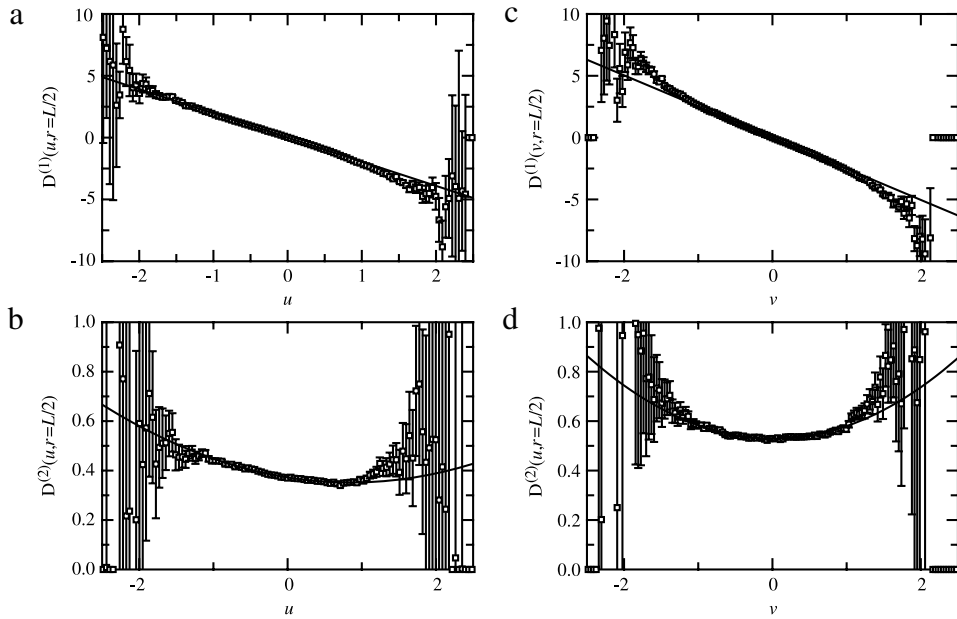


Fig. 43. The Kramers–Moyal coefficients $D^{(1)}$ and $D^{(2)}$ and their dependence on the increments u and v , respectively, for $r = L/2$. (a) and (b) the longitudinal, and (c) and (d) the transverse increments.
Source: From [337].

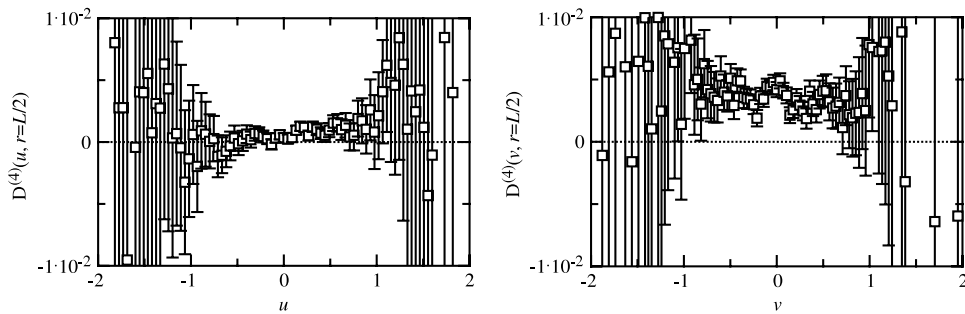


Fig. 44. The fourth-order Kramers–Moyal coefficients $D^{(4)}(u, r)$ and $D^{(4)}(v, r)$ for $r = L/2$. It is seen that within the error bars the longitudinal coefficient is zero. The transverse coefficient is slightly above zero, but its contribution to the Kramers–Moyal expansion is small.
Source: From [337].

$$\begin{aligned}
 D_t^{(1)} : d_{1,t}^v(r) &= \alpha_{1,t}^v + \beta_{1,t}^v r + \gamma_{1,t}^v r^2 \\
 D_1^{(2)} : d_{2,1}^u(r) &= \beta_{2,1}^u r, \quad d_{2,1}^u(r) = \beta_{2,1}^u r, \quad d_{2,1}^{uu}(r) = \alpha_{2,1}^{uu} \\
 D_t^{(2)} : d_{2,t}^v(r) &= \beta_{2,t}^v r, \quad d_{2,t}^{vv}(r) = \alpha_{2,t}^{vv} + \beta_{2,t}^{vv} r + \gamma_{2,t}^{vv} r^2.
 \end{aligned}$$

Here, we denote by X_l and X_t the longitudinal and transverse quantities, respectively.

6.1.5. Integration of the Fokker–Planck equation

Let us demonstrate how the Fokker–Planck equation can describe correctly the statistics of the turbulent field. In Fig. 46 $p(u, r)$ and $p(v, r)$ are shown for several length scales. The results are in good agreement with the data. It is important to also stress that the intermittency effects and the skewness can be described well. A similar calculation has been done for the conditional distributions $p(u, r|u_0, r_0)$ and $p(v, r|v_0, r_0)$, starting at the integral scale with Dirac's delta function $p(u, r = L|u_0, r_0 = L) = \delta(u)$ and $p(v, r = L|v_0, r_0 = L) = \delta(v)$ as the initial conditions. The solutions down to $r = L/2$ are shown in Figs. 47 and 48 and the dependence on the initial value u_0 and v_0 . Comparing the conditional probability distributions in Fig. 47 with those in Fig. 48 makes it evident that the transverse statistics relaxes faster (the contour lines are more horizontal).

On the basis of these results one concludes that the increment statistics can be well described by a Fokker–Planck equation, for which the drift and diffusion coefficients are given by Eq. (6.8).

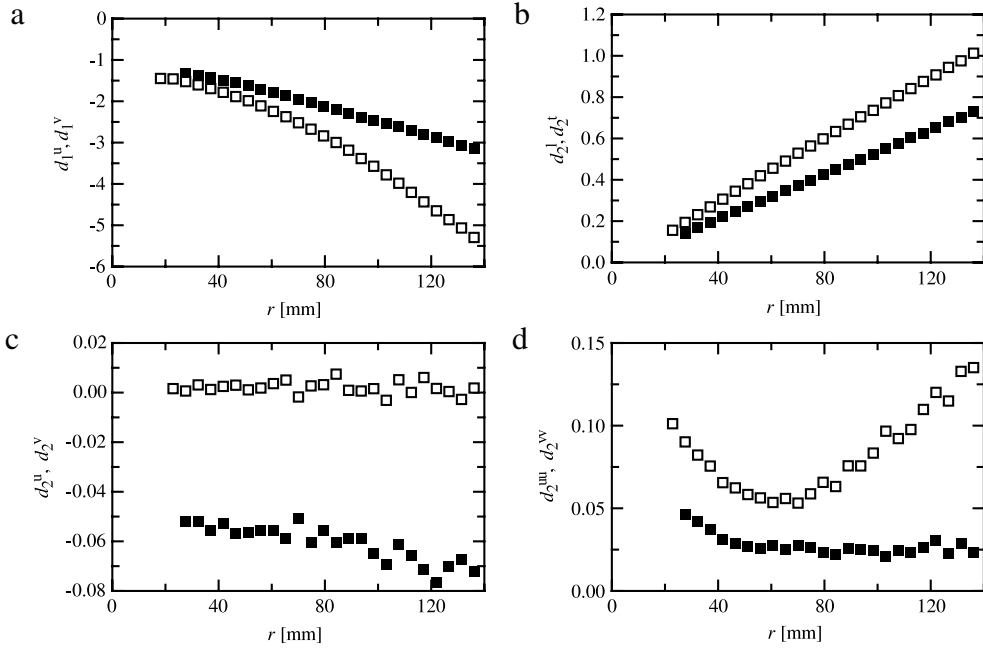


Fig. 45. The r -dependence of the expansions of the Kramers–Moyal coefficients according to Eq. (6.7) for the longitudinal (black squares; $\alpha = u$) and transverse increments (white squares; $\alpha = v$) if the notation is unique, we omit the index l or t .
 Source: From [337].

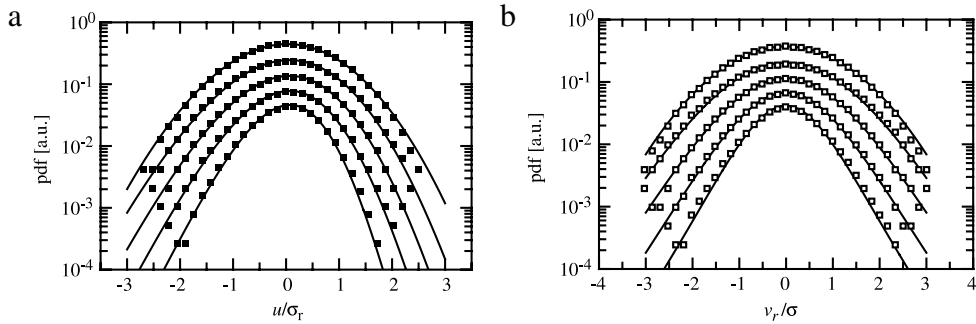


Fig. 46. The solution of the Fokker–Planck equation and its comparison with the data. With the initial distribution on the scale $r = L$, the Fokker–Planck equation was solved numerically. The curves belong to the scales (from top to bottom) $r = 131, 74, 41, 23$, and 12 mm. For a better visibility the curves are shifted by a constant factor. (a) The solution for the longitudinal, and (b) the transverse increments. In both figures the intermittency is visible, while for the longitudinal increments the skewness can also be seen.
 Source: From [337].

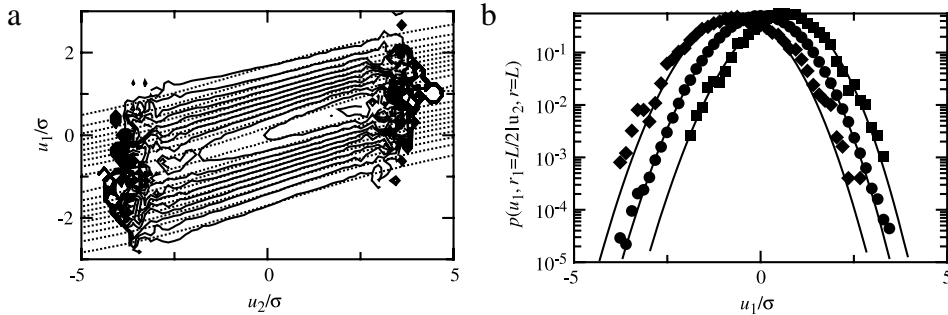


Fig. 47. The longitudinal conditional PDFs $p(u_2, r = L/2 | u_1, r = L)$, calculated from $r = L$ down to $r = L/2$. (a) The contour plot for the numerical solution (dashed line) and the PDFs calculated from the data (straight line). The distance between the contour lines is $\Delta p = 0.05$. (b) Cuts through the contour plot for $u_2 = -2.5\sigma, 0, 2.5\sigma$. The lines are the solution of the Fokker–Planck equation, the symbols represent the PDFs from the data.
 Source: From [337].

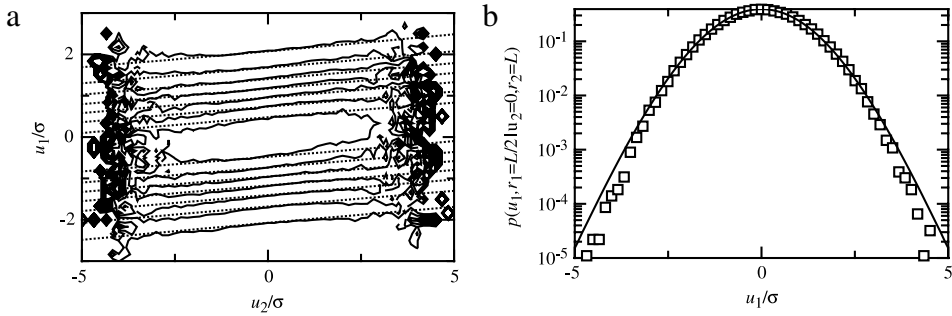


Fig. 48. The same as in Fig. 47, but for the transverse increments. (a) The contour plot for the numerical solution (dashed line) and the PDFs calculated from the data (straight line). The distance between the contour lines is $\Delta p = 0.05$. (b) Cuts through the contour plot for $u_2 = 0$. The line is the solution of the Fokker–Planck equation, the symbols represent the PDF from the data. Source: From [337].

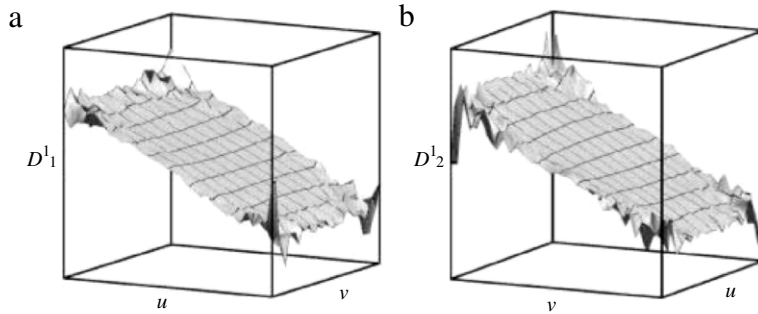


Fig. 49. The u - and v -dependence of the drift vector for the scale $r = L/4$. (a) The drift coefficient $D_1^{(1)}$, and (b) the drift coefficient $D_2^{(1)}$. Note that the vertical axis is rotated for a better comparison between (a) and (b). Both coefficients are purely linear and depend only on one variable. Source: From [337].

6.1.6. Joint multipoint statistics of longitudinal and transverse increments

In the preceding section we presented the results of analyzing the statistics of the longitudinal and transverse increments separately. But the separation is restrictive because the dynamics of both components is due to one velocity field and are, therefore, connected. They cannot be separated due to the nonlinear advection term in the Navier–Stokes equation. Therefore, let us extend the above analysis and examine the joint stochastic properties. We select both increments as one state with the scale parameter r . The aim is to construct a Fokker–Planck equation in terms of the two variables. One can proceed similar to the one-dimensional analysis. The main difference is that one needs much more data and must estimate many more coefficients, because the drift coefficients is now a vector, while the diffusion coefficient is a matrix.

The verification of the Markov properties for two variables is difficult, because one must estimate the double conditioned probability function for a two-dimensional process, i.e., a six-dimensional function with a finite number of data points. One needs approximately 10^4 times more data points, in comparison with the one-dimensional case, if the results are to be of similar significance. The limiting factor is the duration of the measurement and the amount of data. But, we know separately for both components that the Markov properties are valid. In general, if two variables have Markov properties, the joint statistics also have Markov properties, where as the opposite is not true in general [325]. Therefore, one can assume that the combined process is Markovian as well.

The next step is to estimate the Kramers–Moyal coefficients. First, one must calculate the approximation of the drift vector $M_i^{(1)}(u, v, r, \Delta r)$ and of the diffusion matrix $M_{ij}^{(2)}(u, v, r, \Delta r)$ and their dependence on Δr . The shape of the drift and diffusion coefficients are shown in Figs. 49 and 50 for the length scale $L/4$. The drift coefficients have a simple form: they depend only linearly on one variable; see Fig. 49. This means the process decouples in the deterministic part. The diagonal coefficients of the diffusion matrix are shown in Fig. 50(a) and 50(b). Roughly spoken, they consist of a curved surface shifted upwards with a minimum at $u > 0$ and $v = 0$. The off-diagonal coefficient $D_{12}^{(2)}$ (it is $D_{12}^{(2)} \equiv D_{21}^{(2)}$) has a saddle shape; see Fig. 50(c).

One can approximate the form of the drift and diffusion coefficients by a low-order polynomial in u and v [337]:

$$\begin{aligned}
 D_1^{(1)}(u, v, r) &= d_1^u(r)u \\
 D_2^{(1)}(u, v, r) &= d_2^v(r)v \\
 D_{11}^{(2)}(u, v, r) &= d_{11}(r) + d_{11}^u(r)u + d_{11}^{uu}(r)u^2 + d_{11}^{uv}(r)v^2
 \end{aligned} \tag{6.9}$$

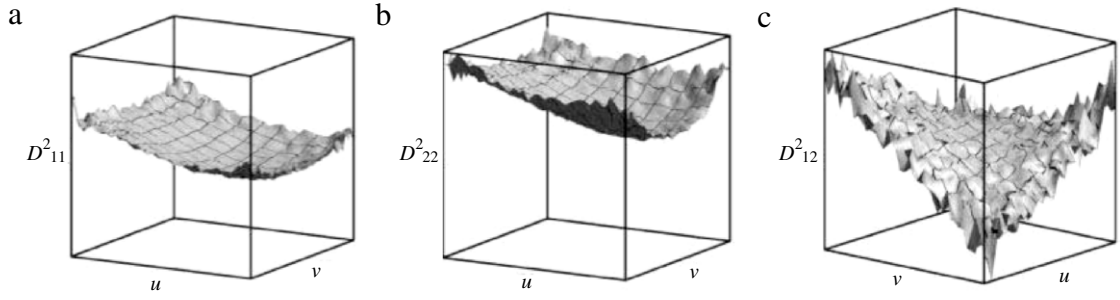


Fig. 50. The u - and v -dependence of the diffusion matrix for the scale $r = L/4$. (a) The coefficient $D_{11}^{(2)}$, and (b) the coefficient $D_{22}^{(2)}$. The diagonal coefficients are not constant, but have a parabolic form, which is more pronounced for the $D_{22}^{(2)}$ coefficient (multiplicative noise). Both coefficients are symmetric under reflection with respect to $v \rightarrow -v$, but not for $u \rightarrow -u$. (c) The saddle-formed off-diagonal coefficient.
Source: From [337].

$$D_{22}^{(2)}(u, v, r) = d_{22}(r) + d_{22}^u(r)u + d_{22}^{uu}(r)u^2 + d_{22}^{vv}(r)v^2$$

$$D_{12}^{(2)}(u, v, r) = d_{12}(r) + d_{12}^v(r)v + d_{12}^{uv}(r)uv.$$

The d -coefficients contain the r -dependence. Their lower index labels the associated Kramers–Moyal coefficient, the upper index the order of the coefficient with respect to u and v . In the Fokker–Planck equation, the coefficients occur symmetrically with respect to reflection $v \rightarrow -v$. Thus, a reflection $v \rightarrow -v$ does not change anything, whereas the symmetry is violated for the longitudinal increment. Of course, the Kramers–Moyal coefficients can be better approximated using higher-order polynomials in u and v , but their contributions are small and their value are not well defined at the edges of the available data range, because high velocities are too rare to ensure a good statistics. Note, the significance of the higher-order terms in $D^{(1)}$ and $D^{(2)}$ is considerable for the closure of Eq. (6.3), but their investigation is not addressed here.

In order to describe the statistics with the Fokker–Planck equation completely, the r -dependence of the d -coefficients must be estimated; see Fig. 51. They can be approximated by [337],

$$D_1^{(1)} : d_1^u(r) = \alpha_1^u + \beta_1^u r \quad (6.10)$$

$$D_2^{(1)} : d_1^v(r) = \alpha_1^v + \beta_1^v r + \gamma_1^v r^2$$

$$D_{11}^{(2)} : d_{11}(r) = \beta_{11} r, \quad d_{11}^u(r) = \beta_{11}^u r, \quad d_{11}^{uu}(r) = \alpha_{11}^{uu}, \quad d_{11}^{vv}(r) = \alpha_{11}^{vv}$$

$$D_{22}^{(2)} : d_{22}(r) = \beta_{22} r, \quad d_{22}^u(r) = \beta_{22}^u r, \quad d_{22}^{uu}(r) = \alpha_{22}^{uu}, \quad (6.11)$$

$$d_{22}^{vv}(r) = \alpha_{22}^{vv} + \beta_{22}^{vv} r + \gamma_{22}^{vv} r^2 \quad (6.12)$$

$$D_{12}^{(2)} : d_{12}^v(r) = \beta_{12}^v r, \quad \alpha_{12}^{uv} + \beta_{12}^{uv} r + \gamma_{12}^{uv} r^2.$$

Indeed, it must be shown that the Fokker–Planck equation, together with the coefficients (6.9) and (6.10), can reproduce the statistics of the measured data. Figs. 52 and 53 show the results for the experimental measured and integrated PDFs. Due to the good agreement one can conclude that the d coefficients can be used to characterize the statistics of the longitudinal and transverse increments.

From the above analysis it appears that the drift and diffusion coefficients contain the information of the small-scale statistics of the turbulence. More specifically, they contain the joint statistics of the longitudinal and transverse increments, as well as the statistics on multiscales. It was shown that in the first approximation the longitudinal and transverse drift and diffusion coefficients can be transformed to each other by a simple rescaling, namely, by multiplying the scale of the longitudinal increments with the factor $3/2$ [337]. With this rescaling the frequently discussed issue of the differences between the longitudinal and transverse structure functions can be explained. Moreover, it has been found that the $3/2$ rescaling can be interpreted as different speed of the longitudinal and transverse cascade, and is compatible with the Kármán equation [337]. Therefore, analyzing the statistics by means of a Fokker–Planck equation provides further insights in the complexity of the cascading process.

6.2. Passive scalar

Since Kolmogorov’s pioneering work on the “turbulent cascade”, the structure and potential universality of small-scale turbulence, has received much attention [298,299]. As mentioned in the previous subsection, the cascade notion relates to the transport of kinetic energy from large to small scales. Turbulent kinetic energy is injected into a flow at the largest scales (i.e., scales related to the boundary conditions of the flow). The inherent instability of large eddies subsequently transfers kinetic energy to smaller and smaller scales, until the smallest eddies convert their kinetic energy into internal energy by the action of viscosity, thus ending the cascade. The length of the cascade (which can be specified in terms of the ratio of the

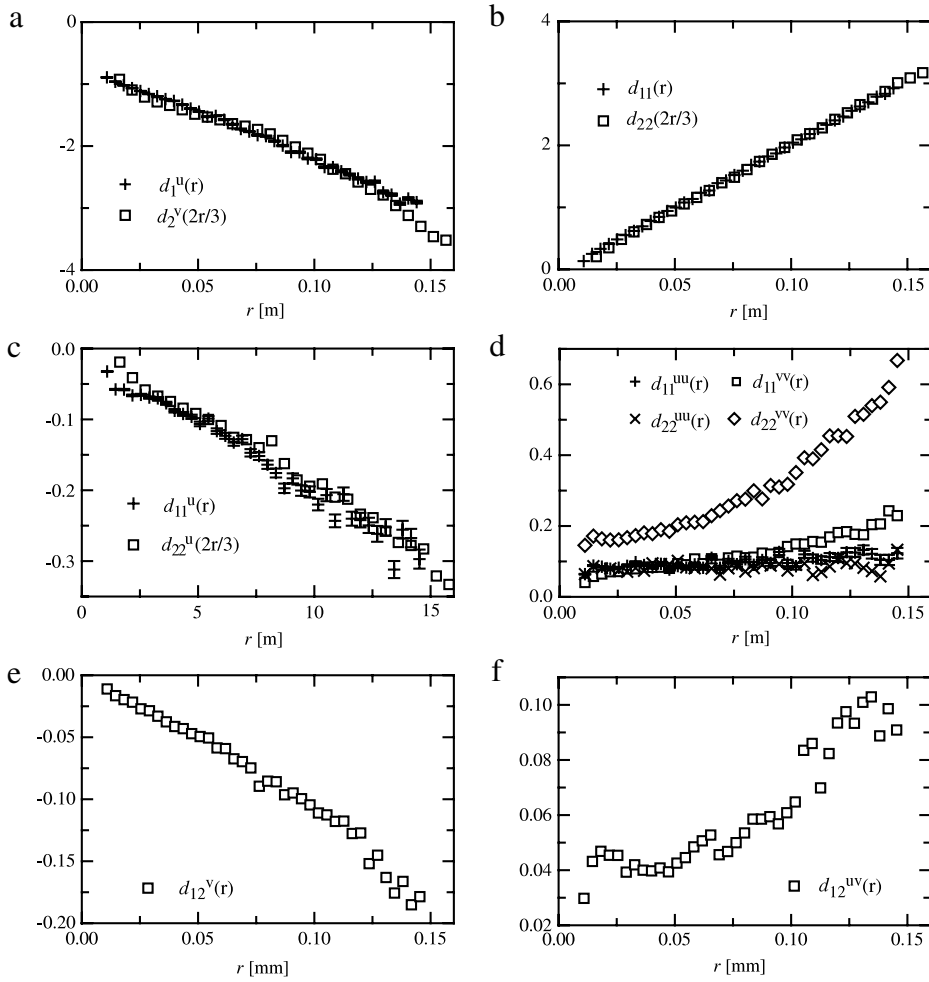


Fig. 51. The coefficients d of Eq. (6.9), which reflect the dependence of the Kramers–Moyal equation on u and v on the linear scale variable r . In parts. (a), (b) and (c) the argument of the transversal coefficient is rescaled by the factor $2/3$. The corresponding longitudinal and transverse coefficients coincide with each other, apart from the intermittency term d_{22}^{vv} . (e) and (f) show the coefficients for the off-diagonal diffusion coefficients. Source: From [337].

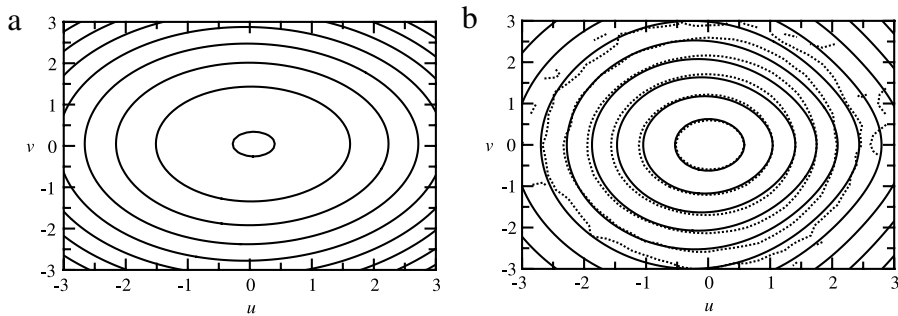


Fig. 52. Solution of the Fokker–Planck equation. (a) Contour plot of the initial condition in logarithmic scale. The simulation starts at the integral length $r = L$ with a Gaussian distribution fitted to the data. (b) The contour plots in logarithm scale of the simulated probability distribution on the scale $r = 2\lambda$. The distance between the contour lines is chosen in logarithmic scale and correspond to a factor 10. Dashed lines are the probability calculated directly from data, the full lines are the simulation ones. The simulation reproduces well the properties of the data. Source: From [337].

largest to smallest scales) is related to the (turbulent) Reynolds number. At high Reynolds numbers, it has been hypothesized that the cascade may be long enough for the smallest scales to “forget” the initial, large scales. Consequently, small-scale turbulence may adopt a universal structure. In addition, should the Reynolds number be high enough for there to be a distinct

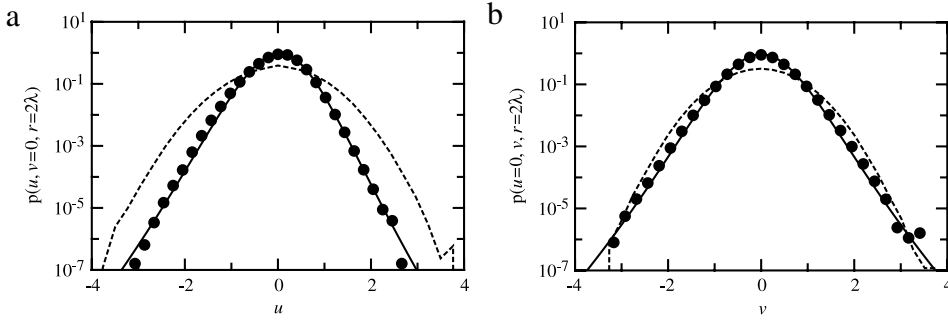


Fig. 53. Cuts through the probability distributions shown in Fig. 52. Black circles are the PDFs of the data, the straight line is the simulation and the dashed line the initial condition at $r = L$. (a) The distribution and its dependence on u for $v = 0$. (b) The distribution and its dependence on v for $u = 0$. Notice that the skewness in (a) and the intermittency for both components are well reproduced.
Source: From [337].

separation of scales between the large and small (dissipative) eddies, a range of scales that is independent of (i) the largest scales, and (ii) the smallest scales (and, therefore, viscosity) may exist. Such a range is called the inertial subrange.

Kolmogorov predicted the inertial-range scaling behavior of the n th-order structure function to be:

$$\langle (u_r)^n \rangle = f(\epsilon, r) \propto r^{\zeta_n}, \tag{6.13}$$

where, from dimensional considerations,

$$\zeta_n = n/3. \tag{6.14}$$

ϵ is the dissipation rate of turbulent kinetic energy (which, in the inertial subrange, is equal to the spectral energy transfer rate) and is equal to $2\nu \langle s_{ij}s_{ij} \rangle$. $s_{ij} \equiv \frac{1}{2}(\partial u_i/\partial x_j + \partial u_j/\partial x_i)$ is the turbulent strain rate. It has been subsequently shown that Eq. (6.14) does not agree with observations of turbulence, and that the deviation increases with the structure function order, n [342,300,343,55,340,344,314]. As mentioned before, the difference is attributed to the large variations in space and time of ϵ , a phenomenon called internal intermittency. As a result, the PDFs of u_r cannot be collapsed for different r and the observed variation of ζ_n with n becomes nonlinear. The relationship between ζ_n and n has been the focus of much study, of which reviews are given by [55,314].

Analogous results have been obtained for passive scalar fields, whose structure functions are given by:

$$\langle (\Delta\theta(r_j))^n \rangle = \langle [\theta(x_j + r_j) - \theta(x_j)]^n \rangle, \tag{6.15}$$

where θ is a turbulent scalar fluctuation, and r_j a separation. Obukhov [346] and Corrsin [347] extended the notions of Kolmogorov and predicted the inertial-range scaling behavior of the n th-order structure function of a passive scalar to be:

$$\langle \delta^n \rangle = f(\epsilon, \epsilon_\theta, r) \propto r^{\xi_n}, \tag{6.16}$$

where $\delta = \Delta\theta(r)$ and from dimensional considerations,

$$\xi_n = n/3. \tag{6.17}$$

Here, $\epsilon_\theta \equiv 2\alpha \langle (\partial\theta/\partial x_i)^2 \rangle$ is the rate at which scalar variance is ‘smeared’ by molecular processes, and is also known as the scalar dissipation rate. (The latter term is technically inaccurate, given that scalar variance is not dissipated, unlike the kinetic energy.) Eq. (6.17) does not agree with observations of turbulence [348–350,345,351,352], similar to the velocity field. The deviations from Eq. (6.17) also increase with the order n and are more significant than those observed for the velocity field. This is attributed to the internal intermittency of the scalar field, which is stronger than that observed for the velocity field; see [351,352] for recent reviews of turbulent passive scalars.

An alternative to studying the moments of the increments of turbulent quantities is to study their PDFs (which can subsequently be used to calculate the structure functions). Examples of such work include that of Castaing et al. [140] and Yaghoti [353] for the velocity field and Castaing [141], and [354–356] for the passive scalar field. To further our understanding of turbulence, the mathematics of Markov processes has been employed in studies of the PDFs of velocity differences for various separations. The applicability of Markov processes to experimental investigations of the PDFs of u_r was investigated by [10,12].

The principal objective of this part of the review is to present the Markov properties of passive scalar increments produced by a mean temperature gradient in grid-generated turbulence. In addition, the Reynolds number dependence of the Markov properties of the scalar fields will be examined over the range $140 \leq R_\lambda \leq 582$.

Results of Markovian analysis:

In [38] the details of experimental setup is given (see also Table 2). Here, the Markov properties of passive scalar increments will be studied and compared with those of the velocity field. Analogously, scalar increments are non-dimensionalized by $\sigma_{L\theta} = \sqrt{2\langle \theta^2 \rangle}$ —the square root of the large-scale limit of the second-order temperature structure

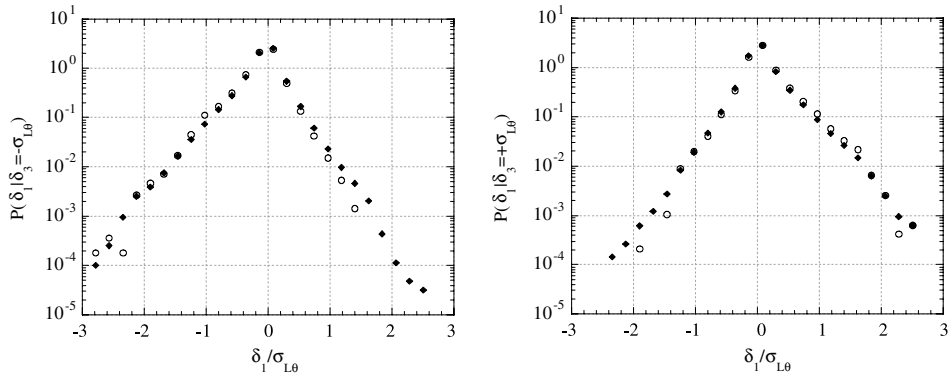


Fig. 54. Verification of the Chapman–Kolmogorov equation for temperature increments with $\delta_3 = -\sigma_{L\theta}$ and $\delta_3 = +\sigma_{L\theta}$. Solid diamonds represent $\int_{-\infty}^{\infty} p(\delta_1, r_1|\delta_2, r_2)p(\delta_2, r_2|\delta_3, r_3)d\delta_2$ and open circles represent $p(\delta_1, r_1|\delta_3, r_3)$. $r_1 = \lambda_\theta$, $r_2 = \ell_\theta/2$ and $r_3 = \ell_\theta$. $R_\lambda = 582$. Source: From [38].

Table 2

Flow Parameters. See [345] for further information on their calculation.

Source: From [38].

R_λ	140	306	582
$\langle U \rangle$ (m/s)	3.3	3.3	7.0
Active grid mode	Synchronous	Random	Random
x/M	62	62	62
dT/dy (K/m)	2.5	2.7	3.6
$\langle u^2 \rangle$ (m^2/s^2)	0.0290	0.0911	0.583
$\langle v^2 \rangle$ (m^2/s^2)	0.0209	0.0594	0.424
$\langle \theta^2 \rangle$ (K^2)	0.176	0.800	1.07
ϵ (m^2/s^3)	0.0418	0.0833	0.940
ϵ_θ (K^2/s)	0.277	0.799	1.74
ℓ (m)	0.11	0.30	0.43
ℓ_θ (m)	0.17	0.33	0.29
λ (m)	0.013	0.016	0.012
η (mm)	0.55	0.47	0.26

function. Most results will be presented for the highest Reynolds number ($R_\lambda = 582$). Unless otherwise specified, the results for the lower Reynolds numbers should be assumed to be consistent with those at $R_\lambda = 582$.

Similarly to the velocity field [10], one now test, (i) the Chapman–Kolmogorov equation for passive scalar increments, and (ii) the Markovian nature of the passive scalar increments. The Chapman–Kolmogorov equation is tested for $r_1 = \lambda_\theta$, $r_2 = \ell_\theta/2$, and $r_3 = \ell_\theta$. Contour plots of the conditional PDFs of scalar increments were similar to those for the velocity field and are, therefore, not reproduced here in the interest of brevity. Cross-sections of the contour plot for fixed δ_3 are shown in Fig. 54. From these figures, the agreement between $p(\delta_3, r_3|\delta_1, r_1)$ and $\int_{-\infty}^{\infty} p(\delta_3, r_3|\delta_2, r_2)p(\delta_2, r_2|\delta_1, r_1)d\delta_2$ is found to be good. The Markovian nature of the passive scalar increments is tested by means of Chapman–Kolmogorov equation in Fig. 55. For the given scales under consideration, there is a reasonable agreement between $(\delta_1, r_1|\delta_2, r_2)$ and $(\delta_1, r_1|\delta_2, r_2; \delta_3 = 0, r_3)$.

For smaller separations (i.e., $r_1 = \ell_\theta/2 - \lambda_\theta/4$, $r_2 = \ell_\theta/2$, and $r_3 = \ell_\theta/2 + \lambda_\theta/4$) the same two tests are performed. The Chapman–Kolmogorov equation is tested in Fig. 56 and the Markov nature of the passive scalar increments tested by means of the CK equation in Fig. 57. Similar to the velocity field, at the smaller scales, one observes that the Chapman–Kolmogorov equation continues to hold, though the passive scalar increments lose the Markovian property.

For large-scale separations, the passive scalar increments exhibit Markovian properties. For smaller separations, such properties disappear. This can alternatively be observed in Fig. 58, where the PDFs of the conditional scalar increments, denoted by x_θ and y_θ , are compared for several separations Δr .

Lastly, it is worth remarking on the different shapes of the PDFs of the passive scalar increment. Compared to the PDFs of velocity increments, the passive scalar increment PDFs are more pointy and possess broader tails. This is a characteristic of the higher level of internal intermittency of a turbulent passive scalar field when compared to the velocity field [351].

It is now of interest to (i) calculate the Kramers–Moyal coefficients for the passive scalar increments, and (ii) evaluate their relative magnitudes to determine the accuracy of modeling the PDF of the scalar increments with a Fokker–Planck equation. As was done for the velocity field, the conditional moments of the passive scalar increments, $M_k(\delta, r, \Delta r)$, are calculated. Typical results for $r = \ell_\theta/2$ and $\Delta r = \lambda_\theta$ are shown in Fig. 59. Polynomial fits of the following form are applied

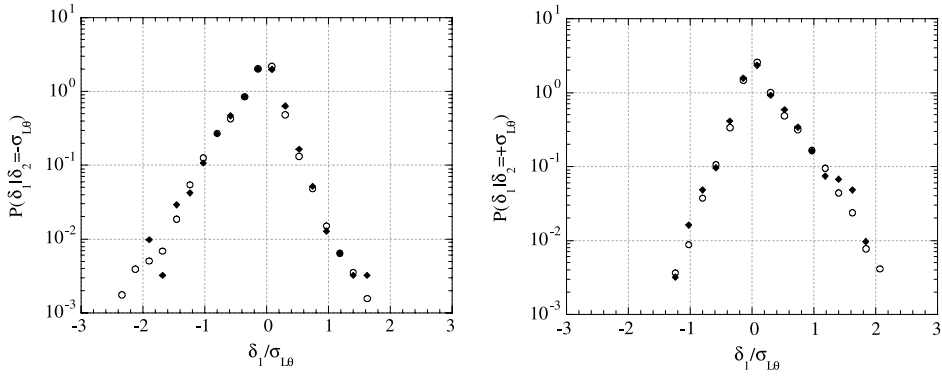


Fig. 55. Verification of the Markovian nature of the temperature increments by a comparison of the conditional PDFs in CK equation with $\delta_2 = -\sigma_{L\theta}$ and $\delta_2 = +\sigma_{L\theta}$. Solid diamonds represent $p(\delta_1, r_1|\delta_2, r_2; \delta_3 = 0, r_3)$, and open circles represent $(\delta_1, r_1|\delta_2, r_2)$. $r_1 = \lambda_\theta, r_2 = \ell_\theta/2$, and $r_3 = \ell_\theta$. $R_\lambda = 582$. Source: From [38].

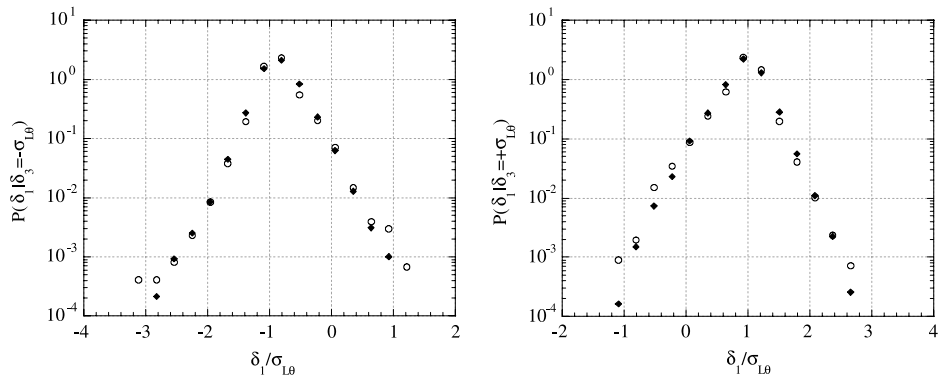


Fig. 56. Verification of the Chapman–Kolmogorov equation for temperature increments measured with a smaller separation of the scales for $\delta_3 = -\sigma_{L\theta}$ and $\delta_3 = +\sigma_{L\theta}$. Solid diamonds represent $\int_{-\infty}^{\infty} (\delta_1, r_1|\delta_2, r_2)(\delta_2, r_2|\delta_3, r_3)d\delta_2$, and open circles represent $(\delta_1, r_1|\delta_3, r_3)$. $r_1 = \ell_\theta/2 - \lambda_\theta/4, r_2 = \ell_\theta/2$, and $r_3 = \ell_\theta/2 + \lambda_\theta/4$. $R_\lambda = 582$. Source: From [38].

to first four conditional moments:

$$M_1 = O_1(r, \Delta r) - G_1(r, \Delta r)\delta + K_1(r, \Delta r)\delta^2 - E_1(r, \Delta r)\delta^3 \tag{6.18}$$

$$M_2 = A_2(r, \Delta r) + X_2(r, \Delta r)\delta + B_2(r, \Delta r)\delta^2 + Z_2(r, \Delta r)\delta^3 + W_2(r, \Delta r)\delta^4 \tag{6.19}$$

$$M_3 = O_3(r, \Delta r) - G_3(r, \Delta r)\delta + K_3(r, \Delta r)\delta^2 - E_3(r, \Delta r)\delta^3 \tag{6.20}$$

$$M_4 = A_4(r, \Delta r) + X_4(r, \Delta r)\delta + B_4(r, \Delta r)\delta^2 + Z_4(r, \Delta r)\delta^3 + W_4(r, \Delta r)\delta^4. \tag{6.21}$$

At first and third orders, the form of the curve fits are identical to those used for the velocity field. However, at second and fourth order, the order of the polynomials has been increased from 2 to 4, given the results in Fig. 59, which suggests that a polynomial of order greater than two is required.

The Kramers–Moyal coefficients, $D_k(\delta, r)$, are calculated as before – by extrapolating the values of $M_k(\delta, r, \Delta r)$ to $\Delta r = 0$, using only data for values of Δr for which the passive scalar field exhibits Markovian properties (i.e., $\Delta r \geq 0.5\lambda$). They take the following form [38]:

$$D_1(\delta, r) = o_1(r) - \gamma_1(r)\delta + \kappa_1(r)\delta^2 - \epsilon_1(r)\delta^3 \tag{6.22}$$

$$D_2(\delta, r) = \alpha_2(r) + \xi_2(r)\delta + \beta_2(r)\delta^2 + \zeta_2(r)\delta^3 + \omega_2(r)\delta^4 \tag{6.23}$$

$$D_3(\delta, r) = o_3(r) - \gamma_3(r)\delta + \kappa_3(r)\delta^2 - \epsilon_3(r)\delta^3 \tag{6.24}$$

$$D_4(\delta, r) = \alpha_4(r) + \xi_4(r)\delta + \beta_4(r)\delta^2 + \zeta_4(r)\delta^3 + \omega_4(r)\delta^4. \tag{6.25}$$

Subsequently studied was the behavior of turbulent passive scalar increments produced by the imposition of a mean temperature gradient upon grid-generated wind tunnel turbulence. Similarly to the velocity field, the passive scalar field (i) satisfied the Chapman–Kolmogorov equation for all scales studied herein, and (ii) satisfied for scales larger than the

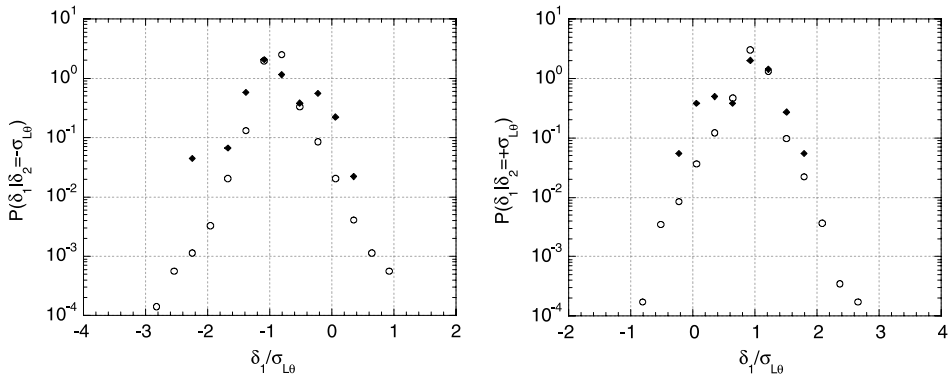


Fig. 57. Verification of the Markovian nature of the temperature increments by a comparison of the conditional PDFs in CK equation with a smaller separation of scales for $\delta_2 = -\sigma_{L\theta}$ and $\delta_2 = +\sigma_{L\theta}$. Solid diamonds represent $P(\delta_1, r_1 | \delta_2, r_2; \delta_3 = 0, r_3)$, and open circles represent $p(\delta_1, r_1 | \delta_2, r_2)$. $r_1 = \ell_\theta/2 - \lambda_\theta/4$, $r_2 = \ell_\theta/2$, and $r_3 = \ell_\theta/2 + \lambda_\theta/4$. $R_\lambda = 582$.
Source: From [38].

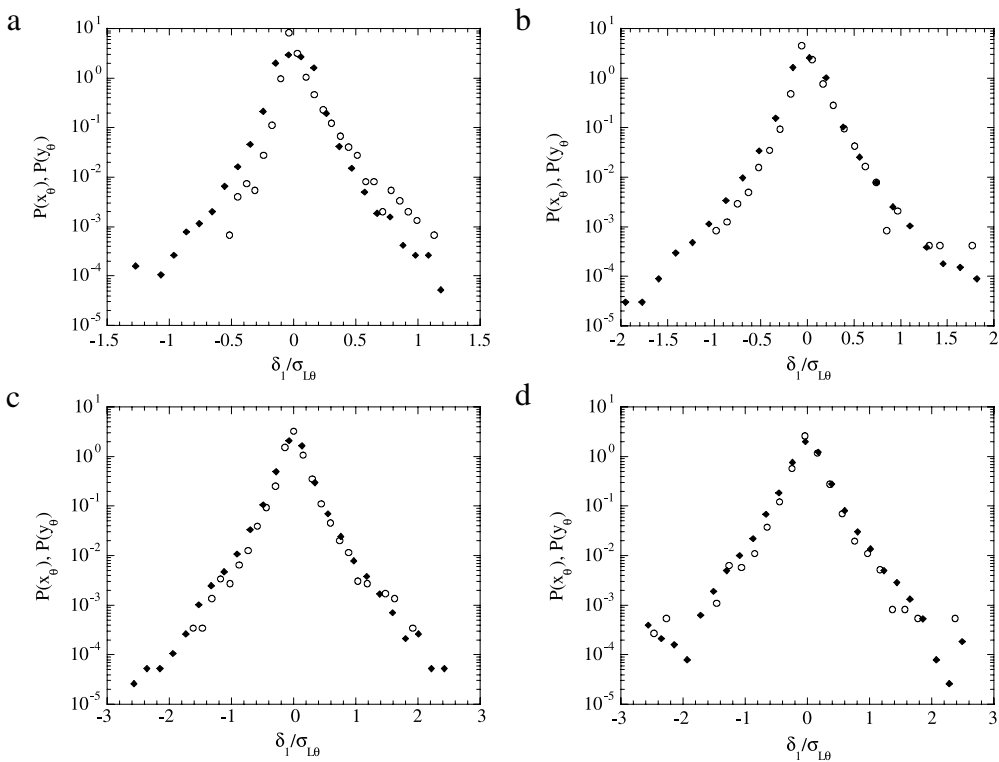


Fig. 58. Comparison of $p(x_\theta)$ (diamonds) and $p(y_\theta)$ (circles) for different scale separations. $r_2 = \ell_\theta/2$ for all cases. (a) $\Delta r = 0.1\lambda_\theta$, (b) $\Delta r = 0.2\lambda_\theta$, (c) $\Delta r = 0.5\lambda_\theta$, and (d) $\Delta r = 1.0\lambda_\theta$. $R_\lambda = 582$.
Source: From [38].

Taylor microscale. However, in contrast with the velocity field, it was found that the fourth-order term in the Kramers–Moyal expansion governing passive scalar increments was notably more significant. Consequently, all terms in the expansion must be retained and the PDFs of passive scalar increments cannot be modeled by a Fokker–Planck equation (see also [332,333]). A truncation of the Kramers–Moyal expansion at finite order would lead to nonrealizable PDFs, due to emergence of regions where the pdf is negative.

6.3. Econophysics: financial data in scale and the measurement noise

The econophysics focusses on the statistical properties of financial time series, such as stock prices, stock market indices or currency exchange rates. In particular, the mechanism leading to the fat-tailed probability distributions of fluctuations

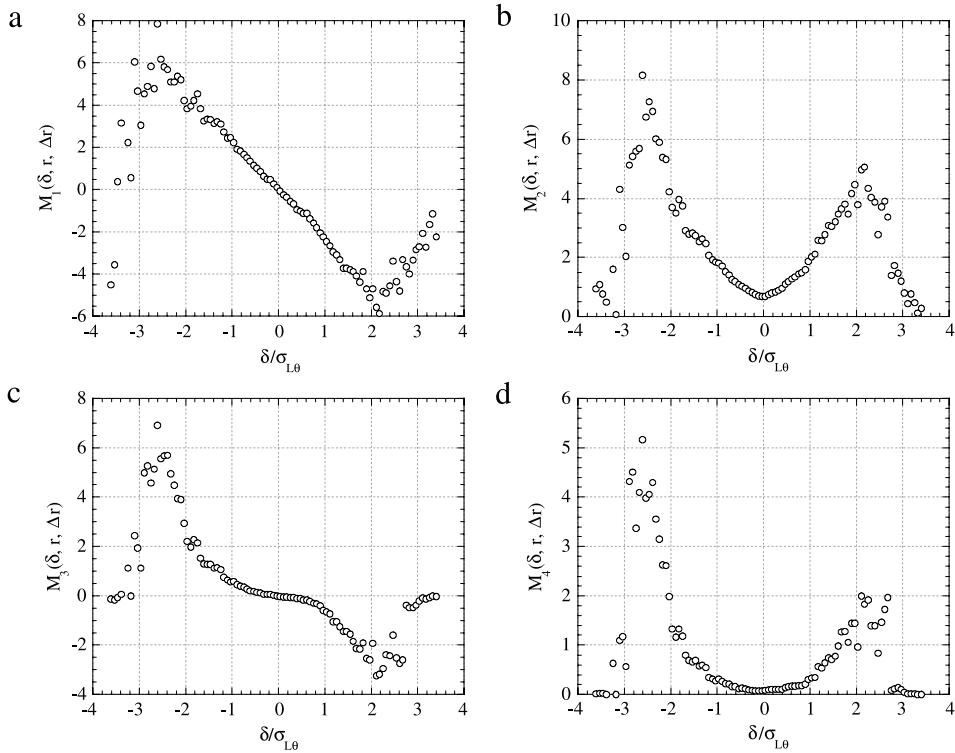


Fig. 59. Conditional moments of temperature increments. (a) $M_1(\delta, r, \Delta r)$, (b) $M_2(\delta, r, \Delta r)$, (c) $M_3(\delta, r, \Delta r)$, and (d) $M_4(\delta, r, \Delta r)$. $r = \ell_\theta/2$ and $\Delta r = \lambda_\theta$. $R_\lambda = 582$.

Source: From [38].

on small time scales is still unknown. Compared to a Gaussian, the PDFs of those fluctuations express an unexpected high probability for large fluctuations.

Fluctuations of financial time series $y(t)$ are usually measured by means of returns, log-returns or, equivalently, by price increments. Here, let us consider the statistics of the price increment $x(\tau)$ over a certain time scale τ , which is defined as:

$$x(\tau) = y(t + \tau) - y(t). \tag{6.26}$$

We suppressed dependence of the price increment $x(\tau)$ on the time t since we assume the underlying stochastic process to be stationary.

Here, we review the application of the Markov method in scale for financial time series [39,40] and discuss how the existence of a Markov process can be checked empirically, and how the Fokker–Planck equation can be constructed directly from the data. Furthermore, it has been shown that how multiplicative and additive noise sources interact, leading to the leptokurtic distributions and volatility clustering of the exchange rates. Friedrich et al. [39] considered in detail a data set containing 10^6 samples of the DM / US Dollar exchange rate from the one-year period October '92 to September '93.

The hypothesis concerning the Markovian properties of exchange rate data immediately fixes a framework for the analysis of the data. First, one has to give evidence of the Markovian properties according to Chapman–Kolmogorov equation. Secondly, the evolution of conditional probability densities $p(x_1, \tau_1 | x_2, \tau_2)$ has to be specified on the basis of the Fokker–Planck equation. Indeed one has to determine the conditional moments $M_k(x, \tau, \Delta\tau)$ at different scales τ for various values of $\Delta\tau$.

Practically, it is only possible to evaluate the lowest-order coefficients. Therefore, let us restrict our analysis to the coefficients of order one, two, and four. Approximating the limit $\Delta\tau \rightarrow 0$, we obtain the Kramers–Moyal coefficients $D_k(x, \tau)$. For the rest of the section, prices and price increments are given in units of the standard deviation σ of $y(t)$. For the data set under consideration, σ is 0.064 DM.

From the frequency spectrum (Fig. 60) of the exchange rate $y(t)$, it becomes evident that the data are dominated by white noise for high frequencies (above $\approx 10^{-2}$ Hz), comparable to the noise affecting any physical measurement. The original signal $y(t)$ seems to be the sum of the underlying “real” signal $s(t)$ and some additive white noise $n(t)$:

$$y(t) = s(t) + n(t). \tag{6.27}$$

The additive noise acts on the increments in a similar way. Note that this noise differs from the dynamical noise of the Langevin equation. $n(t)$ can be regarded as some randomness which is added separately to the dynamical stochastic cascade process. In physics this kind of noise is known as measurement noise [80,81]. We should mention that the discussed problem

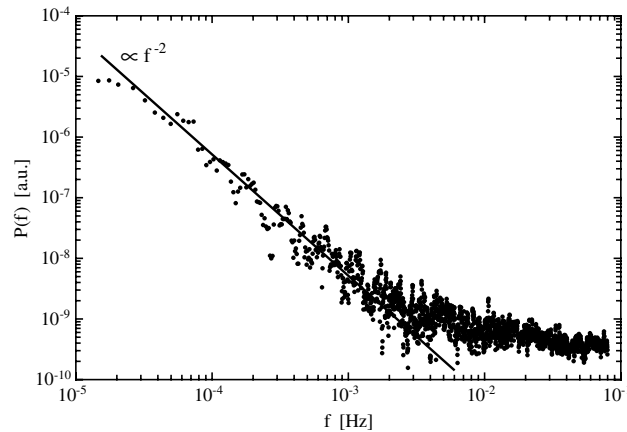


Fig. 60. Frequency spectrum of the exchange rate data $y(t)$. For high frequencies the data are dominated by white noise. Source: From [40].

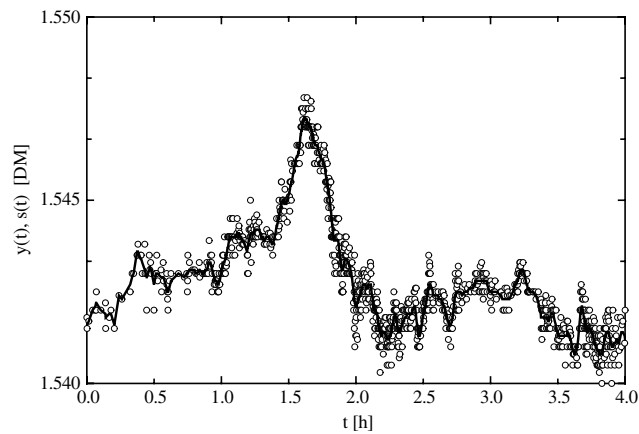


Fig. 61. Samples of the time series of the original exchange rate data $y(t)$ (circles) and the smoothed signal $s(t)$ (full line). Source: From [40].

of measurement noise is closely linked to the so-called Epps effect of financial data describing the decrease of correlations toward smaller return intervals [82].

The existence of such an additive white noise dominating the small scales causes problems in the analysis, especially in the limit $\Delta\tau \rightarrow 0$ which has to be performed according to Eqs. (2.40) and (2.41). In order to avoid these problems, one can apply a low-pass filter to the data. Each value $y(t)$ was replaced by the weighted average of itself and its neighboring data points, where the weighting function was chosen to be a Gaussian centered at t with a width of 44 s. Fig. 61 shows the result $s(t)$ of this procedure in comparison to the original data $y(t)$.

According to Eq. (6.27), one can extract the noise $n(t)$ by subtracting the smoothed signal from the original data $y(t)$. If the assumptions leading to Eq. (6.27) are correct and the algorithm used to smooth the data is an appropriate one, the extracted $n(t)$ should be white noise, i.e. it should be δ -correlated with zero mean.

The ratio of the mean value $\langle n(t) \rangle$ to the standard deviation σ_n of $n(t)$ was found to be smaller than $8 \cdot 10^{-5}$ ($\sigma_n = 0.0003$ DM). This result justifies the assumption of a zero mean for $n(t)$. The autocorrelation function $R_n(\tau)$ of $n(t)$ decreases from 1 to 0.08 within two seconds (see Fig. 62). Compared to the temporal resolution of the data (the smallest time step between two subsequent data points is 2 s), $R(\tau)$ indeed decreases rapidly. However, there appear to be small but significantly nonzero values for time delays $\tau \leq 2$ min, indicating that the approximation of the “real” signal $s(t)$ by the smoothed signal is insufficient. We, therefore, restrict our analysis to time delays τ larger than a certain elementary step τ_{\min} which, from Fig. 62, we chose to be 4 min. In units of τ_{\min} , $R_n(\tau)$ can be considered to be δ -correlated.

Fig. 63 compares the probability density functions of price increments $\chi(\tau)$ calculated from the original data $y(t)$ and the smoothed data $s(t)$. It becomes evident that the influence of the noise $n(t)$ is indeed restricted to small scales. For scales larger than $\tau = 2\tau_{\min}$ the PDFs are practically identical, see also [29].

For the rest of this section, the price increments $x_i(\tau_i)$ are (unless it is mentioned explicitly) calculated from the smoothed data $s(t)$.

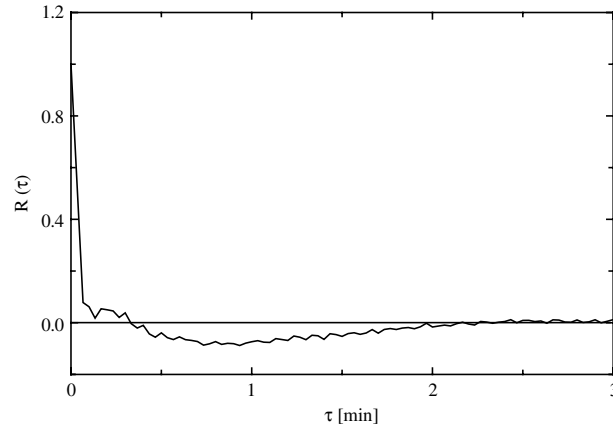


Fig. 62. The autocorrelation function of the extracted additive noise $n(t)$.
Source: From [40].

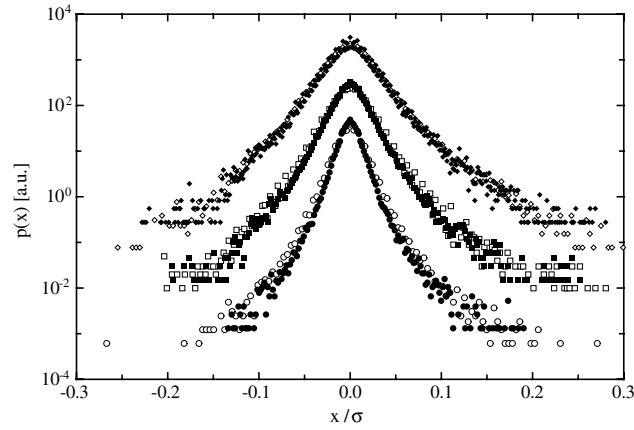


Fig. 63. PDFs of price increments $x(\tau)$ for $\tau = 4, 8,$ and 15 min (from bottom to top). The PDFs of x were calculated from the smoothed data (full symbols) as well as from the original time series $y(t)$ (open symbols). Curves have been shifted in y -direction for clarity of presentation. Note that σ is not the respective standard deviation of each individual PDF, but the standard deviation of the whole data set $y(t)$.
Source: From [40].

6.3.1. Markov properties

Now, let us present evidence that the Markovian property holds. The data set considered here consists of 10^6 data points, allowing us to verify the condition (2.25) for $N = 3$:

$$p(x_1, \tau_1 | x_2, \tau_2; x_3, \tau_3) = p(x_1, \tau_1 | x_2, \tau_2). \tag{6.28}$$

In Fig. 64, the contour plots of $p(x_1, \tau_1 | x_2, \tau_2)$ and $p(x_1, \tau_1 | x_2, \tau_2; x_3 = 0, \tau_3)$ have been superposed for the scales $\tau_1 = \tau_{\min} = 4$ min, $\tau_2 = 2\tau_{\min}$ and $\tau_3 = 3\tau_{\min}$. The proximity of corresponding contour lines yields evidence for the validity of Eq. (6.28) for the chosen set of scales. Additionally, two cuts through the conditional probability densities are provided for fixed values of x_2 .

Fig. 65 shows the same plots for a different set of scales: $\tau_1 = 1$ h, $\tau_2 = \tau_1 + \tau_{\min}$ and $\tau_3 = \tau_1 + 2\tau_{\min}$. Again, one finds a good agreement between corresponding contour lines.

Similar results were obtained for several other sets of scales chosen from the interval $\tau_{\min} \leq \tau_1 \leq 2h$, with $\Delta\tau = \tau_2 - \tau_1 = \tau_3 - \tau_2$ ranging from τ_{\min} to $3\tau_{\min}$. Based on these result, one concludes that the price increments of exchange rate data obey a Markov process for the range of scales under consideration, i.e. for scales and differences of scales larger than τ_{\min} .

6.3.2. Kramers–Moyal coefficients

According to Eqs. (2.40) and (2.41), the coefficients $M_k(x, \tau, \Delta\tau)$ can be calculated from the joint probability density functions. These joint PDFs $p(\tilde{x}, \tau - \Delta\tau, x, \tau)$ are easily obtained from the data by counting the number $N(\tilde{x}, x)$ of occurrences of the two increments \tilde{x} and x . Then the limit $\Delta\tau \rightarrow 0$ has to be performed next in order to obtain the Kramers–Moyal coefficients. Fig. 66 shows the coefficient $M_2(x, \tau, \Delta\tau)$ for exemplarily chosen fixed values of x and τ as a function of $\Delta\tau$.

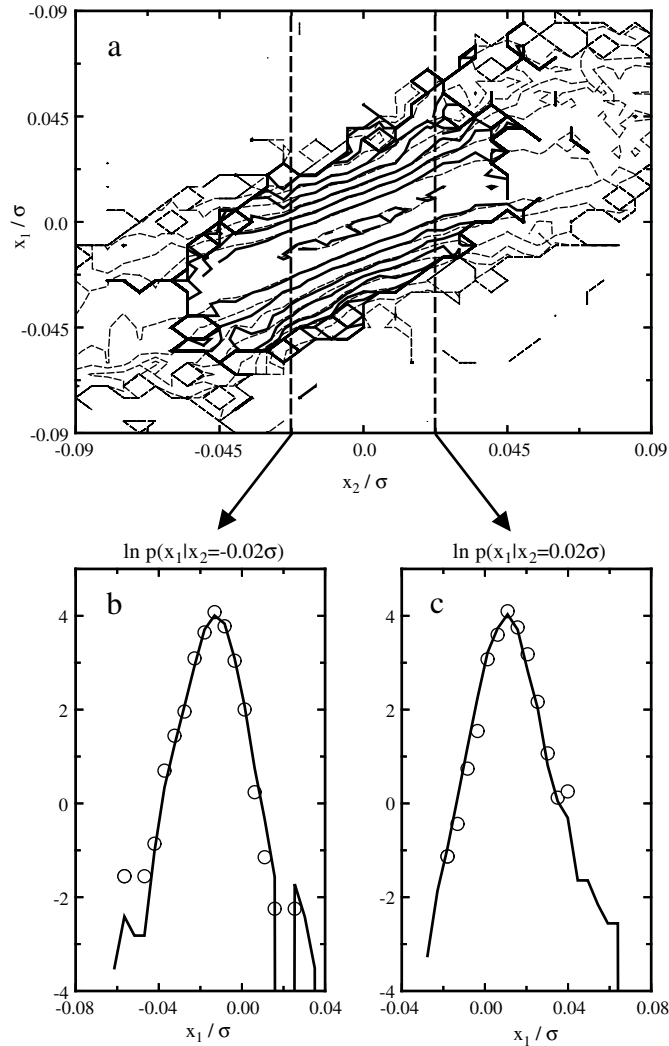


Fig. 64. (a) Contour plots of the conditional PDFs $p(x_1, \tau_1 | x_2, \tau_2)$ (dashed lines) and $p(x_1, \tau_1 | x_2, \tau_2; x_3 = 0, \tau_3)$ (solid lines) for $\tau_1 = \tau_{\min}$, $\tau_2 = 2\tau_{\min}$ and $\tau_3 = 3\tau_{\min}$. (b) and (c) cuts through the conditional PDFs for $x_2 = \pm 0.02\sigma$. Open symbols: $p(x_1, \tau_1 | x_2, \tau_2; x_3 = 0, \tau_3)$, solid lines: $p(x_1, \tau_1 | x_2, \tau_2)$. Source: From [39].

Throughout the interval $\tau_{\min} \leq \Delta\tau \leq 3\tau_{\min}$, the dependence of M_2 on $\Delta\tau$ turns out to be linear. For values of $\tau < \tau_{\min}/2$, the values deviate from that linear behavior. It is interesting to note that the range of scales where those deviations begin is identical with the range of scales for which the autocorrelation function of the reconstructed additive noise $n(t)$ has nonzero values (see Fig. 62). The limit $\Delta\tau \rightarrow 0$ is therefore performed by fitting a straight line to the M_n in the interval $\tau_{\min} \leq \Delta\tau \leq 2\tau_{\min}$, thus avoiding problems with the values for $\Delta\tau \leq \tau_{\min}/2$ (see Fig. 66).

Fig. 66 also displays the coefficient $M_2^{(y)}$, which is obtained when instead of the smoothed signal $s(t)$ the original data $y(t)$ is used to calculate the coefficients M_k . In the presence of additive white noise, the values of $M_2^{(y)}$ diverge as $\Delta\tau$ goes to zero. The limit $\Delta\tau \rightarrow 0$ cannot be performed in this case. Since the coefficients M_k are nothing but conditional moments of the increments, the reason for this behavior can easily be understood by expressing the second moment of the increment of $y(t)$ in terms of $s(t)$ and $n(t)$. Using Eq. (6.27), one obtains:

$$\begin{aligned} \langle (y(t+\tau) - y(t))^2 \rangle &= \langle (s(t+\tau) + n(t+\tau) - s(t) - n(t))^2 \rangle \\ &= \langle (s(t+\tau) - s(t))^2 \rangle + 2\langle n^2 \rangle. \end{aligned} \quad (6.29)$$

Due to the additive nature of the white noise n , the additional constant term $2\langle n^2 \rangle$ arises which does not depend on the scale τ . Similar terms also arise for the conditional moments M_k when $y(t)$ is used instead of $s(t)$. Dividing the conditional moments of the increment by $\Delta\tau$ according to Eqs. (2.40) and (2.41) thus leads to the diverging behavior of $M_k^{(y)}$ in the limit $\Delta\tau \rightarrow 0$ as shown in (Fig. 66) (see also [80]).

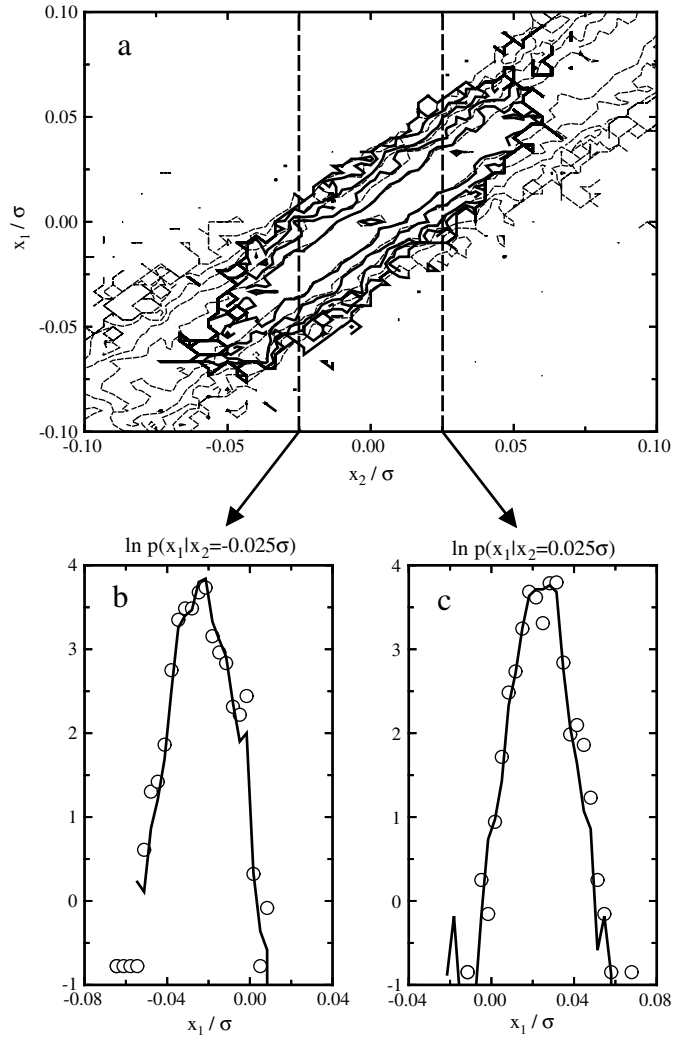


Fig. 65. (a) Contour plots of the conditional PDFs $p(x_1, \tau_1 | x_2, \tau_2)$ (dashed lines) and $p(x_1, \tau_1 | x_2, \tau_2; x_3 = 0, \tau_3)$ (solid lines) for $\tau_1 = 1$ h, $\tau_2 = \tau_1 + \tau_{\min}$ and $\tau_3 = \tau_1 + 2\tau_{\min}$. (b) and (c) cuts through the conditional PDFs for $x_2 = \pm 0.025\sigma$. Open symbols: $p(x_1, \tau_1 | x_2, \tau_2; x_3 = 0, \tau_3)$, solid lines: $p(x_1, \tau_1 | x_2, \tau_2)$. Source: From [40].

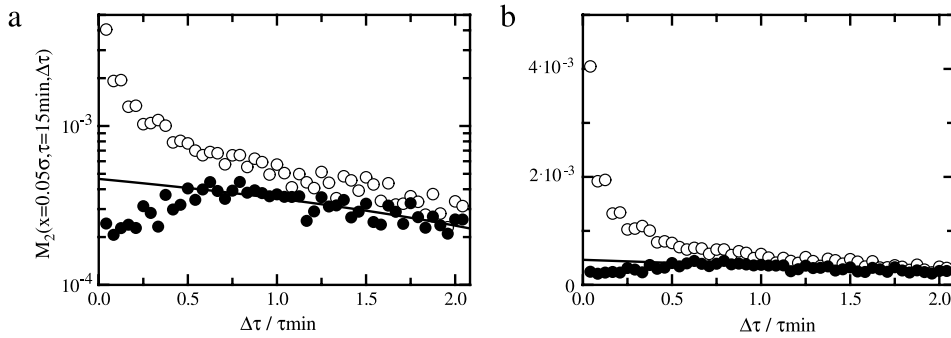


Fig. 66. The coefficient $M_2(x, \tau, \Delta\tau)$ as a function of $\Delta\tau$ for $x = 0.05\sigma$ and $\tau = 15$ min (full circles). (a) logarithmic scale, (b) linear scale. For $\tau \geq \tau_{\min}$, M_2 is a linear function of $\Delta\tau$ and can thus be extrapolated using a linear fit in the interval $\tau_{\min} \leq \Delta\tau \leq 2\tau_{\min}$ (full line). The open circles represent the results for M_2 for the same values of x and τ when instead of the smoothed data $s(t)$ the original data $y(t)$ are used. The presence of additive white noise leads to diverging values for $M_2^{(y)}$ as $\Delta\tau$ goes to zero. Source: From [40].

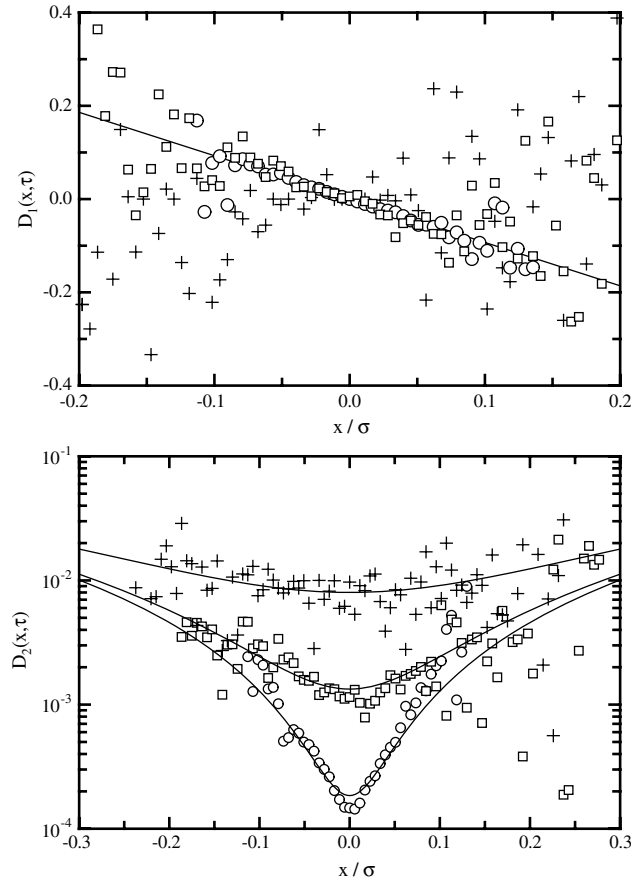


Fig. 67. The coefficients D_1 (a) and D_2 (b) as functions of the price increment x at scale $\tau = 15$ min (circles), $\tau = 2$ h (squares) and $\tau = 12$ h (crosses). The lines represent the results for D_1 and D_2 obtained with the method described in Section 2 (note the logarithmic presentation of D_2). Source: From [40].

When the smoothed signal $s(t)$ is used to calculate the coefficients M_k , the linear dependence of $M_k(x, \tau, \Delta\tau)$ on $\Delta\tau$ is found to hold for $k = 1$ and 2, several scales τ and all values of x . This enables us to calculate the coefficients $D^{(1)}(x, \tau)$ and $D^{(2)}(x, \tau)$ from the M_k using the method of linear extrapolation described above. Fig. 67 shows the results for $D^{(1)}$ and $D^{(2)}$ as a function of the price increment x at several scales τ . Both coefficients exhibit simple dependences on the price increment. While $D^{(1)}$ is linear in x , $D^{(2)}$ can be approximated by a polynomial of degree two where the linear term is zero:

$$\begin{aligned} D^{(1)}(x, \tau) &= -\gamma(\tau)x, \\ D^{(2)}(x, \tau) &= \alpha(\tau) + \beta(\tau)x^2. \end{aligned} \quad (6.30)$$

Eq. (6.30) turns out to describe the dependences of the coefficients $D^{(k)}$ on x for all scales τ up to two hours (see Fig. 67). For larger scales, the statistics of the data are too poor to allow for a proper calculation of the coefficients M_k , which results in considerable scatter of $D^{(1)}$ and $D^{(2)}$ (as exemplarily shown for $\tau = 12$ h in Fig. 67). Fitting the $D^{(k)}(x, \tau)$ by straight lines and parabolas, respectively, therefore yields values for $\gamma(\tau)$, $\alpha(\tau)$ and $\beta(\tau)$ which scatter considerably and which do not exhibit a well-defined functional dependence on the scale τ . However, what can be concluded from the analysis of the coefficients $D^{(k)}$ is that, the Kramers–Moyal coefficients are linear and quadratic functions of the price increment, respectively, with the coefficients depending on the scale τ . According to the Pawula theorem, it is of importance to estimate the fourth-order coefficient and to decide whether it may be neglected. Fig. 68 shows the coefficient for $M_4(x, \tau, \Delta\tau)$ for fixed values of x and τ as a function of $\Delta\tau$. Again, we find a linear dependence of the coefficient on $\Delta\tau$ for $\Delta\tau \geq \tau_{\min}$. But, whereas $M_2(\Delta\tau)$ increases as $\Delta\tau$ goes to zero, M_4 decreases. Furthermore, the linear extrapolation yields a value for D_4 which is small compared to the values of M_4 for $\tau_{\min} \leq \tau \leq 2\tau_{\min}$. This is a first hint that M_4 tends to zero in the limit $\Delta\tau \rightarrow 0$.

6.3.3. Consistency checks

The results and assumptions of the preceding sections lead to Fokker–Planck equations for the PDF $p(x, \tau)$ and the conditional PDF $p(x, \tau | x_0, \tau_0)$, respectively. The coefficients $D^{(1)}$ and $D^{(2)}$ which completely determine these equations

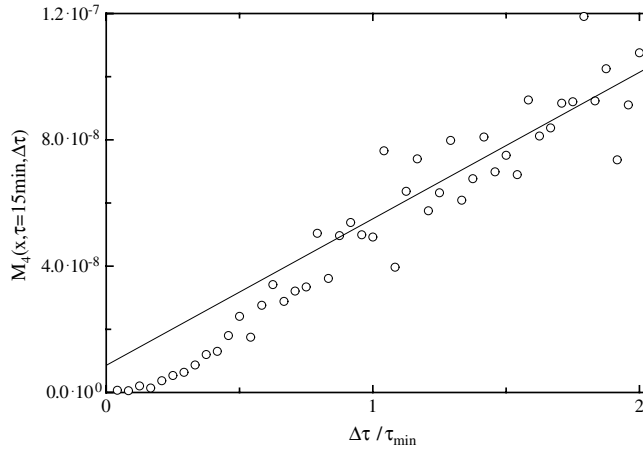


Fig. 68. The coefficient $M_4(x, \tau, \Delta\tau)$ as a function of $\Delta\tau$ for $x = -0.05\sigma$ and $\tau = 15$ min (circles).
Source: From [40].

were estimated from the data. In order to test this result, one can compare the (numerical) solution of the Fokker–Planck equation with the distributions obtained directly from the data. The algorithm used for the numerical iteration is based on the approximative solution of the Fokker–Planck equation for small steps $\Delta\tau$. According to [14], the conditional PDF $p(x_1, \tau_0 - \Delta\tau | x_0, \tau_0)$ is, for small $\Delta\tau$ and arbitrary $D^{(1)}$ and $D^{(2)}$, a Gaussian distribution in x_1 with mean value $x_0 - D^{(1)} \Delta\tau$ and standard deviation $\sqrt{2D^{(2)} \Delta\tau}$. In order to obtain the conditional densities for larger steps, we use the Chapman–Kolmogorov equation

$$p(x_2, \tau_0 - 2\Delta\tau | x_0, \tau_0) = \int_{-\infty}^{+\infty} p(x_2, \tau_0 - 2\Delta\tau | x_1, \tau_0 - \Delta\tau) p(x_1, \tau_0 - \Delta\tau | x_0, \tau_0) dx_1. \quad (6.31)$$

Eq. (6.31) is a direct consequence of the Markov condition. Iterating this procedure, we finally obtain the conditional PDF $p(x, \tau_0 - n\Delta\tau | x_0, \tau_0)$. Multiplying with $p(x_0, \tau_0)$ and integrating with respect to x_0 yields the PDF $p(x, \tau_0 - n\Delta\tau)$.

Fig. 69, which compares the solutions of the Fokker–Planck equation for the PDF $p(x, \tau)$ with the empirically estimated PDFs, proves that the Fokker–Planck equation accurately describes the evolution of $p(x, \tau)$ in τ over the range $4 \text{ min} \leq \tau \leq 12 \text{ h}$.

As mentioned above, the Fokker–Planck equation also governs the conditional PDF $p(x, \tau | x_0, \tau_0)$. As a further test of our results, we calculated the solutions of the Fokker–Planck equation. Fig. 70 shows the result for $\tau_0 = 1 \text{ h}$ and $\tau = 0.5 \text{ h}$, again in comparison with empirical data. Taking into account the various uncertainties and assumptions in the determination of the coefficients $D^{(1)}$ and $D^{(2)}$, the agreement between the solution of Fokker–Planck equation and the data is remarkably good.

The purpose of this section was to show how the mathematical framework of Markov processes can be applied to the analysis of empirical high frequency exchange rate data. Within the limitations due to the finite number of samples, one was able to verify the Markovian properties of the price increment for time delays τ larger than $\tau_{\min} = 4 \text{ min}$. Furthermore, one obtained estimates for the Kramers–Moyal coefficients $D^{(k)}(x, \tau)$ and found hints that the fourth-order coefficient $D^{(4)}$ is zero. The comparison of the solutions of the resulting Fokker–Planck equations with the empirical distributions strongly supports our results for $D^{(1)}$ and $D^{(2)}$ [39].

6.4. Seismic time series

There are many known precursors to impending earthquakes, ranging from peculiar behavior of animals, to thermal radiation from the earth. The challenge then is how to analyze seismic data in order to understand the precursors and their implications for an impending earthquake, which may then be used for developing and setting up new quantities as alerts for the earthquakes.

There are currently a large number of stations around the world that perform high quality measurements for seismic activities. Such data are usually viewed as examples of complex stochastic time series, and can be analyzed by various methods. Fig. 71 show the time series of earth velocity which is detected by broad-band station, and velocity in turbulent media. It is evident that both time series have very complex fluctuations and behavior.

Historically, understanding the phenomena that lead to large earthquakes entails having the ability to accurately analyze such time series and understanding their nature [357–360,53,54]. Several concepts and ideas have been advanced over the past decades to explain certain aspects of earthquakes and the associated seismic time series, like the Gutenberg–Richter [361] law for the number of earthquakes with a magnitude greater than a given value M , to the Omori

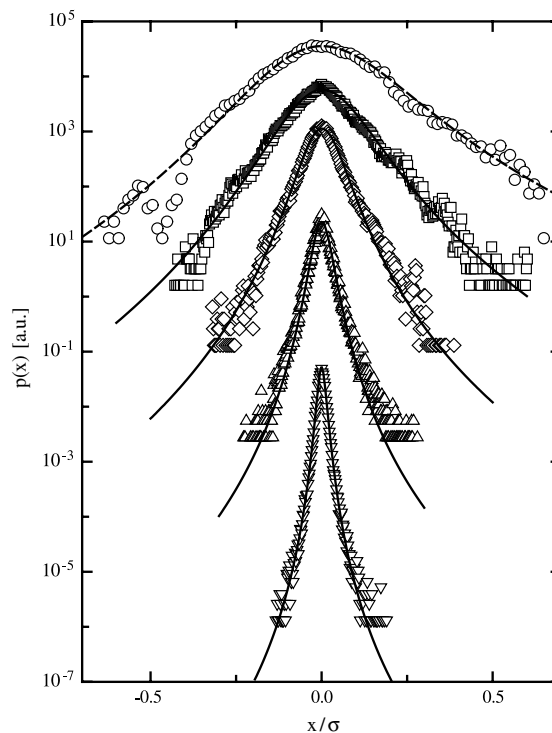


Fig. 69. Comparison of the numerical solutions of the Fokker–Planck equation (solid lines) for the PDFs $p(x, \tau)$ with the PDFs obtained directly from the data (open symbols). The scales τ are (from top to bottom): $\tau = 12$ h, 4 h, 1 h, and 15 and 4 min. The PDF at the largest scale $\tau = 12$ h was parametrized (dashed line) and used as initial condition for the iteration of the Fokker–Planck equation. Curves are shifted in vertical direction for clarity of presentation. Source: From [40].

law [362] for the distribution of the aftershocks, or the Bak–Tang concept of self-organized criticality [363]. Furthermore seismic data belong to the much larger class of stochastic time series, the analysis of which has been the subject of much research over the past years. In particular, there has been much recent interest in investigating the precursors to and the predictability of extreme increments in a time series [364,365].

Numerous papers have reported that large events are preceded by anomalous trends of seismic activity both in time and space. Several reports also indicate that seismic activity increases as an inverse power of the time to the main event (sometimes referred to as an inverse Omori law for relatively short time spans), while others document a quiescence, or even contest the existence of such anomalies at all [357,359,248]. If such anomalies can be analyzed and understood, then one might be able to forecast future large events.

There are two schools of thought on the length of the time period over which the anomalies occur and accumulate. One school believes that the anomalies occur within days to weeks before the main shock, but probably not much earlier [366,367], and that the spatial precursory patterns develop at short distances from impending large earthquakes. Proponents of this school look for the precursory patterns in the immediate vicinity of the main shock, i.e., within distances from the epicenter that are on the order of, or somewhat larger than, the length of the main shock rupture.

The second school believes that the anomalies may occur up to *decades* before large earthquakes, and at distances much larger than the length of the main shock rupture, a concept closely linked to the theory of critical phenomena [357,359,368] which was advocated [357,359,368] as early as 1964 with a report [358] on the pre-monitory increase in the total area of the ruptures in the earthquake sources in a medium magnitude range, documenting the existence of long-range correlations in the precursors (over 10 seismic source lengths) with worldwide similarity. More recently, Knopoff et al. [369] reported on the existence of long-range spatial correlations in the increase of medium-range magnitude seismicity prior to large earthquakes in California.

Sornette and Sornette [370] proposed an observable consequence of the critical point model of Allègre et al. [371] with the goal of verifying the proposed scaling laws of rupture. Almost simultaneously, but following apparently an independent line of thought, Voight [372,373] introduced the idea of a time-to-failure analysis in the form of an empirical second-order nonlinear differential equation, which for certain values of the parameters would lead to a time-to-failure power law, in the form of an inverse Omori law. This failure was used and tested later for predicting volcanic eruptions. Then, Sykes and Jaumé [374] performed the first empirical study to quantify with a specific law an acceleration of seismicity prior to large earthquakes. They used an exponential law to describe the acceleration, and did not use or discuss the concept of a critical earthquake. Bufo and Varnes [375] re-introduced a time-to-failure power law to model the observed accelerated seismicity

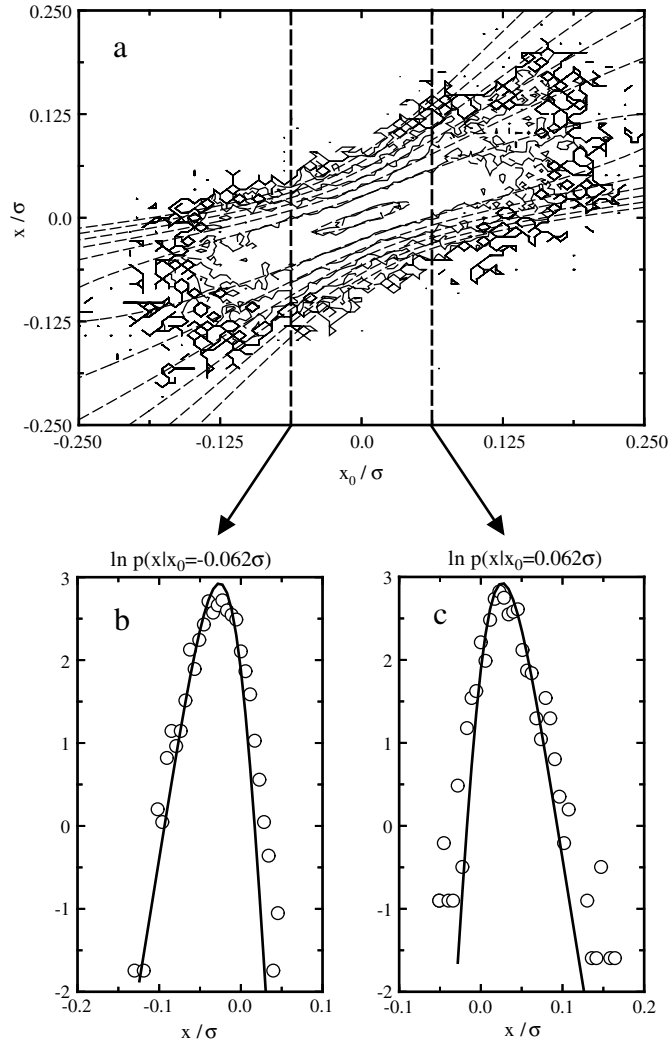


Fig. 70. Comparison of the numerical solution of the Fokker–Planck equation for the conditional PDF $p(x, \tau | x_0, \tau_0)$ with the empirical data. (a) Contour plots of $p(x, \tau | x_0, \tau_0)$ for $\tau_0 = 1$ h and $\tau = 0.5$ h. Dashed lines: numerical solution of Eq. (6.31), solid lines: empirical data. (b) and (c) Cuts through $p(x, \tau | x_0, \tau_0)$ for $x_0 = -0.062\sigma$ and $x_0 = +0.062\sigma$, respectively. Open symbols: empirical data, solid lines: numerical solution of the Fokker–Planck equation.

Source: From [40].

quantified by the so-called cumulative Benioff strain. Their justification of the power law was a mechanical model of material damage. They neither referred to nor discussed the concept of a critical earthquake.

Sornette and Sammis [227] were the first to reinterpret the work of Bufe and Varnes [375], and all the previous ones reporting accelerated seismicity, within a model in which the occurrence of large earthquakes is viewed as a critical point phenomenon in the sense of the statistical physics framework of critical phase transitions. Their model generalized significantly the previous works in that the proposed critical point theory did not rely on an irreversible fracture process, but invoked a more general *self-organization* of the stress field prior to large earthquakes. Moreover, using insights from the critical phenomena, Sornette and Sammis [227] generalized the power-law description of the accelerated seismicity by considering *complex* scaling exponents which result in *log-periodic* corrections to the scaling [227,376–378,225,379].

Such a generalized power law with log-periodic corrections was shown in [230] to describe the increase in the energy that rock releases as it undergoes fracturing. These ideas were further developed by Huang et al. [380]. Empirical evidence for these concepts was provided by Bowman et al., [381] who showed that large earthquakes in California with magnitudes larger than 6.5 are systematically preceded by a power-law acceleration of seismic activity in time over several decades, in a spatial domain about 10–20 times larger than the impending rupture length (i.e., of the order of a few hundred kilometers). The large event can, therefore, be viewed as a temporal singularity in the seismic history time series. Such a theoretical framework implies that a large event results from the collective behavior and accumulation of many previous smaller-sized events. Similar analysis was reported by Brehm and Braile [382] for other earthquakes.

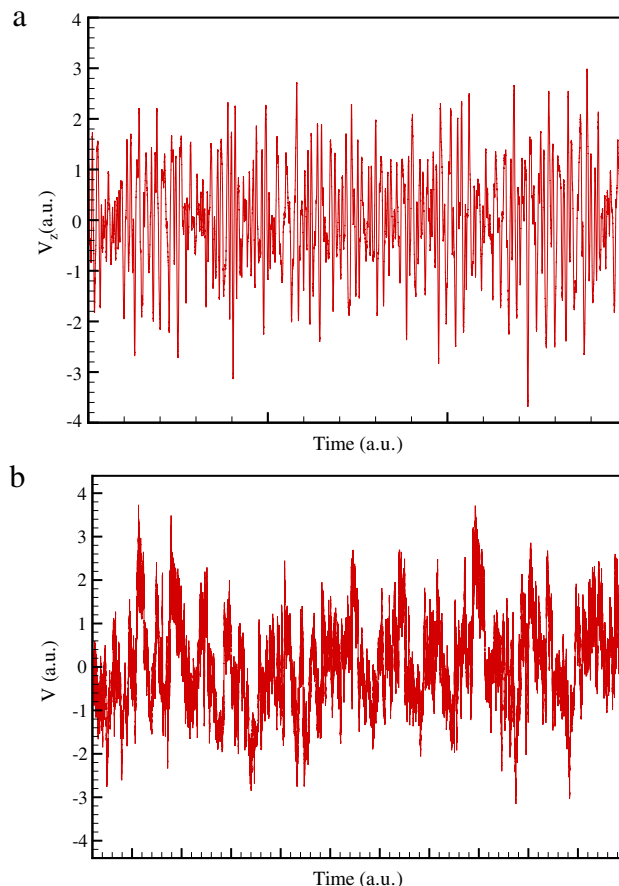


Fig. 71. (a) Time series of Earth velocity fluctuations and (b) velocity of turbulent fluid.

In the critical point approach to earthquakes, as the stress on rock increases, micro-ruptures develop that redistribute the stress and generate fluctuations in it. As damage accumulates, the fluctuations become spatially and temporally correlated, resulting in a larger number of significantly stressed large domains. The correlations accelerate the spatial smoothing of the fluctuations, culminating in a rupture with a size on the order of the system's size, and representing the final state in which earthquakes occur. Numerical and empirical evidence for this picture indicates that, similar to critical phenomena, the correlation length of the stress-field fluctuations increases significantly before a large earthquake. In this vein, Zoller and Hainzl [383–385], recently performed novel and systematic spatiotemporal tests of the critical point hypothesis for large earthquakes based on the quantification of the predictive power of both the predicted accelerating moment release and the growth of the spatial correlation length, hence providing fresh support to the concept.

Recently Manshour et al., [53,54] analyzed the fluctuations in the time series for the Earth vertical velocity and have found that far from an earthquake the fat tails of the non-Gaussian probability density function (PDF) of the detrended increments of the series exhibits a behavior which is reminiscent of the cascading process in hydrodynamic turbulence. As an earthquake is approached, the shape of the fat tails manifests significant changes, exhibiting a transition from the non-Gaussian PDF to a scale-invariant behavior. The transition to the scale-invariant behavior is characterized by the change in the Castaing parameter λ_s^2 , which is related to the diffusion coefficient $D^{(2)}$ (see Section 4), of the time series. The typical time scale over which the PDF undergoes the transition is of the order of 5–10 h before an earthquake. Thus, the phase transition may be used for risk analysis of impending earthquakes.

Let us begin with the time series for a large earthquake with magnitude $M = 7.1$, that had occurred on May 21, 2003, in Oran-Argel and detected in Ibiza (Balearic Islands – Spain). The data is divided into two parts: (i) data set (a) representing the background fluctuations far from the time of the earthquake, and (ii) data set (b) close (less than 5 h) to the earthquake.

The data are first detrended in order to remove the possible trends in the time series $x(t) \equiv V_z(t)$. To do so, $x(t)$ is divided into semi-overlapping subintervals $[1 + s(k - 1), s(k + 1)]$ of length $2s$ and labeled by $k \geq 1$. $x(t)$ is then fitted to a third-order polynomial to detrend the original series in the corresponding time window. The detrended increments on scale s are defined by $Z_s(t) = x^*(t + s) - x^*(t)$, where $t \in [1 + s(k - 1), sk]$, with $x^*(t)$ being the detrended series, i.e., the deviation of $x(t)$ from its fitted value.

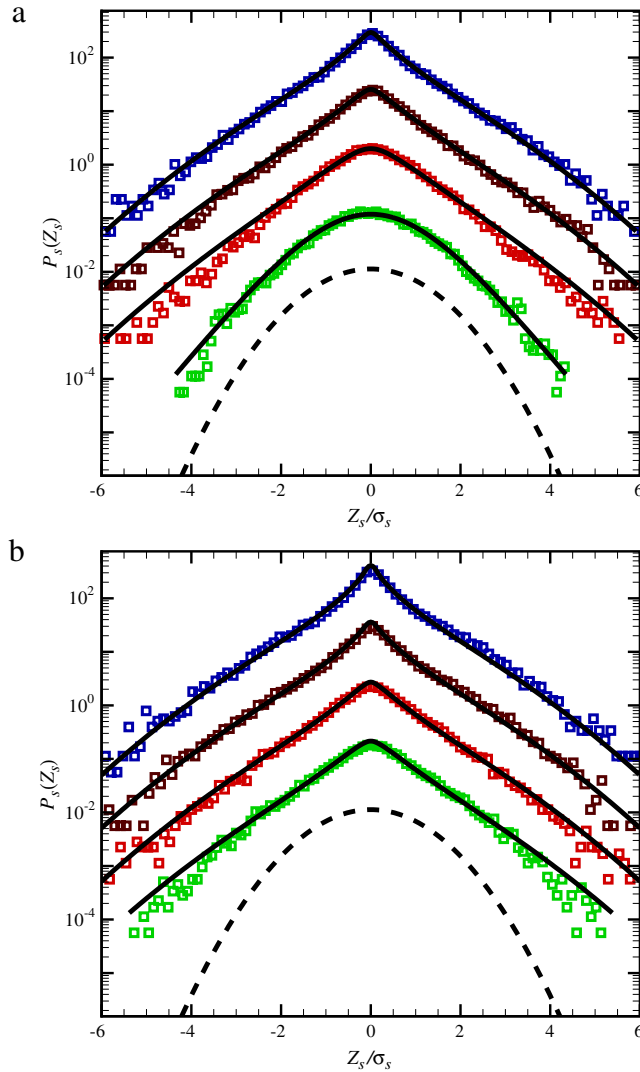


Fig. 72. Continuous deformation of the increments' PDFs for the $M = 7.1$ earthquake for, from top to bottom, $s = 200, 400, 600,$ and 800 ms, and (a) far from, and (b) close to, the earthquake. Solid curves are the PDFs based on Eq. (4.20), while dashed curves are the Gaussian PDF. Source: From [53].

To fit the increments' PDF to Eq. (4.20), one can estimate the variance $\lambda_s^2(s)$, using the least squares method, with the error bars estimated by the goodness of the fit method. Deviation of $\lambda_s^2(s)$ from zero is a possible indicator of non-Gaussian statistics. As shown in Fig. 72, one finds an accurate parametrization of the PDFs by $\lambda_s^2(s)$ for both data sets. Moreover, the PDF of Z_s for the data set (a) becomes essentially Gaussian as s increases to 800 ms, whereas it deviates from the Gaussian distribution for the data set (b).

The scale dependence of the parameter λ_s^2 of the PDF is shown in Fig. 73. For the data set (a) of the $M = 7.1$ earthquake, shown in Fig. 73(a), and times $200 \text{ ms} < s < 500 \text{ ms}$, a logarithmic decay, $\lambda_s^2 \propto \log s$, is obtained. For the data set (b), the logarithmic regime extends to $300 \text{ ms} < s < 2000 \text{ ms}$. Fig. 73(b) presents similar behavior for the $M = 6.1$ earthquake (the 2004, $M = 6.1$ event in Alhucemas–Spain). Moreover, the PDF of Z_s for the data set (a) becomes essentially Gaussian as s increases to 800 ms ($\lambda_s^2 \rightarrow 0$), whereas it deviates from the Gaussian distribution for the data set (II). The time scale $s = 800$ ms for λ_s^2 within a moving window was estimated by the plot of λ_s^2 vs. s for the data set (a) (background fluctuations), and selecting s such that $\lambda_s \rightarrow 0$.

The importance of the results shown in Fig. 73 is that, they indicate that the increments' PDFs for $s > 2000$ ms and $s > 1500$ ms are almost Gaussian ($\lambda_s^2 \rightarrow 0$) for the $M = 7.1$ and $M = 6.1$ earthquakes [for the data set (b)], respectively. Transforming the time scales to length scales via the velocity of the elastic waves in Earth, ~ 5000 m/s, the corresponding length scales are about 10 and 7.5 km, for the same earthquakes, respectively, implying that larger earthquakes have larger characteristic length scales, and that for the $M = 6.1$ event the active part in the fault is smaller. As one moves down the

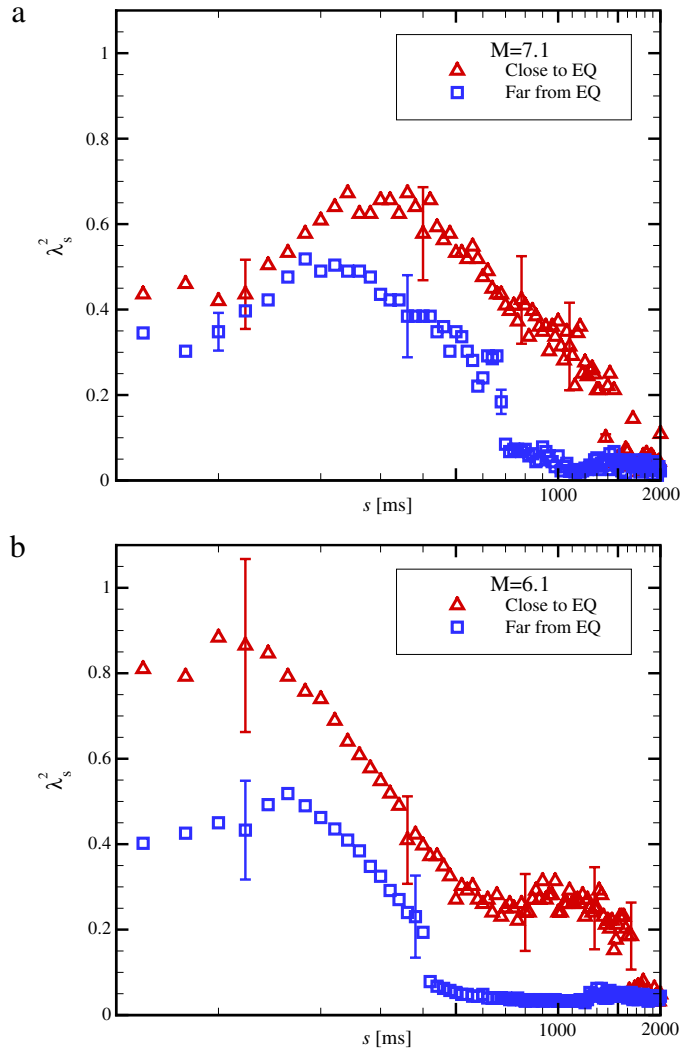


Fig. 73. Scale dependence of λ_s^2 vs $\log s$. (a) The $M = 7.1$ event, far from [data set (a)] and close to [data set (b)] the earthquake. For the data set (a) and $s > 700$ ms, $\lambda_s^2 \rightarrow 0$, implying that the increments' PDF is Gaussian, but for the data set (b) λ_s^2 deviates strongly from 0 for $700 \text{ ms} < s < 1500$ ms. (b) Same as in (a), but for the $M = 6.1$ event. When $\lambda_s \rightarrow 0$ the error bars are about the same size as the symbols. Source: From [53].

cascade process from the large to small scales, one expects the statistics to increasingly deviate from Gaussianity, in order to arrive at Eq. (4.20). Note that, a non-Gaussian PDF with fat tails on small scales indicates an increased probability of occurrence of short-time *extreme* seismic fluctuations.

It is shown that this analysis may be used as a new precursor for detecting an impending earthquake. A window containing one hour of data is selected and moved with $\Delta t = 15$ min to determine the temporal dependence of λ_s^2 . Guided by Fig. 7, the local temporal variations of λ_s^2 for $s = 800$ ms are investigated. According to Fig. 73, for $s \simeq 800$ ms, the difference between the values of λ^2 is large enough for the background data and the data set near the earthquakes. Hence, such a time scale may be used as the characteristic time for the dynamics of the non-Gaussian indicator λ_s^2 . Fig. 74(b) and (d) display a well-pronounced, systematic increase in λ_s^2 as the earthquakes are approached. Taking into account the estimated error of λ_s^2 for the background fluctuations in Fig. 74, we see that about 7 and 5 h before the earthquakes values of λ_s^2 are larger, by more than two standard deviations, than those for the background.

Due to the attenuation of elastic waves in Earth [386–389], stations that are far from an earthquake epicenter cannot provide any clue to the occurrence of the earthquakes. It is checked for several earthquakes. Shown in Fig. 75 are the results for the $M = 5.4$ California earthquake, occurred at (40.837 N, 123.499 W). The station at a distance $d \simeq 128$ km from the epicenter does provide an alert of about 3 h for the earthquake, whereas that at $d \simeq 400$ km does not.

They also analyzed several other earthquakes of various magnitudes. It is examined that for events with $M \leq 5$ the increase in λ_s^2 is not large, even if the data are collected in stations as close as 100 km from the epicenters. When the data

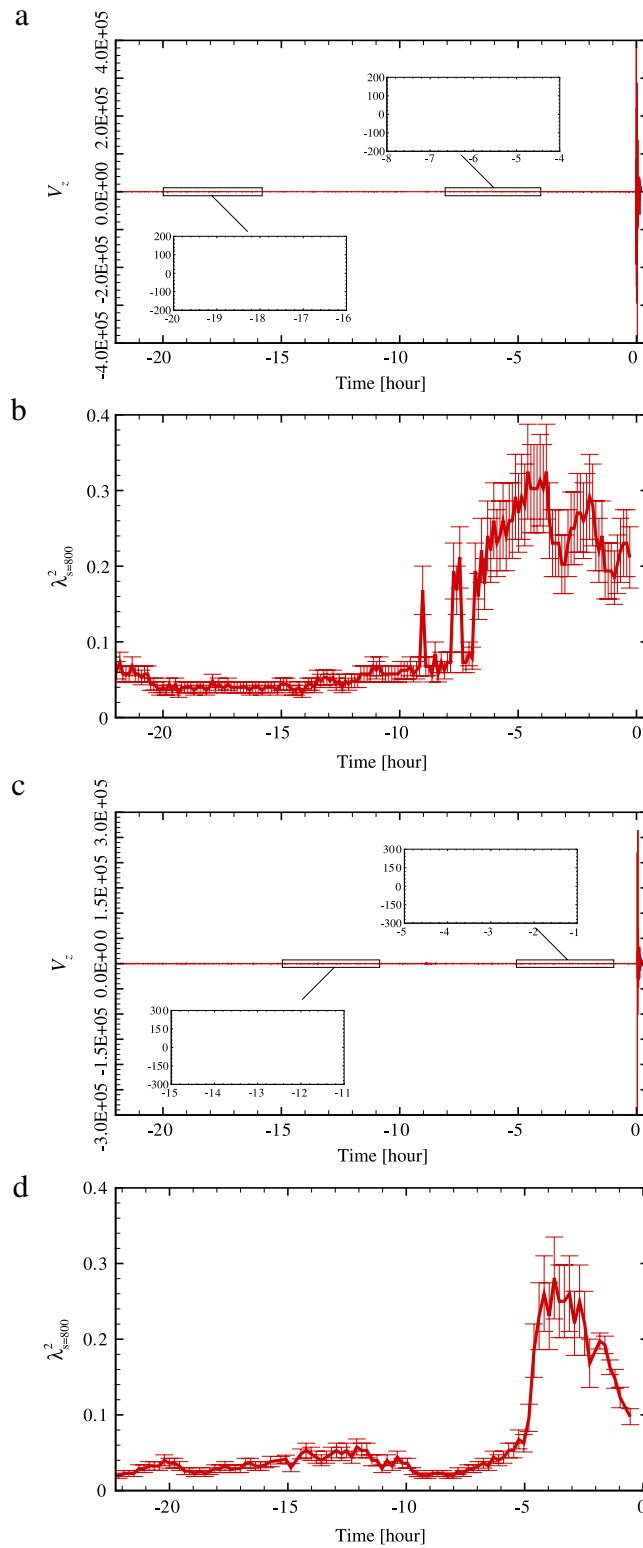


Fig. 74. The local temporal dependence of λ_s^2 and the flatness for $s = 800$ ms, over a one-hour period, for the $M = 7.1$ and $M = 6.1$ events, indicating a gradual, systematic increase on approaching the earthquakes.
 Source: From [53].

for large earthquakes in Pakistan and Iran were analyzed, they exhibited the same types of trends as those presented above, for the time variations of λ_s^2 close to the earthquakes. For example, for the $M = 7.6$ earthquake that occurred on August 10,

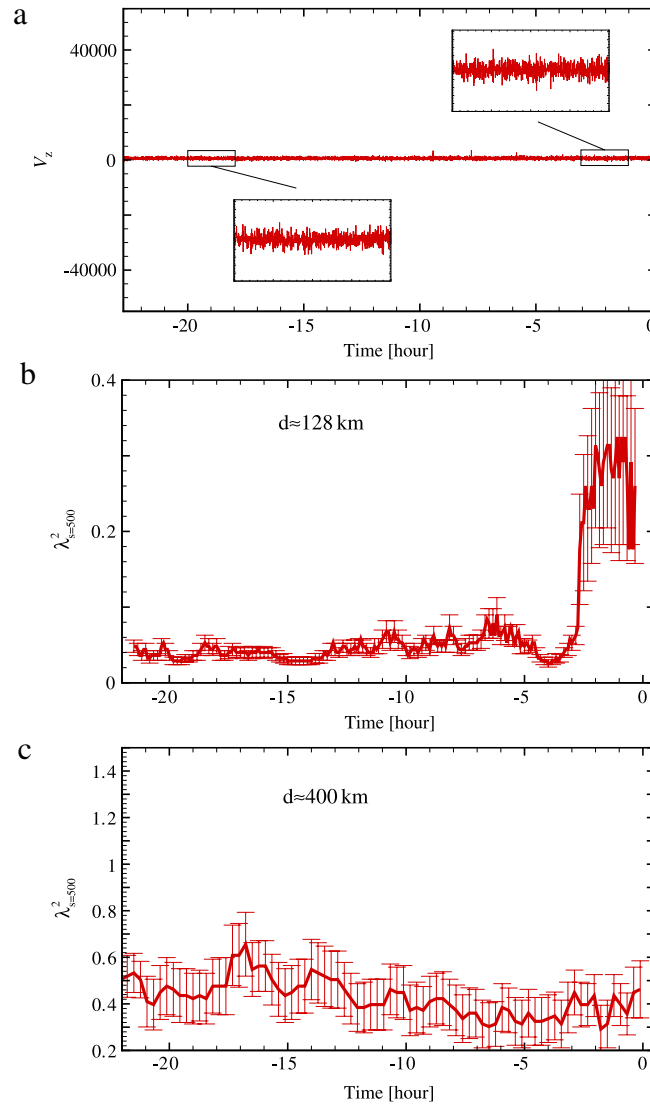


Fig. 75. (a) The data for the $M = 5.4$ earthquake in California. (b) and (c) Show the local temporal dependence of λ_s^2 for $s = 500$ ms, collected at stations with a distance d from the epicenter. The station at $d = 128$ km provides the alert, whereas the other station does not. Source: From [53].

2005, in Pakistan, the transition in the value of λ_s^2 occurred about 10 h before the event, and for the $M = 6.3$ earthquake that occurred in northern Iran on May 28, 2004, it happened about 4 h before the earthquake.

The same transition in earthquakes in Algeria, California, China, Indonesia, Iran, Japan, Pakistan, Peru, Spain, and Italy has been observed and reported in [54].

In summary, the temporal dependence of the fat tails of the PDF of the increments of the vertical velocity $V_z(t)$ of Earth, collected at broad-band stations near earthquakes' epicenters, exhibits a gradual, systematic increase in the probability of the appearance of large values on approaching a large or moderate earthquake, which is interpreted as an alert for the earthquake. To estimate the alert time one must first estimate the time scale s for moving λ_s^2 by plotting it vs. s for the data set (a), and selecting s such that $\lambda^2 \rightarrow 0$. On this scale the difference between λ_s^2 for the data sets (a) and (b) will be large enough to yield a meaningful alert for the earthquake. One must also estimate λ_s^2 or the flatness in some windows and move it over the time series, in order to observe its variations with the time [53,54].

7. Conclusions and outlook

The description of complex systems on the basis of stochastic processes, which include nonlinear dynamics, seems to be a promising approach for the future. The challenge will be to extend the understanding to more complex processes, such as

the Lévy processes, processes with no white noise, or higher-dimensional processes, to name but a few. As has been shown in this review, for these problems it should be possible to derive from precise mathematical results general methods of data series analysis.

Besides the further improvement of the method, we are convinced that there is still a wide range of further applications. Advanced sensor techniques enable scientists to collect huge data sets measured with high precision. Based on the stochastic approach we have presented here, the question is no longer how to invest much efforts into noise reduction but, to the contrary, the involved noise can help one to derive a better characterization and, thus, a better understanding of the system considered. Thus, there are many applications in the inanimate and the animate world, ranging from technical applications over socio-econo systems to biomedical applications. An interesting feature will be the extraction of higher correlation aspects, such as the question of the cause and effect chain, which may be unfolded by asymmetric determinism and the reconstructed noise terms from data.

It would be interesting to extend the methods of data analysis reviewed in the present contribution to anomalous diffusion processes, which have been reviewed in [390–393]. Recently, continuous representations of Lévy flights have been discussed [394] as well as certain generalized Langevin equations for anomalous diffusion have been derived [395–399]. However, it should be noticed that these processes are, in general, non-Markovian and, therefore, multiple time correlations have to be considered as well [400–403]. It would be interesting to extend the tools discussed in the present review to this class of stochastic processes.

Acknowledgments

We would like to thank F. Böttcher, J. Davoudi, F. Ghasemi, J. Gottschall, G. R. Jafari, D. Kleinhans, St. Lück, Ch. Renner, M. Siefert, S. Siegert and M. Wächter, whose Ph.D. theses have contributed much to this review article. M.R.R.T. thanks the Alexander von Humboldt Foundation and DFG through Grants No. 190/135-1 for financial support.

References

- [1] H. Haken, *Synergetics, An Introduction*, Springer, Berlin, Heidelberg, 1983.
- [2] H. Haken, *Advanced Synergetics*, Springer, Berlin, Heidelberg, 1987.
- [3] H. Haken, *Information and Self-Organization: A Macroscopic Approach to Complex Systems*, Springer, Berlin, 2000.
- [4] H. Haken, *Synergetics: Introduction and Advanced Topics*, Springer Verlag, Berlin, Heidelberg, New York, 2004.
- [5] G. Nicolis, I. Prigogine, *Exploring Complexity*, W. H. Freeman & Co, San Francisco, 1989.
- [6] P. Bak, *How Nature Works: The Science of Self-Organized Criticality*, Oxford University Press, 1999.
- [7] J.D. Hamilton, *Time Series Analysis*, Princeton University Press, 1994.
- [8] H. Kantz, T. Schreiber, *Nonlinear Time Series Analysis*, Cambridge University Press, 2003.
- [9] R.H. Stoffer, S. David, *Time Series Analysis and Its Applications*, Springer-Verlag, Berlin, 2006.
- [10] R. Friedrich, J. Peinke, *Phys. Rev. Lett.* 78 (1997) 863.
- [11] R. Friedrich, J. Peinke, *Physica D* 102 (1997) 147.
- [12] J. Davoudi, M. Reza Rahimi Tabar, *Phys. Rev. Lett.* 82 (1999) 1680.
- [13] R. Friedrich, J. Peinke, M.R. Rahimi Tabar, in: R.A. Meyers (Ed.), *Encyclopedia of Complexity and Systems Science*, Springer-Verlag, Berlin, 2009, p. 3574.
- [14] H. Risken, *The Fokker–Planck Equation*, 2nd ed., Springer, Berlin, 1989.
- [15] N.G. Van Kampen, *Stochastic Processes in Physics and Chemistry*, North Holland, Amsterdam, 1981.
- [16] P. Hänggi, H. Thomas, *Phys. Rep.* 88 (1982) 207.
- [17] C.W. Gardiner, *Handbook of Stochastic Methods*, Springer-Verlag, Berlin, 1983.
- [18] R. Friedrich, S. Siegert, J. Peinke, St. Lück, M. Siefert, M. Lindemann, J. Raethjen, G. Deuschl, G. Pfister, *Phys. Lett. A* 271 (2000) 217.
- [19] J. Gradisek, I. Grabec, S. Siegert, R. Friedrich, *Mech. Syst. Signal Process.* 16 (5) (2002) 831.
- [20] J. Gradisek, S. Siegert, R. Friedrich, I. Grabec, *J. Sound Vib.* 252 (3) (2002) 545.
- [21] T.D. Frank, P.J. Beek, R. Friedrich, *Phys. Lett. A* 328 (2004) 219.
- [22] T.D. Frank, R. Friedrich, P.J. Beek, *Stoch. Dyn.* 9 (2004) 44.
- [23] P. Sura, S.T. Gille, *J. Marine Res.* 313 (2003).
- [24] P. Sura, *J. Atmos. Sci.* 60 (2003) 654.
- [25] S. Kriso, R. Friedrich, J. Peinke, P. Wagner, *Phys. Lett. A* 299 (2002) 287.
- [26] T. Kuusela, *Phys. Rev. E* 69 (2004) 031916.
- [27] R. Friedrich, K. Marzinzik, A. Schmigel, in: J. Parisi, S.C. Muller, W. Zimmermann (Eds.), *A Perspective Look at Nonlinear Media*, in: *Lecture Notes in Physics*, vol. 503, Springer-Verlag, Berlin, 1997, p. 313.
- [28] R. Friedrich, J. Zeller, J. Peinke, *Europhys. Lett.* 41 (1998) 153.
- [29] C. Renner, J. Peinke, R. Friedrich, *J. Fluid Mech.* 433 (2001) 383.
- [30] G.R. Jafari, S.M. Fazlei, F. Ghasemi, S. Vaez Allaei, M. Reza Rahimi Tabar, A. Iraj Zad, G. Kavei, *Phys. Rev. Lett.* 91 (2003) 226101.
- [31] M. Wächter, F. Riess, T. Schimmel, U. Wendt, J. Peinke, *Eur. Phys. J. B* 41 (2004) 259.
- [32] G.R. Jafari, M. Reza Rahimi Tabar, A. Iraj Zad, G. Kavei, *J. Phys. A* 375 (2007) 239; M. Vahabi, G.R. Jafari, N. Mansour, *J. Stat. Mech.* (2008) P03002.
- [33] M. Allahkarami, J.C. Hanana, H.A. Balea, *Appl. Sur. Sci.* 257 (2010) 857.
- [34] M. Wächter, F. Riess, H. Kantz, J. Peinke, *Europhys. Lett.* 64 (2003) 579.
- [35] P. Sangpour, O. Akhavan, A.Z. Moshfegh, G.R. Jafari, M. Reza Rahimi Tabar, *Phys. Rev. B* 71 (2005) 155423.
- [36] A. Mora, M. Haase, *Nonlinear Dyn.* 44 (2006) 307.
- [37] S.M. Fazeli, A.H. Shirazi, G.R. Jafari, *New J. Phys.* 10 (2008) 083020; S. Hosseinabadi, A. Mortezaali, A.A. Masoudi, *Sur. Interface Anal.* 40 (2008) 71.
- [38] M. Tutkun, L. Mydlarski, *New J. Phys.* 6 (2004) 49.
- [39] R. Friedrich, J. Peinke, Ch. Renner, *Phys. Rev. Lett.* 84 (2000) 5224.
- [40] Ch. Renner, J. Peinke, R. Friedrich, *Physica A* 298 (2001) 499.
- [41] F. Ghasemi, M. Sahimi, J. Peinke, R. Friedrich, G.R. Jafari, M. Reza Rahimi Tabar, *Phys. Rev. E* 75 (2007) R060102.
- [42] F. Farahpour, Z. Eskandari, A. Bahraminasab, G.R. Jafari, F. Ghasemi, M. Reza Rahimi Tabar, M. Sahimi, *Physica A* 385 (2007) 601.

- [43] V.N. Smelyanskiy, D.G. Luchinsky, A. Stefanovska, P.V.E. McClintock, *Phys. Rev. Lett.* 94 (2005) 098101.
- [44] V.N. Smelyanskiy, D.G. Luchinsky, D.A. Timuçin, A. Bandrivskyy, *Phys. Rev. E* 72 (2005) 026202.
- [45] M. Reza Rahimi Tabar, F. Ghasemi, J. Peinke, R. Friedrich, K. Kaviani, F. Taghavi, S. Sadeghi, G. Bijani, M. Sahimi, *Comput. Sci. Eng.* 8 (2006) 54.
- [46] F. Ghasemi, J. Peinke, M. Reza Rahimi Tabar, M. Sahimi, *Int. J. Mod. Phys. C* 17 (2006) 571.
- [47] F. Ghasemi, M. Sahimi, J. Peinke, M. Reza Rahimi Tabar, *J. Biol. Phys.* 32 (2006) 117.
- [48] F. Ghasemi, A. Bahraminasab, M.S. Movahed, K.R. Sreenivasan, S. Rahvar, M. Reza Rahimi Tabar, *J. Stat. Mech.* (2006) P11008.
- [49] D. Holstein, H. Kantz, *Phys. Rev. E* 79 (2009) 056202.
- [50] J. Prusseit, K. Lehnertz, *Phys. Rev. Lett.* 98 (2007) 138103.
- [51] K. Lehnertz, *J. Biol. Phys.* 34 (2008) 253.
- [52] M. Reza Rahimi Tabar, M. Sahimi, F. Ghasemi, K. Kaviani, M. Allamehzadeh, J. Peinke, M. Mokhtari, M. Vesaghi, M.D. Niry, A. Bahraminasab, S. Tabatabai, F. Fayazbakhsh, M. Akbari, *Modelling Critical and Catastrophic Phenomena in Geoscience: A Statistical Physics Approach*, in: *Lecture Notes in Physics*, 705, Springer Verlag, Berlin-Heidelberg, 2007, p. 281.
- [53] P. Manshour, S. Saberi, M. Sahimi, J. Peinke, A.F. Pacheco, M. Reza Rahimi Tabar, *Phys. Rev. Lett.* 102 (2009) 014101.
- [54] P. Manshour, F. Ghasemi, T. Matsumoto, J. Gómez, M. Sahimi, J. Peinke, A.F. Pacheco, M. Reza Rahimi Tabar, *Phys. Rev. E* 82 (2010) 036105.
- [55] U. Frisch, *Turbulence, The Legacy of A. N. Kolmogorov*, Cambridge University Press, Cambridge, England, 1995.
- [56] J. Feder, *Fractals*, Plenum Press, New York, 1998.
- [57] V.S. L'vov, I. Procaccia, *Phys. Rev. Lett.* 76 (1996) 2898.
- [58] V.S. L'vov, I. Procaccia, *Phys. Rev. E* 54 (1996) 6268.
- [59] G. Eyink, *Phys. Lett. A* 172 (1993) 355.
- [60] G. Eyink, *Phys. Rev. E* 48 (1993) 1823.
- [61] A.L. Fairhall, B. Druvha, V.S. L'vov, I. Procaccia, K.R. Sreenivasan, *Phys. Rev. Lett.* 79 (1997) 3174.
- [62] R. Benzi, L. Biferale, F. Toschi, *Phys. Rev. Lett.* 80 (1998) 3244.
- [63] J. Davoudi, M. Reza Rahimi Tabar, *Phys. Rev. E* 61 (2000) 6563.
- [64] S.O. Rice, *Bell Syst. Tech. J.* 23 (1944) 282.
- [65] S.O. Rice, *Bell Syst. Tech. J.* 24 (1945) 46.
- [66] F. Shahbazi, S. Sobhanian, M. Reza Rahimi Tabar, S. Khorram, G.R. Frootan, H. Zahed, *J. Phys. A: Math. Gen.* 36 (2003) 2517.
- [67] A. Bahraminasab, M.S. Movahed, S.D. Nassiri, A.A. Masoudi, M. Sahimi, *J. Stat. Phys.* 124 (2006) 1471.
- [68] V.V. Yanovsky, A.V. Chechkin, D. Schertzer, A.V. Tur, *Physica A* 282 (2000) 13.
- [69] D. Schertzer, M. Larchev'equ, J. Duan, V.V. Yanovsky, S. Lovejoy, *J. Math. Phys.* 42 (2001) 200.
- [70] B.V. Gnedenko, A.N. Kolmogorov, *Limit Distributions of Sums of Independent Random Variables*, Addison-Wesley, 1954.
- [71] T.H. Solomon, E.R. Weeks, H.L. Swinney, *Phys. Rev. Lett.* 71 (1993) 3975.
- [72] J.-P. Bouchaud, A. Georges, *Phys. Rep.* 195 (1990) 127.
- [73] D. Brockmann, L. Hufnagel, T. Geisel, *Nature* 439 (2006) 462.
- [74] R.N. Mategna, H.E. Stanley, *Nature* 376 (1995) 46.
- [75] W. Feller, *An Introduction to Probability Theory and its Applications*, vols. 1, 2, John Wiley, 1971.
- [76] A. Einstein, Über die von der molekularkinetischen Theorie der Wärme geforderte Bewegung von in ruhenden Flüssigkeiten suspendierten Teilchen, *Ann. Phys.* 17 (1905) 549.
- [77] St. Lück, Ch. Renner, J. Peinke, R. Friedrich, *Phys. Lett. A* 359 (2006) 335.
- [78] A.N. Kolmogorov, *Mathematische Annalen* 104 (1931) 415.
- [79] M. Siefert, A. Kittel, R. Friedrich, J. Peinke, *Europhys. Lett.* 61 (2003) 466.
- [80] F. Böttcher, J. Peinke, D. Kleinhans, R. Friedrich, P.G. Lind, M. Haase, *Phys. Rev. Lett.* 97 (2006) 090603.
- [81] B. Lehle, *Phys. Rev. E* 83 (2011) 021113.
- [82] T.W. Epps, *J. Amer. Statist. Assoc.* 74 (1979) 291.
- [83] D. Kleinhans, R. Friedrich, *Phys. Lett. A* 368 (2007) 194.
- [84] D. Kleinhans, R. Friedrich, M. Wächter, J. Peinke, *Phys. Rev. E* 76 (2007) 041109.
- [85] F. Ghasemi, J. Peinke, M. Sahimi, M. Reza Rahimi Tabar, *Euro. Phys. J. B* 47 (2005) 411.
- [86] D. Lamouroux, K. Lehnertz, *Phys. Lett. A* 373 (2009) 3507.
- [87] F. Wilcoxon, *Biometrics* 1 (1945) 80.
- [88] J. Gottschall, J. Peinke, *New J. Phys.* 10 (2008) 083034.
- [89] J. Gottschall, J. Peinke, V. Lippens, V. Nagel, *Phys. Lett. A* 373 (2008) 811.
- [90] S. Siegert, R. Friedrich, *Phys. Rev. E* 64 (2001) 041107.
- [91] M. Wächter, A. Kouzmitchev, J. Peinke, *Phys. Rev. E* 70 (2004) 055103(R).
- [92] D. Kleinhans, R. Friedrich, A. Nawroth, J. Peinke, *Phys. Lett. A* 346 (2005) 42.
- [93] A. Nawroth, J. Peinke, D. Kleinhans, R. Friedrich, *Phys. Rev. E* 76 (2007) 056102.
- [94] A.M. Van Mourik, A. Daffertshofer, P.J. Beek, *Phys. Lett. A* 351 (2006) 13.
- [95] A.M. Van Mourik, A. Daffertshofer, P.J. Beek, *Biol. Cybern.* 94 (2006) 233.
- [96] R. Riera, C. Anteneodo, *J. Stat. Mech.* (2010) P04020.
- [97] S.J. Lade, *Phys. Lett. A* 373 (2009) 3705.
- [98] C. Anteneodo, S.M. Duarte Queir's, *Phys. Rev. E* 82 (2010) 041122.
- [99] C. Honisch, R. Friedrich, *Phys. Rev. E* 83 (2011) 066701.
- [100] A. Nawroth, J. Peinke, *Phys. Lett. A* 360 (2006) 234.
- [101] R. Stresing, J. Peinke, *New J. Phys.* 12 (2010) 103046.
- [102] A. Nawroth, R. Friedrich, J. Peinke, *New J. Phys.* 12 (2010) 083021.
- [103] A.H. Shirazi, G.R. Jafari, J. Davoudi, J. Peinke, M. Reza Rahimi Tabar, M. Sahimi, *J. Stat. Mech.* (2009) P07046.
- [104] J. Zhang, M. Small, *Phys. Rev. Lett.* 96 (2006) 238701.
- [105] A. Shreim, P. Grassberger, W. Nadler, B. Samuelsson, J.E.S. Socolar, M. Paczuski, *Phys. Rev. Lett.* 98 (2007) 198701.
- [106] L. Lacasa, B. Luque, F. Ballesteros, J. Luque, J.C. Nuño, *Proc. Natl. Acad. Sci.* 105 (2008) 4972.
- [107] G.R. Jafari, M.S. Movahed, S.M. Fazeli, M. Reza Rahimi Tabar, S.F. Masoudi, *J. Stat. Mech.* (2006) P06008.
- [108] F. Shayeganfar, M. Hölling, J. Peinke, M. Reza Rahimi Tabar, *J. Phys. A: Math. Gen.* (2011) (in press).
- [109] M.S. Movahed, A. Bahraminasab, H. Rezaazadeh, A.A. Masoudi, *J. Phys. A: Math. Gen.* 39 (2006) 3903.
- [110] C.-K. Peng, J. Mietus, J.M. Hausdorff, S. Havlin, H.E. Stanley, A.L. Goldberger, *Phys. Rev. Lett.* 70 (1993) 1343.
- [111] C.-K. Peng, S.V. Buldyrev, S. Havlin, M. Simons, H.E. Stanley, A.L. Goldberger, *Phys. Rev. E* 49 (1994) 1685.
- [112] S.M. Ossadnik, S.B. Buldyrev, A.L. Goldberger, S. Havlin, R.N. Mantegna, C.-K. Peng, M. Simons, H.E. Stanley, *Biophys. J.* 67 (1994) 64.
- [113] M.S. Taqqu, V. Teverovsky, W. Willinger, *Fractals* 3 (1995) 785.
- [114] S.V. Goldberger, S. Havlin, R.N. Mantegna, M.E. Matsa, C.-K. Peng, M. Simons, H.E. Stanley, *Phys. Rev. E* 51 (1995) 5084.
- [115] S.V. Buldyrev, N.V. Dokholyan, A.L. Goldberger, S. Havlin, C.-K. Peng, H.E. Stanley, G.M. Viswanathan, *Physica A* 249 (1998) 430.
- [116] J.W. Kantelhardt, E. Koscielny-Bunde, H.H. Rego, S. Havlin, A. Bunde, *Physica A* 295 (2001) 441.
- [117] K. Hu, P. Ivanov, Z. Chen, P. Carpena, H.E. Stanley, *Phys. Rev. E* 64 (2001) 011114.
- [118] Z. Chen, P. Ivanov, K. Hu, H.E. Stanley, *Phys. Rev. E* 65 (2002) 041107.
- [119] M.S. Movahed, G.R. Jafari, F. Ghasemi, S. Rahvar, M. Reza Rahimi Tabar, *J. Stat. Mech.* (2006) P02003.
- [120] E. Alessio, A. Carbone, G. Castelli, V. Frappietro, *Eur. Phys. J. B* 27 (2002) 197.

- [121] A. Carbone, G. Castelli, Noise in Complex Systems and Stochastic Dynamics, in: Proc. of SPIE, vol. 5114, 2003, p. 406.
- [122] J.F. Muzy, E. Bacry, A. Arneodo, Phys. Rev. Lett. 67 (1991) 3515.
- [123] H.E. Hurst, R.P. Black, Y.M. Simaika, Long-Term Storage. An Experimental Study, Constable, London, 1965.
- [124] A.R. Mehrabi, H. Rassamdana, M. Sahimi, Phys. Rev. E 56 (1997) 712.
- [125] A. Eke, P. Herman, L. Kocsis, L.R. Kozak, Physiol. Meas. 23 (2002) R1–R38.
- [126] B. Podobnik, H.E. Stanley, Phys. Rev. Lett. 100 (2008) 084102.
- [127] F. Wang, K. Yamasaki, S. Havlin, H.E. Stanley, Phys. Rev. E 79 (2009) 016103.
- [128] S.Y. Chen, K.R. Sreenivasan, M. Nelkin, Phys. Rev. Lett. 79 (1997) 1253.
- [129] S.Y. Chen, K.R. Sreenivasan, M. Nelkin, N.Z. Cao, Phys. Rev. Lett. 79 (1997) 2253.
- [130] T. Schreiber, A. Schmitz, Physica D 142 (2000) 346.
- [131] J. Theiler, S. Eubank, A. Longtin, B. Galdrikian, J.D. Farmer, Physica D 58 (1992) 77.
- [132] J. Theiler, P.S. Linsay, D.M. Rubin, Time Series Prediction: Forecasting the Future and Understanding the Past, in: Santa Fe Institute Studies in the Science of Complexity, Proc., vol. XV, Addison-Wesley, Reading, MA, 1993.
- [133] J. Theiler, D. Prichard, Fields Inst. Commun. 11 (1997) 99.
- [134] M. Ragwitz, H. Kantz, Phys. Rev. Lett. 87 (2001) 254501.
- [135] M. Ragwitz, H. Kantz, Phys. Rev. Lett. 89 (2002) 149402.
- [136] R. Friedrich, Ch. Renner, M. Siefert, J. Peinke, Phys. Rev. Lett. 89 (2002) 149401.
- [137] A.-L. Barabasi, H.E. Stanley, Fractal Concepts in Surface Growth, Cambridge University Press, New York, 1995.
- [138] V.S. L'vov, I. Procaccia, Phys. Fluids 8 (1996) 2565.
- [139] A.A. Donkov, A.D. Donkov, E.I. Grancharova, Int. J. Mod. Phys. A12 (1997) 165.
- [140] B. Castaing, Y. Gagne, E.J. Hopfinger, Physica D 46 (1990) 177.
- [141] B. Castaing, Physica D 73 (1994) 31.
- [142] B. Castaing, J. Physique II France 6 (1996) 105.
- [143] B. Jouault, P. Lipa, M. Greiner, Phys. Rev. E 59 (1999) 2451.
- [144] J. Cleve, M. Greiner, B.R. Pearson, K.R. Sreenivasan, Phys. Rev. E 69 (2004) 066316.
- [145] S. Ghashghaie, W. Breyman, J. Peinke, P. Talkner, Y. Dodge, Nature 381 (1996) 767.
- [146] H.E. Stanley, V. Plerou, Quant. Finance 1 (2001) 563.
- [147] E. Bacry, J. Delour, J.F. Muzy, Phys. Rev. E 64 (2001) 026103.
- [148] K. Kiyono, Z.R. Struzik, Y. Yamamoto, Phys. Rev. Lett. 96 (2006) 068701.
- [149] G.R. Jafari, M.S. Movahed, P. Noroozadeh, A. Bahraminasab, M. Sahimi, F. Ghasemi, M. Reza Rahimi Tabar, Int. J. Mod. Phys. C 18 (2007) 1689; G.R. Jafari, A. Bahraminasab, P. Noroozadeh, Int. J. Mod. Phys. C 18 (2007) 1223.
- [150] K. Kiyono, Z.R. Struzik, N. Aoyagi, F. Togo, Y. Yamamoto, Phys. Rev. Lett. 95 (2005) 058101.
- [151] B. Dubrulle, Phys. Rev. Lett. 73 (1994) 959.
- [152] B. Dubrulle, Eur. Phys. J. B 13 (2000) 1.
- [153] Z.-S. She, E.C. Waymire, Phys. Rev. Lett. 74 (1995) 262.
- [154] K. Kiyono, Phys. Rev. E 79 (2009) 031129.
- [155] H.-G. Purwins, S. Amiranashvili, Physik Journal 6 (2007) 21.
- [156] H.U. Bödeker, M. Röttger, A.W. Liehr, T.D. Frank, R. Friedrich, H.G. Purwins, Phys. Rev. E 67 (2003) 056220.
- [157] A.W. Liehr, H.U. Bödeker, M. Röttger, T.D. Frank, R. Friedrich, H.G. Purwins, New J. Phys. 5 (2003) 89.
- [158] M. Siefert, J. Peinke, Phys. Rev. E 70 (2004) 015302.
- [159] E. Anahua, M. Lange, F. Böttcher, St. Barth, J. Peinke, Stochastic Analysis of the Power Output for a Wind Turbine, DEWEK, 2004.
- [160] E. Anahua, St. Barth, J. Peinke, in: J. Peinke, P. Schaumann, St. Barth (Eds.), Wind Energy – Proceedings of the Euromech Colloquium, Springer, Berlin, 2007, p. 173.
- [161] E. Anahua, St. Barth, J. Peinke, Markovian Power Curves for Wind Turbines, Wind Energy 11 (2008) 219.
- [162] J. Gottschall, J. Peinke, Envir. Res. Lett. 3 (2008) 015005.
- [163] M. Kern, O. Buser, J. Peinke, M. Siefert, L. Vulliet, Phys. Lett. A 336 (2005) 428.
- [164] D.G. Luchinsky, M.M. Millonas, V.N. Smelyanskiy, A. Pershakova, A. Stefanovska, P.V. McClintock, Phys. Rev. E 72 (2005) 021905.
- [165] J. Kirchner, W. Meyer, M. Elsholz, B. Hensel, Phys. Rev. E 76 (2007) 021110.
- [166] R. Bartsch, Th. Hennig, A. Heinen, S. Heinrichs, P. Maass, Physica A 354 (2005) 415.
- [167] Th. Hennig, P. Maass, J. Hayano, S. Heinrichs, J. Biol. Phys. 32 (2006) 383.
- [168] J. Egger, T. Jonsson, Tellus A 51 (2002) 1.
- [169] T. Stemler, J.P. Werner, H. Benner, W. Just, Phys. Rev. Lett. 98 (2007) 044102.
- [170] A. Bahraminasab, F. Ghasemi, A. Stefanovska, P.V.E. McClintock, H. Kantz, Phys. Rev. Lett. 100 (2008) 084101; A. Bahraminasab, D. Kenwright, A. Stefanovska, F. Ghasemi, P.V.E. McClintock, IET Syst. Biol. 2 (2008) 48.
- [171] N. Stepp, T.D. Frank, Eur. Phys. J. B 67 (2009) 251.
- [172] M. Strumik, W. Macek, Phys. Rev. E 78 (2008) 026414.
- [173] D.G. Luchinsky, V.N. Smelyanskiy, A. Duggento, P.V. McClintock, Phys. Rev. E 77 (2008) 061105.
- [174] G.R. Jafari, M. Sahimi, M.R. Rasaei, M. Reza Rahimi Tabar, Phys. Rev. E 83 (2011) 026309.
- [175] F. Shayeganfar, S. Jabbari-Farouji, M.S. Movahed, G.R. Jafari, M. Reza Rahimi Tabar, Phys. Rev. E 81 (2010) 061404.
- [176] A. Farahzadi, P. Niyamakom, M. Beigmohammadi, N. Mayer, M. Heuken, F. Ghasemi, M. Reza Rahimi Tabar, T. Michely, M. Wuttig, Europhys. Lett. 90 (2010) 10008.
- [177] S. Kimiagar, M.S. Movahed, S. Khorram, M. Reza Rahimi Tabar, J. Stat. Phys. (2011) doi:10.1007/s10955-011-0171-5.
- [178] F. Shayeganfar, S. Jabbari-Farouji, M. Sadegh Movahed, G.R. Jafari, M. Reza Rahimi Tabar, Phys. Rev. E 80 (2009) 061126.
- [179] A. Bahraminasab, F. Ghasemi, A. Stefanovska, P.V.E. McClintock, R. Friedrich, New J. Phys. 11 (2009) 103051.
- [180] K. Patanarapeelert, T.D. Frank, I.M. Tang, Math. Comput. Modelling 53 (2011) 122.
- [181] H.U. Bödeker, C. Beta, T.D. Frank, E. Bodenschatz, Europhys. Lett. 90 (2010).
- [182] R. Stresing, J. Peinke, R.E. Seoud, J.C. Vassilicos, Phys. Rev. Lett. 104 (2010) 194501.
- [183] G. Nabyouini, B.J. Farahani, Appl. Surf. Sci. 256 (2009) 674.
- [184] A.A. Ramos, Astron. Astrophys. 494 (2009) 287.
- [185] M.H. Peters, J. Chem. Phys. 134 (2011) 025105.
- [186] M. Greiner, J. Gieseemann, P. Lipa, Phys. Rev. E 56 (1997) 4263.
- [187] A. Riegert, N. Baba, K. Gelfert, W. Just, H. Kantz, Phys. Rev. Lett. 94 (2005) 054103.
- [188] P.G. Lind, A. Mora, J.A. Gallas, M. Haase, Phys. Rev. E 72 (2005) 056706.
- [189] S. Sato, T. Kitamura, Phys. Rev. E 73 (2006) 026119.
- [190] I. Horenko, C. Hartmann, C. Schütte, F. Noe, Phys. Rev. E 76 (2007) 016706.
- [191] E. Racca, F. Laio, D. Poggi, L. Ridolfi, Phys. Rev. E 75 (2007) 011126.
- [192] T. Le Borgne, M. Dentz, J. Carrera, Phys. Rev. E 78 (2008) 026308.
- [193] J. Masoliver, J. Perelló, Phys. Rev. E 78 (2008) 056104.
- [194] T. Letz, J. Peinke, A. Kittel, How to characterize chaotic time series distorted by interacting dynamical noise, 2007, preprint.
- [195] A. Babloyantz, A. Destexhe, Proc. Natl. Acad. Sci. USA 83 (1986) 3513.
- [196] T. Elbert, J. William, Z. Kowalik, J.E. Skinner, K.E. Graf, N. Birbaumer, Physiol. Rev. 74 (1) (1994) 1–47.

- [197] W.S. Pritchards, D.W. Duke, *Brain and Cognition* 27 (1995) 353.
- [198] H.G. Schuster, *Deterministic Chaos*, Physik-Verlag, Weinheim, 1984.
- [199] G.W. Frank, T. Lookman, M.A. Nerenberg, C. Essex, J. Lemieux, W. Blume, *Physica D* 46 (1990) 427.
- [200] J.B. Bassingthwaite, L.S. Liebowitch, B.J. West, *Fractal Physiology*, Oxford University Press, 1994.
- [201] F.H. Lopes da Silva, E. Niedermeyer, *Electroencephalography: Basic Principles, Clinical Applications, and Related Fields*, William & Wilkins, Baltimore, 1993.
- [202] J.P. Pijn, J. van Neerven, A. Noest, F.H. Lopes da Silva, *Electroencephalogr. Clin. Neurophysiol.* 79 (1991) 371.
- [203] K. Lehnertz, C.E. Elger, *Electroencephalogr. Clin. Neurophysiol.* 95 (1995) 108; J. Prusseit, K. Lehnertz, *Phys. Rev. E* 77 (2008) 041914.
- [204] J.P. Pijn, D.N. Velis, M.J. van der Heyden, J. DeGoede, C.W. Veelen, F.H. Lopes da Silva, *Brain Topography* 9 (1997) 249.
- [205] R.G. Andrzejak, F. Mormann, G. Widman, T. Kreuz, C.E. Elger, K. Lehnertz, *Epilepsy Res.* 69 (2006) 30.
- [206] D.T. Kaplan, M.I. Furman, S.M. Pincus, S.M. Ryan, L.A. Lipsitz, A.L. Goldberger, *Biophys. J.* 59 (1991) 945.
- [207] C.L.Y. Yeong, S. Torquato, *Phys. Rev. E* 57 (1998) 495.
- [208] C.L.Y. Yeong, S. Torquato, *Phys. Rev. E* 58 (1998) 224.
- [209] A. Bunde, S. Havlin, J.W. Kantelhardt, T. Penzel, J.-H. Peter, K. Voigt, *Phys. Rev. Lett.* 85 (2000) 3736.
- [210] P. Bernaola-Galvan, P.Ch. Ivanov, L.N. Amaral, H.E. Stanley, *Phys. Rev. Lett.* 87 (2001) 168105.
- [211] V. Schulte-Frohlinde, Y. Ashkenazy, P.Ch. Ivanov, L. Glass, A.L. Goldberger, H.E. Stanley, *Phys. Rev. Lett.* 87 (2001) 068104.
- [212] Y. Ashkenazy, P.Ch. Ivanov, S. Havlin, C.-K. Peng, A.L. Goldberger, H.E. Stanley, *Phys. Rev. Lett.* 86 (2001) 1900.
- [213] C.-K. Peng, S. Havlin, H.E. Stanley, A.L. Goldberger, *Chaos* 5 (1995) 82.
- [214] P.Ch. Ivanov, L.A.N. Amaral, A.L. Goldberger, H.E. Stanley, *Europhys. Lett.* 43 (1998) 363.
- [215] P.Ch. Ivanov, A. Bunde, L.A.N. Amaral, S. Havlin, J. Fritsch-Yelle, R.M. Baevsky, H.E. Stanley, A.L. Goldberger, *Europhys. Lett.* 48 (1999) 594.
- [216] P.Ch. Ivanov, L.A.N. Amaral, A.L. Goldberger, S. Havlin, M.G. Rosenblum, Z. Struzik, H.E. Stanley, *Nature (London)* 399 (1999) 461.
- [217] R.G. Turcott, M.C. Teich, *Ann. Biomed. Eng.* 24 (1996) 269.
- [218] L.A. Lipsitz, J. Mietus, G.B. Moody, A.L. Goldberger, *Circulation* 81 (1990) 1803.
- [219] N. Iyengar, C.-K. Peng, R. Morin, A.L. Goldberger, L.A. Lipsitz, *Am. J. Physiol.* 271 (1996) R1078.
- [220] C.-K. Peng, J.M. Hausdorff, A.L. Goldberger, in: J. Walleczek (Ed.), *Nonlinear Dynamics, Self-Organization, and Biomedicine*, Cambridge University Press, Cambridge, 1999.
- [221] D.C. Lin, *Int. J. Mod. Phys. C* 16 (2005) 465.
- [222] E.A. Novikov, *Dokl. Akad. Nauk USSR* 168 (1966) 1279.
- [223] D. Sornette, *Phys. Rep.* 297 (1998) 239.
- [224] D. Sornette, *Why Stock Markets Crash*, Princeton University Press, Princeton, NJ, 2003.
- [225] A. Johansen, D. Sornette, O. Ledoit, *J. Risk* 1 (1999) 5.
- [226] W.-X. Zhou, D. Sornette, *Physica D* 165 (2002) 94.
- [227] D. Sornette, C.G. Sammis, *J. Phys. I France* 5 (1995) 607.
- [228] D. Stauffer, D. Sornette, *Physica A* 252 (1998) 271.
- [229] M. Saadatfar, M. Sahimi, *Phys. Rev. E* 65 (2002) 036116.
- [230] M. Sahimi, S. Arbabi, *Phys. Rev. Lett.* 77 (1996) 3689.
- [231] L. Bachelier, *Theorie de la speculation*, Ph.D. Thesis, Annales Scientifiques de l'Ecole Normal Supérieure III-17 (1900).
- [232] P. Samuelson, *Industrial Management Review* 6 (1965) 41.
- [233] R.F. Engle, *Econometrica* 50 (1982) 987.
- [234] T. Bollerslev, *J. of Econometrics* 31 (1986) 307.
- [235] I.N. Bronstein, K.A. Semendjajew, *Taschenbuch der Mathematik Zürich-Frankfurt/M* (1987).
- [236] T. Bollerslev, I. Domowitz, *J. Finance*, 48 1421 (1993).
- [237] S.J. Taylor, *Math. Finance* 4 (1994) 183.
- [238] E. Ghysels, A. Harvey, E. Renault, *Stochastic Volatility*, in: G.S. Maddala, C.R. Rao (Eds.), *Handbook of Statistics*, vol. 14, North-Holland, Amsterdam, 1996, pp. 119–191.
- [239] A.R. Gallant, G. Tauchen, *Econometric Theory* 12 (1996) 657–681.
- [240] M. Constantin, S. Das Sarma, *Phys. Rev. E* 72 (2005) 051106.
- [241] F. Wang, K. Yamasaki, S. Havlin, H.E. Stanley, *Phys. Rev. E* 73 (2006) 026117.
- [242] R. Mantegna, H.E. Stanley, *Nature* 383 (1996) 767.
- [243] R. Mantegna, H.E. Stanley, *An Introduction to Econophysics: Correlations and Complexities in Finance*, Cambridge University Press, New York, 2000.
- [244] W. Breymann, S. Gashghaie, P. Talkner, *Int. J. Theor. Appl. Finance* 3 (3) (2000) 357.
- [245] J.P. Bouchaud, R. Cont, *Eur. Phys. J. B* 6 (1998) 543.
- [246] J.P. Bouchaud, M. Potters, *Theory of Financial Risk and Derivative Pricing: From Statistical Physics to Risk Management*, Cambridge University Press, 2003.
- [247] D. Sornette, *Phys. Rep.* 378 (2003) 198.
- [248] D. Sornette, *Critical Phenomena in Natural Sciences*, 2nd ed., Springer, Berlin, 2004.
- [249] M. Ausloos, K. Ivanova, *Phys. Rev. E* 68 (2003) 6122.
- [250] T. Di Matteo, T. Aste, M.M. Dacorogna, *Physica A* 324 (2003) 183.
- [251] T. Di Matteo, T. Aste, M.M. Dacorogna, *J. Banking Finance* 29 (2005) 827.
- [252] A. Johansen, *Physica A* 234 (2003) 157.
- [253] M. Gallegati, A.P. Kirman, M. Marsili, *The Complex Dynamics of Economic Interaction: Essays in Economics and Econophysics*, Springer Verlag, Berlin, 2004, Heidelberg, New York.
- [254] D. Abbott, J.P. Bouchaud, X. Gabaix, *Noise and Fluctuations in Econophysics and Finance*, SPIE-International Society for Optical Engine, 2005.
- [255] K.E. Bassler, G.H. Gunaratne, J.L. McCauley, *Physica A* 369 (2006) 343.
- [256] A.R. Pagan, H. Sabu, *Estudios Economics* 7 (1992) 30.
- [257] T. Bollerslev, R.F. Engle, D.B. Nelson, *ARCH Models Handbook of Econometrics* 4 (1994).
- [258] R.F. Engle, M. Rothschild (Eds.), *J. Econometrics (suppl.)* 52 (1992).
- [259] F. Drost, T. Nijman, *Econometrica* 61 (1993) 909.
- [260] T.G. Andersen, T. Bollerslev, Kellogg Graduate School of Management, Northwestern University, working paper 186, 130 (1994).
- [261] S. Picozzi, B.J. Wes, *Phys. Rev. E* 66 (2002) 046118.
- [262] V. Plerou, P. Gopikrishnan, X. Gabaix, H.E. Stanley, *Quant. Finance* 4 (2004) C11.
- [263] F. Schmitt, D. Schertzer, S. Lovejoy, *Appl. Stoch. Model D. A.* 15 (1) (1998).
- [264] D. Stauffer, D. Sornette, *Physica A* 271 (1999) 496.
- [265] R. Cont, J.P. Bouchaud, *Macroeconomic Dynamics* 4 (2000) 170.
- [266] D.-H. Kim, H. Jeong, *Phys. Rev. E* 72 (2005) 046133.
- [267] M.H.R. Stanley, L.A.N. Amaral, S.V. Buldyrev, S. Havlin, H. Leschhorn, P. Maass, R.N. Mantegna, M.A. Salinger, H.E. Stanley, *Fractals* 4 (1996) 415.
- [268] H.E. Stanley, L.A.N. Amaral, S.V. Buldyrev, A.L. Goldberger, S. Havlin, B.T. Hyman, H. Leschhorn, P. Maass, H.A. Makse, R.N. Mantegna, C.-K. Peng, M.A. Salinger, M.H.R. Stanley, G.M. Viswanathan, *Fractals* 4 (1996) 427.
- [269] M.H.R. Stanley, L.A.N. Amaral, S.V. Buldyrev, S. Havlin, H. Leschhorn, P. Maass, M.A. Salinger, H.E. Stanley, *Nature* 379 (1996) 804.

- [270] H.E. Stanley, V. Afanasyev, L.A.N. Amaral, S.V. Buldyrev, A.L. Goldberger, S. Havlin, H. Leschhorn, P. Maass, R.N. Mantegna, C.-K. Peng, P.A. Prince, M.A. Salinger, M.H.R. Stanley, G.M. Viswanathan, *Physica A* 231 (1996) 20.
- [271] H.E. Stanley, L.A.N. Amaral, S.V. Buldyrev, A.L. Goldberger, H. Leschhorn, P. Maass, H.A. Makse, C.-K. Peng, M.A. Salinger, M.H.R. Stanley, G.M. Viswanathan, *Physica A* 224 (1996) 302.
- [272] L.A. Amaral, S.V. Buldyrev, S. Havlin, H. Leschhorn, P. Maass, M.A. Salinger, H.E. Stanley, M.H.R. Stanley, *J. de Physique* 7 (1997) 621.
- [273] S.V. Buldyrev, L.A. Amaral, S. Havlin, H. Leschhorn, P. Maass, M.A. Salinger, H.E. Stanley, M.H.R. Stanley, *J. de Physique* 7 (1997) 635.
- [274] L.A.N. Amaral, S.V. Buldyrev, S. Havlin, P. Maass, M.A. Salinger, H.E. Stanley, M.H.R. Stanley, *Physica* 244 (1997) 1.
- [275] M. Lee, W. Li, *Econom. Lett.* 86 (2005) 339.
- [276] L. Chakravarti, R. Chakravarti, *Handbook of Methods of Applied Statistics*, vol. I, John Wiley and Sons, 1967, 392–394.
- [277] E. Wong, M. Zakai, *Int. J. Eng. Sci.* 3 (1965) 213;
E. Wong, M. Zakai, *Ann. Math. Stat.* 36 (1965) 1560.
- [278] O.E. Barndorff-Nielsen, T. Mikosch, S.I. Resnick (Eds.), *Levy Processes: Theory and Applications*, Birkhäuser, Boston, 2001.
- [279] P. Billingsley, *Probability and Measure*, Wiley, 1995.
- [280] T. Halpin-Healy, Y.C. Zhang, *Phys. Rep.* 245 (1995) 218.
- [281] C.-H. Lam, L.M. Sander, *Phys. Rev. Lett.* 71 (1993) 561.
- [282] A. Giacometti, M. Rossi, *Phys. Rev. E* 63 (2001) 046102.
- [283] A. Irajizad, G. Kavei, M. Reza Rahimi Tabar, S.M. Vaez Allaei, *J. Phys.: Condens. Matter* 15 (2003) 1889.
- [284] S. Mercik, K. Weron, *Phys. Rev. E* 63 (2001) 051910.
- [285] M. Ohring, *Materials Science of Thin Films: Deposition and Structure*, Academic Press, New York, 2002.
- [286] M. Marsilli, A. Maritan, F. Toigoend, J.R. Banavar, *Rev. Modern Phys.* 68 (1996) 963.
- [287] A.A. Masoudi, F. Shahbazi, J. Davoudi, M. Reza Rahimi Tabar, *Phys. Rev. E* 65 (2002) 026132.
- [288] M. Sahimi, *Heterogeneous Materials I & II*, Springer, New York, 2003.
- [289] O. Akhavan, M. Abdolhad, *Curr. Appl. Phys.* 10 (2010) 1203;
O. Akhavan, *Curr. Nanoscience* 6 (2010) 116;
O. Akhavan, R. Azimirad, *J. Phys. D: Appl. Phys.* 42 (2009) 065404;
G. Kavei, A.M. Gheidari, *J. Mater. Process. Technol.* 208 (2008) 514;
C.A. Haselwandter, D.D. Vvedensky, *Phys. Rev. E* 77 (2008) 061129;
G. Kavei, A.M. Gheidari, *Scanning* 30 (2008) 232.
- [290] W.F. Egelhoff Jr., P.J. Chen, C.J. Powell, M.D. Stiles, R.D. McMichael, C.L. Lin, J.M. Sivertsen, J.H. Judy, K. Takano, A.E. Berkowitz, T.C. Anthony, J.A. Brug, *J. Appl. Phys.* 79 (1996) 5277.
- [291] B. Dai, J.N. Coi, W. Lai, *J. Magn. Magn. Mat.* 27 (2003) 19.
- [292] A.Z. Moshfegh, O. Akhavan, *Thin Solid Films* 370 (2000) 10.
- [293] A.Z. Moshfegh, P. Sangpour, *Phys. Status Solidi C* 1 (2004) 1744.
- [294] H. Peitgen, D. Saupe, *The Science of Fractal Images*, Springer, Berlin, 1988.
- [295] J. Aue, J.T.M.D. Hosson, *Appl. Phys. Lett.* 71 (1997) 1347.
- [296] A.S. Monin, A.M. Yaglom, *Statistical Fluid Mechanics: Mechanics of Turbulence*, vol. 2, MIT Press, 1975.
- [297] L.F. Richardson, *Proc. Roy. Soc. A* 97 (1920) 354.
- [298] A.N. Kolmogorov, *Dokl. Akad. Nauk SSSR* 30 (1941) 301.
- [299] A.N. Kolmogorov, *Dokl. Akad. Nauk SSSR* 32 (1941) 16.
- [300] A.N. Kolmogorov, *J. Fluid Mech.* 13 (1962) 82.
- [301] G.I. Barenblatt, N. Goldenfeld, *Phys. Fluids* 7 (1995) 3078.
- [302] J. Herweijer, W. van de Water, in: R. Benzi (Ed.), *Advances in Turbulence V*, Kluwer Academic, 1995, pp. 210–216.
- [303] R. Camussi, D. Barbagallo, G. Guj, F. Stella, *Phys. Fluids* 8 (1996) 1181.
- [304] R. Camussi, R. Benzi, *Phys. Fluids* 9 (1997) 257.
- [305] H. Kahalerras, Y. Malec, Y. Gagne, in: S. Gavrilatus, L. Michiels, P.A. Monkewitz (Eds.), *Advances in Turbulence VI*, Kluwer Academic, 1996, pp. 235–238.
- [306] B.R. Pearson, Institut National Polytechnique de Grenoble (France), *Velocity structure functions in a turbulent plane jet*, vol. 339 (1997).
- [307] A. Noullez, G. Wallace, W. Lempert, R.B. Miles, U. Frisch, *J. Fluid Mech.* 339 (1997) 287.
- [308] S. Grossmann, D. Lohse, A. Reeh, *Phys. Fluids* 9 (1997) 3817.
- [309] S. Grossmann, D. Lohse, A. Reeh, *Phys. Rev. E* 56 (1997) 5473.
- [310] O.N. Boratav, R.B. Pelz, *Phys. Fluids* 9 (1997) 1400.
- [311] O.N. Boratav, *Phys. Fluids* 9 (1997) 1206.
- [312] O.N. Boratav, *Phys. Fluids* 9 (1997) 3120.
- [313] R.A. Antonia, M. Ould-Rouis, Y. Zhu, F. Anselmet, *Europhys. Lett.* 37 (1997) 85.
- [314] K.R. Sreenivasan, R.A. Antonia, *Annu. Rev. Fluid Mech.* 29 (1997) 435.
- [315] B. Dhruva, Y. Tsuji, K.R. Sreenivasan, *Phys. Rev. E* 56 (1997) R4928.
- [316] G.W. He, S.Y. Chen, R.H. Kraichnan, R.Y. Zhang, Y. Zhou, *Phys. Rev. Lett.* 81 (1998) 4636.
- [317] H. Kahalerras, Y. Malecot, Y. Gagne, B. Castaing, *Phys. Fluids* 10 (1998) 910.
- [318] G. Pedrizzetti, *Phys. Fluids* 11 (1999) 1694.
- [319] W. van de Water, J. Herweijer, *J. Fluid Mech.* 387 (1999) 3.
- [320] R.A. Antonia, B.R. Pearson, *Europhys. Lett.* 48 (1999) 163.
- [321] M. Nelkin, *Phys. Fluids* 11 (1999) 2202.
- [322] M. Nelkin, *Amer. J. Phys.* 68 (2000) 310.
- [323] R.A. Antonia, B.R. Pearson, T. Zhou, *Phys. Fluids* 12 (2000) 3000.
- [324] Y. Malecot, C. Auriault, H. Kahalerras, Y. Gagne, O. Chanal, B. Chabaud, B. Castaing, *Eur. Phys. J. B* 16 (2000) 549.
- [325] G.P. Romano, R.A. Antonia, *J. Fluid Mech.* 436 (2001) 231.
- [326] T. Zhou, R.A. Antonia, *J. Fluid Mech.* 406 (2000) 81.
- [327] A. Tsinober, *An Informal Introduction to Turbulence*, Kluwer Academic Publ, 2001.
- [328] A. Praskovskiy, S. Oncley, *Phys. Fluids* 6 (1994) 2886.
- [329] P. Marcq, A. Naert, *Phys. Fluids* 13 (2001) 2590.
- [330] A. Naert, R. Friedrich, J. Peinke, *Phys. Rev. E* 56 (1997) 6719.
- [331] P. Marcq, A. Naert, *Physica D* 124 (1998) 368.
- [332] I. Hosokawa, *Phys. Rev. E* 65 (2002) 027301.
- [333] I. Hosokawa, *Phys. Rev. Lett.* 91 (2003) 109401.
- [334] C. Renner, J. Peinke, R. Friedrich, O. Chanal, B. Chabaud, *Phys. Rev. Lett.* 89 (2000) 124502.
- [335] S. Siegert, R. Friedrich, J. Peinke, *Phys. Lett. A* 243 (1998) 275.
- [336] P.-O. Amblard, J.-M. Brossier, *Eur. Phys. J. B* 12 (1999) 579.
- [337] M. Siefert, J. Peinke, *J. Turbul.* 7 (2006) 1.
- [338] R. Benzi, S. Ciliberto, R. Tripiccion, C. Baudet, F. Massaioli, S. Succi, *Phys. Rev. E* 48 (1993) R29.
- [339] R. Benzi, S. Ciliberto, C. Baudet, G.R. Chavarria, *Physica D* 80 (1995) 385.
- [340] A. Arneodo, et al., *Europhys. Lett.* 34 (1996) 411.
- [341] S.B. Pope, *Turbulent Flows*, Cambridge University Press, 2000.

- [342] A.M. Oboukhov, *J. Fluid Mech.* 13 (1962) 77.
- [343] F. Anselmet, Y. Gagne, E.J. Hopfinger, R.A. Antonia, *J. Fluid Mech.* 140 (1984) 63.
- [344] A. Arneodo, J.-F. Muzy, D. Sornette, *Eur. Phys. J. B* 2 (1998) 277.
- [345] L. Mydlarski, Z. Warhaft, *J. Fluid Mech* 358 (1998) 135.
- [346] A.M. Oboukhov, *Izv. Akad. Nauk. SSSR, Geogr. Geofiz.* 13 (1949) 58.
- [347] S. Corrsin, *J. Appl. Phys.* 22 (1951) 469.
- [348] N.N. Korchaskin, *Izv. Atmos. Ocean. Phys.* 6 (1970) 947.
- [349] C.W. Van Atta, *Phys. Fluids* 14 (1971) 1803.
- [350] R.A. Antonia, E.J. Hopfinger, Y. Gagne, F. Anselmet, *Phys. Rev. A* 30 (1984) 2704.
- [351] Z. Warhaft, *Annu. Rev. Fluid Mech.* 2 (2000) 203.
- [352] B.I. Shraiman, E.D. Siggia, *Nature* 405 (2000) 639.
- [353] Y. Yakhot, *Phys. Rev. E* 57 (1998) 1737.
- [354] S. Vaienti, M. Ould-Rouis, F. Anselmet, P.L. Gal, *Physica D* 73 (1994) 99.
- [355] M. Ould-Rouis, F. Anselmet, P.L. Gal, S. Vaienti, *Physica D* 85 (1995) 405.
- [356] S. Bounoua, M. Ould-Rouis, P.L. Gal, F. Anselmet, *Int. J. Heat Mass Transfer* 41 (1998) 2049.
- [357] C.H. Scholz, *The Mechanics of Earthquakes and Faulting*, Cambridge University Press, Cambridge, 1990.
- [358] V.I. Keilis-Borok, L.N. Malinovskaya, *J. Geophys. Res.* 69 (1964) 3019.
- [359] V.I. Keilis-Borok, A.A. Soloviev, *Nonlinear Dynamics of the Lithosphere and Earthquake Prediction*, Springer, Heidelberg, 2002.
- [360] P. Bhattacharyya, B.K. Chakrabarti, *Modelling Critical and Catastrophic Phenomena in Geoscience: A Statistical Physics Approach*, in: *Lecture Notes in Physics*, 705, Springer, Berlin, 2007.
- [361] B. Gutenberg, R.F. Richter, *Seismicity of the Earth*, Hafner Publishing, New York, 1965.
- [362] T. Utsu, Y. Ogata, R.S. Matsu'ura, *J. Phys. Earth* 43 (1995) 1.
- [363] P. Bak, C. Tang, J. Geophys. Res. 94 (1989) 15635.
- [364] S. Hallerberg, E.G. Altmann, D. Holstein, H. Kantz, *Phys. Rev. E* 75 (2007) 016706.
- [365] E.G. Altmann, D. Holstein, H. Kantz, *Phys. Rev. E* 75 (2007) 016706.
- [366] L.M. Jones, P. Molnar, *J. Geophys. Res.* 84 (1979) 3596.
- [367] F.T. Freund, *J. Geodyn.* 33 (2002) 545.
- [368] G.A. Sobolev, Y.S. Tyupkin, *Phys. Solid Earth* 36 (2) (2000) 138.
- [369] L. Knopoff, et al., *J. Geophys. Res.* 101 (1996) 5779.
- [370] A. Sornette, D. Sornette, *Tectonophysics* 179 (1990) 327.
- [371] C.J. Allègre, L. Mouel, A. Provost, *Nature* 297 (1982) 47.
- [372] B. Voight, *Nature* 332 (1989) 125.
- [373] B. Voight, *Science* 243 (1989) 200.
- [374] L.R. Sykes, S. Jaumé, *Nature* 348 (1990) 595.
- [375] C.G. Bufe, D.J. Varnes, *J. Geophys. Res.* 98 (1993) 9871.
- [376] W.I. Newman, D.L. Turcotte, A.M. Gabrielov, *Phys. Rev. E* 52 (1995) 4827.
- [377] H. Saleur, C.G. Sammis, D. Sornette, *Nonlinear Process. Geophys.* 3 (1996) 102.
- [378] H. Saleur, C.G. Sammis, D. Sornette, *J. Geophys. Res.* 101 (1996) 17661.
- [379] A. Johansen, H. Saleur, D. Sornette, *Eur. Phys. J. B* 15 (2000) 551.
- [380] Y. Huang, H. Saleur, C.G. Sammis, D. Sornette, *Europhys. Lett.* 41 (1998) 43.
- [381] D.D. Bowman, G. Ouillon, C.G. Sammis, A. Sornette, D. Sornette, *J. Geophys. Res.* 103 (1998) 2435.
- [382] D.J. Brehm, L.W. Braile, *Bull. Seismol. Soc. Amer.* 88 (1998) 564.
- [383] G. Zoller, S. Hainzl, *Nat. Hazards. Earth Syst. Sci.* 1 (2001) 93.
- [384] G. Zoller, S. Hainzl, J. Kurths, *J. Geophys. Res.* 106 (2001) 2167.
- [385] G. Zoller, S. Hainzl, *Geophys. Res. Lett.* 29 (2002) 101029.
- [386] K. Sobczyk, *Acta Mechanica* 25 (1976) 13.
- [387] B. Gurevich, *Geophysics* 67 (2002) 264.
- [388] F. Shahbazi, A. Bahraminasab, S.M. Vaez Allaei, M. Sahimi, M. Reza Rahimi Tabar, *Phys. Rev. Lett.* 94 (2005) 165505.
- [389] A. Bahraminasab, S.M. Vaez Allaei, F. Shahbazi, M. Sahimi, M.D. Niry, M. Reza Rahimi Tabar, *Phys. Rev. B* 75 (2007) 064301;
A. Sheikhan, N. Abedpour, R. Sepehrinia, M.D. Niry, M. Reza Rahimi Tabar, M. Sahimi, *Waves Random Media* 20 (2010) 191;
A. Sheikhan, M.R. Rahimi Tabar, M. Sahimi, *Phys. Rev. B* 80 (2009) 035130;
M. Sahimi, M.R. Rahimi Tabar, A. Bahraminasab, R. Sepehrinia, S.M. Vaez Allaei, *Acta Mech.* 205 (2009) 197;
A. Esmailpour, M. Esmailpour, A. Sheikhan, M. Elahi, M.R. Rahimi Tabar, M. Sahimi, *Phys. Rev. B* 78 (2008) 134206;
R. Sepehrinia, M. Reza Rahimi Tabar, M. Sahimi, *Phys. Rev. B* 78 (2008) 024207;
S. Mehdi Vaez Allaei, M. Sahimi, M.R. Rahimi Tabar, *J. Stat. Mech.* (2008) P03016;
R. Sepehrinia, A. Bahraminasab, M. Sahimi, M. Reza Rahimi Tabar, *Phys. Rev. B* 77 (2008) 014203;
N. Abedpour, M. Neek-Amal, Reza Asgari, F. Shahbazi, N. Nafari, M. Reza Rahimi Tabar, *Phys. Rev. B* 76 (2007) 195407;
A. Esmailpour, M. Esmailzadeh, E. Faizabadi, P. Carpena, M. Reza Rahimi Tabar, *Phys. Rev. B* 74 (2006) 024206;
A. Esmailpour, H. Cheraghchi, Pedro Carpena, M. Reza Rahimi Tabar, *J. Stat. Mech.* (2007) P09014;
A.E.B. Costa, F.A.B.F. de Moura, *J. Phys.: Condens. Matter* 23 (2011) 065101;
A.E.B. Costa, F.A.B.F. de Moura, *Eur. Phys. J. B* 79 (2011) 253.
- [390] R. Metzler, J. Klafter, *Phys. Rep.* 339 (2000) 1;
R. Metzler, J. Klafter, *J. Phys. A: Math. Gen.* 37 (2004) R161.
- [391] M.F. Shlesinger, G.M. Zaslavsky, J. Klafter, *Nature* 363 (1999) 31.
- [392] G.M. Zaslavsky, *Phys. Today* 52 (1999) 39.
- [393] R. Balescu, *Aspects of Anomalous Transport in Plasmas*, Taylor & Francis, 2005.
- [394] I. Lubashevsky, R. Friedrich, A. Heuer, *Phys. Rev. E* 79 (2009) 011110; *Phys. Rev. E* 80 (2009) 031148.
- [395] R. Friedrich, F. Jenko, A. Baule, S. Eule, *Phys. Rev. Lett.* 96 (2006) 230601.
- [396] R. Friedrich, F. Jenko, A. Baule, S. Eule, *Phys. Rev. E* 74 (2006) 041103.
- [397] S. Eule, R. Friedrich, F. Jenko, *J. Phys. Chem. B* 111 (2007) 13041.
- [398] S. Eule, R. Friedrich, F. Jenko, D. Kleinhans, *J. Phys. Chem. B* 111 (2007) 11474.
- [399] S. Eule, R. Friedrich, F. Jenko, I.M. Sokolov, *Phys. Rev. E* 78 (2008) 060102.
- [400] A. Baule, R. Friedrich, *Phys. Rev. E* 71 (2005) 026101.
- [401] A. Baule, R. Friedrich, *Europhys. Lett.* 77 (2007) 10002.
- [402] A. Baule, R. Friedrich, *Europhys. Lett.* 79 (2007) 60004.
- [403] H. Affan, R. Friedrich, S. Eule, *Phys. Rev. E* 80 (2009) 011137.